NREL
NATIONAL RENEWABLE ENERGY LABORATORY

Advanced Power Electronics and Electric Motors Annual Report – 2013

S. Narumanchi, K. Bennion, D. DeVoto, G. Moreno, J. Rugh, and S. Waye
National Renewable Energy Laboratory

NREL is a national laboratory of the U.S. Department of Energy
Office of Energy Efficiency & Renewable Energy
Operated by the Alliance for Sustainable Energy, LLC

This report is available at no cost from the National Renewable Energy Laboratory (NREL) at www.nrel.gov/publications.

Technical Report
NREL/TP-5400-60621
January 2015

Contract No. DE-AC36-08GO28308

NREL
NATIONAL RENEWABLE ENERGY LABORATORY

Advanced Power Electronics and Electric Motors Annual Report – 2013

S. Narumanchi, K. Bennion, D. DeVoto, G. Moreno, J. Rugh, and S. Waye
National Renewable Energy Laboratory

Prepared under Task No. VTP2.7000

NREL is a national laboratory of the U.S. Department of Energy
Office of Energy Efficiency & Renewable Energy
Operated by the Alliance for Sustainable Energy, LLC

This report is available at no cost from the National Renewable Energy Laboratory (NREL) at www.nrel.gov/publications.

National Renewable Energy Laboratory
15013 Denver West Parkway
Golden, CO 80401
303-275-3000 • www.nrel.gov

Technical Report
NREL/TP-5400-60621
January 2015

Contract No. DE-AC36-08GO28308

NOTICE

This report was prepared as an account of work sponsored by an agency of the United States government. Neither the United States government nor any agency thereof, nor any of their employees, makes any warranty, express or implied, or assumes any legal liability or responsibility for the accuracy, completeness, or usefulness of any information, apparatus, product, or process disclosed, or represents that its use would not infringe privately owned rights. Reference herein to any specific commercial product, process, or service by trade name, trademark, manufacturer, or otherwise does not necessarily constitute or imply its endorsement, recommendation, or favoring by the United States government or any agency thereof. The views and opinions of authors expressed herein do not necessarily state or reflect those of the United States government or any agency thereof.

This report is available at no cost from the National Renewable Energy Laboratory (NREL) at www.nrel.gov/publications.

Available electronically at http://www.osti.gov/scitech

Available for a processing fee to U.S. Department of Energy and its contractors, in paper, from:

U.S. Department of Energy
Office of Scientific and Technical Information
P.O. Box 62
Oak Ridge, TN 37831-0062
phone: 865.576.8401
fax: 865.576.5728
email: mailto:reports@adonis.osti.gov

Available for sale to the public, in paper, from:

U.S. Department of Commerce
National Technical Information Service
5285 Port Royal Road
Springfield, VA 22161
phone: 800.553.6847
fax: 703.605.6900
email: orders@ntis.fedworld.gov
online ordering: http://www.ntis.gov/help/ordermethods.aspx

Cover Photos: (left to right) photo by Pat Corkery, NREL 16416, photo from SunEdison, NREL 17423, photo by Pat Corkery, NREL 16560, photo by Dennis Schroeder, NREL 17613, photo by Dean Armstrong, NREL 17436, photo by Pat Corkery, NREL 17721.

NREL prints on paper that contains recycled content.

Table of Contents

Integrated Power Module Cooling 1
Advanced Liquid Cooling Research and Development 12
Two-Phase Cooling of Power Electronics 20
Air-Cooling Technology for Power Electronics Thermal Management 28
Electric Motor Thermal Management 38
Combining Fluid Loops on Electric-Drive Vehicles 46
Reliability of Bonded Interfaces 51
Reliability of Electrical Interconnects 59

This report is available at no cost from the National Renewable Energy Laboratory (NREL) at www.nrel.gov/publications.

Integrated Power Module Cooling

Principal Investigator: Kevin Bennion
National Renewable Energy Laboratory (NREL)
Transportation and Hydrogen Systems Center
15013 Denver West Parkway
Golden, CO 80401
Phone: 303-275-4447
E-mail: Kevin.Bennion@nrel.gov

DOE Technology Development Manager: Susan A. Rogers
Phone: 202-586-8997
E-mail: Susan.Rogers@ee.doe.gov

NREL Task Leader: Sreekant Narumanchi
Phone: 303-275-4062

Start Date: October 2011
Projected End Date: September 2013

Objectives

A cost-effective, compact, efficient, and reliable electric traction drive is a key enabling technology for the electrification of vehicle propulsion systems. Heat dissipation has a significant impact on the power capability of power electronics, which leads to increased device cost and package volume or size. The optimal thermal performance is a function of the power electronics packaging and the heat exchanger design. To reach the desired cost and performance objectives, a solution that integrates commercially available packages with low-cost cooling technologies is needed. As seen in Figure 1, approximately 46% of the inverter cost is attributed to the power silicon, thermal management, and housing [1]. The National Renewable Energy Laboratory (NREL) team has developed a concept for an integrated power electronics module heat exchanger to reduce cost and improve the power per die area. The primary objectives are to:

- Improve power per die area by 100% over existing commercial power electronics thermal management systems
- Maintain best-in-class power density capabilities as compared to existing systems
- Enable a modular or scalable thermal approach to reduce the need for custom heat exchanger redesigns as applications scale in power
- Eliminate internal fluid seals commonly found on existing integrated cooling concepts to reduce leakage-induced failure modes
- Reduce parasitic power requirements for the cooling system.

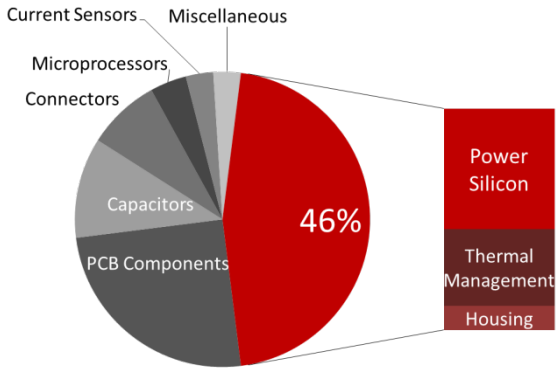

Figure 1: Inverter cost drivers [1]

Technical Barriers

The intent of the project is to demonstrate the concept and potential application of the thermal management approach. The pathway towards commercialization requires addressing the following potential barriers.

- Scaling the research and development prototype to address high-volume manufacturing processes for reduced cost.
  - We collaborated with an industry partner with experience in heat exchanger manufacturing methods to get input and guidance to reduce fabrication cost.
- The integration of the electronics package with the heat exchanger requires robust and low thermal resistance interfaces.
  - Past and current work performed within the Advanced Power Electronics and Electric Motor (APEEM) activity in regards to thermal interface materials and bonded interface materials is seen as a critical enabler for this this project.
- The cooling design should support multiple power semiconductor packaging methods.
  - The project considered the application of the design to multiple packaging and interconnect methods.
  - The design addressed in the project is compatible with single- and double-sided cooling configurations for power semiconductor thermal management.

Technical Targets

The U.S. Department of Energy (DOE) technical targets applicable to this research are the goals outlined in the Electrical and Electronics Technical Team Roadmap [2]. Specifically, the project helps in meeting 2015 and 2020 power electronics technical targets. Because this project focuses on the thermal management of the power electronics and not the development of a full inverter, the APEEM technical targets were cascaded down into project goals specific to the thermal management research. The approach of cascading the APEEM system-level targets to thermal management goals specific to the project is shown in Figure 2. The specific project goals are summarized as follows:

This report is available at no cost from the National Renewable Energy Laboratory (NREL) at www.nrel.gov/publications.

- Cost
  - Improve power per die area with comparable or better power density
  - Low cost, scalable, and low-waste manufacturing methods
- Volume
  - Maintain equivalent or better power density
- Weight
  - Eliminate large cast heat exchangers
- Reliability
  - Remove internal fluid seals to reduce leak-induced failure modes
  - Increase passive stack thermal capacitance for transient heat loads

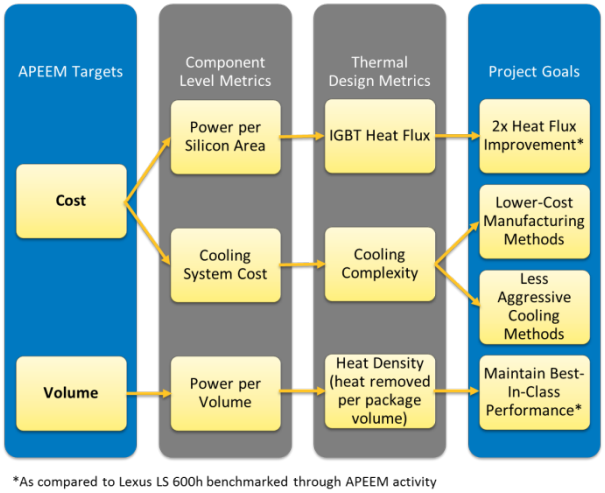

Figure 2: Project goals

Accomplishments

The project concluded in FY13 because the project goals were achieved and the next path towards commercialization would involve a collaborative industry project to further develop the concepts for a specific inverter application. During FY13, the following project goals were achieved:

- Demonstrated the potential to double the heat removal capability of the power semiconductor devices, leading to increased power per semiconductor die area
- Demonstrated a greater than 30% increase in the package heat density, which exceeded the original project goal, which leads to improved power density
- Showed one approach to using extruded cold rails for power electronics cooling, potentially reducing weight and eliminating the need for large cast metal heat exchangers
- Illustrated a concept that removes internal seals to reduce potential failure modes from internal fluid leaks
- Demonstrated an approach to improve semiconductor thermal management without negatively impacting the thermal capacitance within the module, which impacts the temperature cycling behavior of the module and reliability
- Developed a modular and scalable thermal approach, which can reduce the need for custom heat exchanger redesigns as applications scale in power
- Reduced cost and increased reliability by using larger channel dimensions that are more economical to manufacture and less likely to clog
- Maintained compatibility to alternative power semiconductor packaging technologies such as wire bonds, ribbon bonds, or planar interconnect technologies for single and double sided cooling
- Built three prototype designs and validated model results against experimental results
- Established a collaboration with a heat exchanger development partner (Sapa Extrusions North America)
- Received patent incorporating proposed cooling approaches [3].

✧ ✧ ✧ ✧ ✧

Introduction

Improving the ability to remove heat from power electronics semiconductor packages is significant in reducing the cost and size of semiconductor devices [4]. For this reason, new and improved thermal management approaches are needed for power electronics systems. The overall thermal performance of the power electronics system depends on both the thermal packaging of the semiconductor devices and the design of the cooling interface. As shown in previous work, the cooling performance must be matched to the package design to get the optimal integrated solution [5]–[7].

Existing State of the Art

The heat dissipation limitations of a conventional power electronics package, as shown in Figure 3, are well known and described in the literature. The thermal limitations of the thermal interface material between the heat spreader and the heat exchanger have led to efforts to improve the thermal interface [8] or remove interface materials through direct cooling.

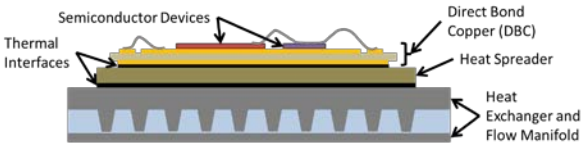

Figure 3: Conventional power electronics semiconductor thermal stack with heat spreader and thermal interface material between the heat spreader and the heat exchanger surface

Direct cooling of the power semiconductor package can take multiple forms, but generally involves removing intermediate layers between the semiconductor device and the cooling fluid. Two common approaches involve direct cooling of the heat spreader, as shown in Figure 4, or direct cooling of the substrate metallization layer (Figure 5). Examples include direct bond

This report is available at no cost from the National Renewable Energy Laboratory (NREL) at www.nrel.gov/publications.

copper (DBC) or direct bond aluminum, as shown in Figure 5. Direct cooling reduces available cooling surface area and requires more aggressive cooling mechanisms [6]. Examples include fluid jets that impinge on the heat spreader or DBC directly [9]–[11], microchannels [12], pin fins [13]–[16], or other fin structures such as folded fins attached to the heat spreader [17].

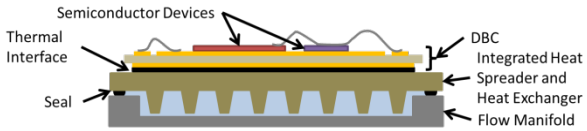

Figure 4: Example package with a direct-cooled heat spreader

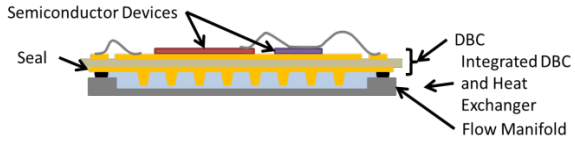

Figure 5: Example package with direct-cooled metallization layer such as DBC

In addition to improving the thermal performance through reducing the thermal stack resistance and more aggressive cooling, others have proposed methods to remove heat from both sides of the power semiconductor device (also known as double-sided-cooling) [4, 18, 19]. A commercial example is the 2008 Lexus LS 600H hybrid electric vehicle, which is summarized in a report by Burress et al. [20] and which achieved the highest power density of the commercial devices benchmarked through the DOE's Vehicle Technologies Office. A schematic of the cooling and thermal package structure is provided in Figure 6.

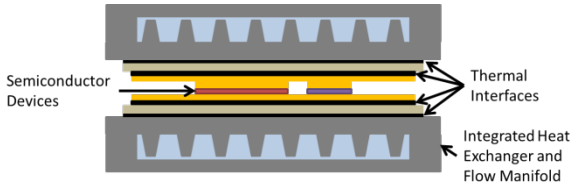

Figure 6: Example package enabling cooling on both sides of the power semiconductor device (double-sided cooling)

While the approaches discussed previously are effective at improving the ability to remove heat from the semiconductor devices, they face challenges regarding implementation. All of the cooling approaches highlighted above are dominated by planar heat removal structures that focus on one-dimensional heat transfer out of the power semiconductor package through the top or bottom of the package. The heat spreader does allow for some thermal spreading, but the cooling is applied to a single surface of the package. When the heat spreader is removed and the coolant fluid is directly applied to the DBC, the reduced heat spreading requires more aggressive cooling to maintain the same performance as illustrated by Bennion and Moreno [6]. The drive to more aggressive cooling leads to concerns related to fluid channel size, parasitic power, reliability, construction, and cost. To enable less aggressive convective cooling technologies, the heat spreading characteristics of the package passive thermal stack must be matched or optimized to the convective cooling performance. The removal of layers within the semiconductor package also reduces the thermal capacitance of the structure, making the semiconductor more susceptible to transient loading effects, which impacts reliability. Also, the direct-cooling approaches illustrated in Figure 4 and Figure 5 often require seals to prevent coolant from leaking into the electronics, which can lead to issues related to performance and reliability [13].

Proposed Concept

NREL's proposed cooling approach [3] attempts to emphasize the use of the heat spreader to enable high cooling performance with less aggressive convective cooling methods. The approach integrates the heat spreader with the heat exchanger to provide multiple heat transfer paths within the heat spreader. Improving the heat spreading characteristics of the package provides an opportunity to increase the available surface area in contact with the coolant and does not rely on aggressive convective cooling methods or small fluid channel passages. Instead of relying on a planar thermal stack dominated by one-dimensional heat transfer (Figure 7), the concept design uses the available space around the package to spread and remove heat along multiple paths, as illustrated in Figure 8.

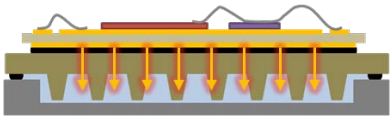

Figure 7: Conventional system with one-dimensional dominated heat flow path

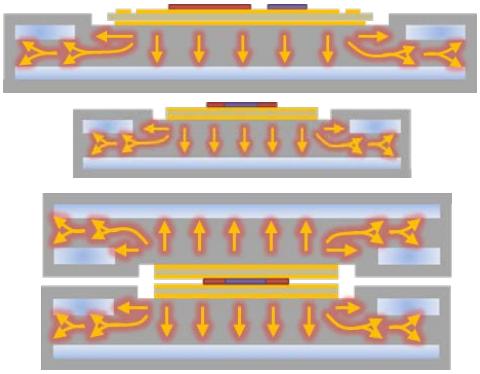

Figure 8: Conceptual drawings of integrated heat spreader and heat exchanger system to enhance heat spreading and cooling performance

In addition to improving the thermal performance, the concept features other important characteristics not directly related to heat transfer. The design enables a modular, or scalable, approach to the cooling of power semiconductor devices that builds upon high-volume manufacturing methods already accepted by the automotive industry. Examples include thin-film folded fins used in brazed automotive heat exchangers and extruded aluminum materials used in a wide range of applications. The concept also eliminates the internal seals

This report is available at no cost from the National Renewable Energy Laboratory (NREL) at www.nrel.gov/publications.

shown in Figure 4 and Figure 5. The seals are moved to external locations to reduce the risk of coolant interfering with the electrical components. Additionally, the parasitic power requirements for the cooling system are reduced by increasing the fluid channel dimensions.

Approach

The goal of the project was to prove the potential of the cooling concept and refine the design that would lead to a hardware prototype for validation of the model results. Our work during FY13 focused on the process highlighted in Figure 9, which involves the following steps:

- Performing thermal finite element analysis (FEA) design optimization of the heat spreader structure to investigate the thermal structure design, select heat spreader materials, and identify convective cooling performance targets
- Evaluating cooling surface enhancement designs using computational fluid dynamics (CFD) modeling tools and confirming the ability to develop a heat exchanger surface that meets the minimum convective cooling performance requirements
- Building and testing hardware prototypes
- Simulating the full system to iterate on the heat spreader design and the convective cooling heat exchanger surface to enable lower cost manufacturing.

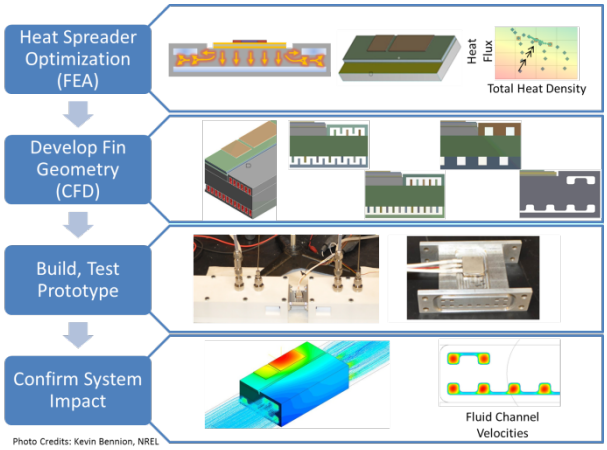

Figure 9: Thermal management design strategy

Analytical Design Approach

The heat spreader was optimized through a series of iterations involving FEA and CFD. Thermal FEA has an advantage over CFD simulation in speed, allowing more design iterations within a set period of time. CFD has the advantage of providing detailed fluid dynamics and heat transfer results for specific heat exchanger geometries. For this reason, we developed a method to decouple the fluid dynamics and heat transfer results within CFD simulations from the passive stack thermal model within CFD or FEA framework. The first step in the process is estimating the appropriate convective boundary conditions for the thermal FEA model.

The effective convection coefficient (h) is calculated following the Effectivness-Number of Transfer Units (NTU) heat exchanger analysis method following equations 1–5 [21] . The first step in the analysis estimates the convection coefficient and area product (UA) for the reference surface. Knowing the mass flow ($\dot{m}$) and fluid specific heat (c_p) it is possible to calculate the heat exchanger NTU and effectiveness (ε), which can be used to calculate heat exchanger thermal resistance ($R_{th,NTU}$), area weighted thermal resistance ($R''_{th,NTU}$), and h. The final result is an appropriate convection coefficient that can be applied to the thermal FEA model, such as within ANSYS that accounts for the impact of fluid properties and fluid flow rate.

$$NTU = \frac{UA}{\dot{m}c_p} \quad (1)$$

$$\varepsilon = 1 - e^{-NTU} \quad (2)$$

$$R_{th,NTU} = \frac{1}{\varepsilon \dot{m} c_p} \quad (3)$$

$$R''_{th,NTU} = \frac{A}{\varepsilon \dot{m} c_p} \quad (4)$$

$$h = \frac{1}{R''_{th,NTU}} \quad (5)$$

Two approaches were develedoped to calculate the convection coefficient and area product (UA) in equation 1. Figure 8 illlustrates the two approaches. The first approach estimates a UA over the channel wetted area, while the second approach estimates a UA over a flat base surface.

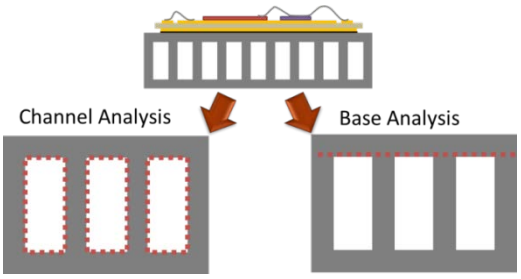

Figure 10: The convective heat transfer boundary conditions were evaluated along the channel (left) and a cut plan along the base of the heat exchanger (right)

In the first approach, the effective convection coefficient along the channel wetted area is calculated from CFD simulation results. The effective convection coefficient is then applied within the thermal FEA model. Applying the convection coefficient within the thermal FEA model provides a secondary check on the passive stack thermal model within the CFD and FEA models. Performing the analysis within a thermal FEA also allows for quicker sensitivity studies associated with the convection coefficient and passive thermal stack of the package. The procedure for calculating the channel UA product follows equations 6–9, where the symbols are defined in Table 1. This approach assumes a uniform convection coefficient is applied to the FEA thermal model at the fluid inlet temperature.

This report is available at no cost from the National Renewable Energy Laboratory (NREL) at www.nrel.gov/publications.

$$\Delta T_1 = T_{surf,av,ch} - T_{c,o} \quad (6)$$

$$\Delta T_2 = T_{surf,av,ch} - T_{c,i} \quad (7)$$

$$\Delta T_{lm,ch} = \frac{(\Delta T_1 - \Delta T_2)}{ln\left({}^{\Delta T_1}/_{\Delta T_2}\right)} \quad (8)$$

$$(UA)_{ch} = \frac{Q}{\Delta T_{lm,ch}} \quad (9)$$

Table 1: Nomenclature for channel calculations

Symbol	Description
$T_{c,o}$	Outlet coolant temperature
$T_{c,i}$	Inlet coolant temperature
$T_{surf,av,ch}$	Average temperature of channel walls
$\Delta T_{lm,ch}$	Channel log mean temperature difference
$(UA)_{ch}$	Channel convection coefficient and area product
Q	Heat into channels

The second approach simplifies the analysis by cutting the heat exchanger along the base, removing the geometry complexities of the fins. This analysis is useful for comparing the interactions between the passive stack thermal resistance and an effective heat exchanger convective cooling thermal resistance. Instead of calculating a UA along the wetted channels, a UA across an arbitrary plane is defined. The process is listed in equations 10–13, where the symbols are defined in Table 2.

$$\Delta T_1 = T_{surf,av,base} - T_{c,o} \quad (10)$$

$$\Delta T_2 = T_{surf,av,base} - T_{c,i} \quad (11)$$

$$\Delta T_{lm,base} = \frac{(\Delta T_1 - \Delta T_2)}{ln\left({}^{\Delta T_1}/_{\Delta T_2}\right)} \quad (12)$$

$$(UA)_{base} = \frac{Q}{\Delta T_{lm,base}} \quad (13)$$

Table 2: Nomenclature for base calculations

Symbol	Description
$T_{surf,av,base}$	Average temperature along base
$\Delta T_{lm,base}$	Base log mean temperature difference
$(UA)_{base}$	Base convection coefficient and area product

Breaking up the heat exchanger analysis as outlined above provides a method for evaluating the combined thermal performance incorporating the passive thermal stack and the convecting cooling performance. The process allows quick design studies and optimization with thermal FEA models and selective CFD analysis at periodic intervals. Also, prior to having prototype hardware for testing, the ability to compare CFD and FEA model results provides a valuable check for modeling errors. Full conjugate heat transfer simulations within CFD were compared to simplified FEA models with boundary conditions calculated from the full model.

Adjustments for Manufacturing Cost

The heat exchanger was designed with a focus on cost. The goal was not to maximize the heat transfer convection coefficient for the heat exchanger. Instead, design iterations focused on making the heat exchanger more economical while still meeting the targeted cooling performance. The initial focus for the design focused on designing an extruded aluminum heat sink. An extruded aluminum process was selected because of its lower tooling cost as compared to aluminum castings and the ability to use higher thermal conductivity alloys (36% improvement in thermal conductivity) with lower material cost.

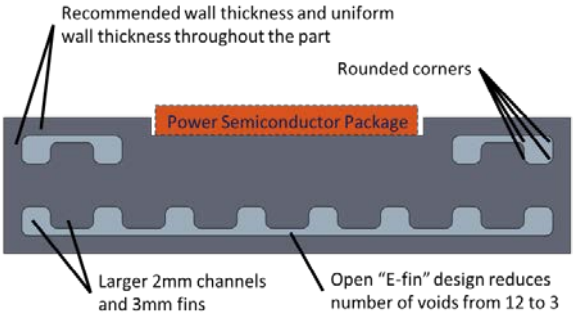

Figure 11: Sample parameters from design guidelines to reduce fabrication cost

The adjustments to the design followed guidelines consistent with input obtained through an extrusion design manual provided by Sapa Extrusions North America [22]. Some of the key features to reduce the manufacturing cost are highlighted in Figure 11, and they include rounded corners, reducing the number of internal voids, and maintaining a minimum recommended thickness that is dependent on the size of the part. One key factor in reducing tooling cost is the open "E-fin" design in Figure 11. The "E-fin" reduces the number of voids in the extruded part as compared to closed channels, which results in 12 voids. Based on industry input, the reduction from 12 to three voids results in an approximate 25% cost reduction. The final design prototype is shown in Figure 12 with a heater bonded to the surface. The flanges are included to attach the prototype to the inlet and outlet manifolds for testing.

This report is available at no cost from the National Renewable Energy Laboratory (NREL) at www.nrel.gov/publications.

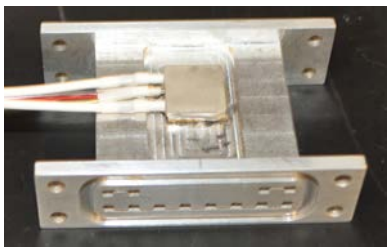

Figure 12: Prototype heat exchanger with heater

Experimental Approach

Once the design was selected, three heat exchangers were built. Two heat exchangers representing the design were built with Al6061 and Al6063. The third heat exchanger represented a baseline with a single cooling zone beneath the package, which was made with Al6061. The baseline and design heat exchanger geometries are shown in Figure 13. The materials used to fabricate the heat exchangers are listed in Table 4. The Al6063 material was provided by Sapa Extrusions North America.

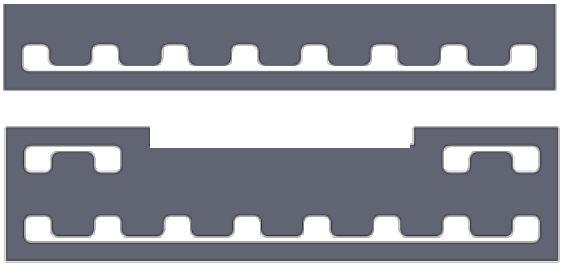

Figure 13: Fabricated heat exchanger geometries showing baseline (top) and design (bottom)

Table 3: Tested heat exchangers and materials

Geometry	Material
Baseline	Al 6061
Design	Al 6061
Design	Al 6063

Each of the heat exchangers listed in Table 4 was tested experimentally to verify the simulated thermal and fluid characteristics of the heat exchanger from the CFD simulation results. The model validation experiments were performed with a water-ethylene glycol (WEG) mixture of 50%/50% by volume. The heat exchangers were tested at 2.0 kg/min, 4.0 kg/min, and 6.0 kg/min (1.9 L/min, 3.8 L/min, and 5.7 L/min). The tests on the baseline heat exchanger included five repetitions, and tests on the design heat exchanger included six repetitions for each test condition. The inlet coolant temperature was set to 30°C for each test, and the specific gravity of the fluid was checked prior to starting tests to ensure the fluid properties remained constant.

The test setup is shown in Figure 14 and Figure 15. Figure 14 is a drawing of the inlet manifold that attaches to the heat exchanger flange, while Figure 15 shows the hardware with temperature and pressure measurement apparatuses within the inlet and outlet manifolds.

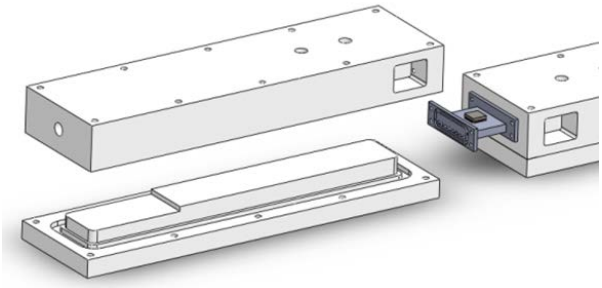

Figure 14: Test section showing inlet manifold for CFD model validation

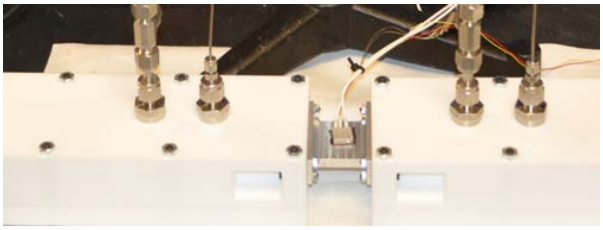

Figure 15: Heat exchanger installed in test fixture with inlet and outlet temperature and pressure measurements

As shown in Figure 12, a heater representing a power semiconductor device heat load was mounted to a copper spreader with epoxy (Figure 16). The copper spreader was bonded to the heat exchanger with Btech thermoplastic material (referred to as Btech - Figure 16). The copper spreader was instrumented with thermocouples in two locations (Figure 17), and the thermocouples were soldered into the copper spreader to ensure good thermal contact.

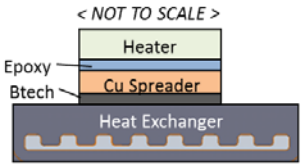

Figure 16: Heater assembly layers

This report is available at no cost from the National Renewable Energy Laboratory (NREL) at www.nrel.gov/publications.

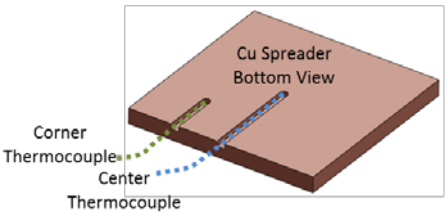

Figure 17: Thermocouple locations in the copper spreader

The measurement uncertainties of temperature and pressure were estimated to include systematic and random errors. The thermocouples were calibrated, and the total 95% confidence interval (U95) was within ±0.13°C (~0.4%). The heater also included a temperature measurement, but it was not calibrated with the thermocouples installed into the copper spreader. The inlet and outlet pressures were monitored with a U-tube manometer with a U95 of ±14 Pa (~1%).

The epoxy layer and the Btech layer represented unknown thermal resistance within the stack. The values for these thermal resistances were estimated by matching the temperature measurements at the lowest flow rate to the model results. The process for determining the effective thermal conductivity of the epoxy and Btech layers followed the listed steps and is illustrated in Figure 18.

- The convection coefficients were mapped from a single flow rate CFD model to the FEA model channels.
- The effective resistance and thermal conductivity of the epoxy and Btech layers were solved iteratively for a single test by matching the temperature change between the heater to copper spreader and the temperature change between the copper spreader to the inlet coolant temperature.
- The effective thermal resistance values for the epoxy and Btech layers were applied to the CFD model and validated against experimental results for other flow rates.

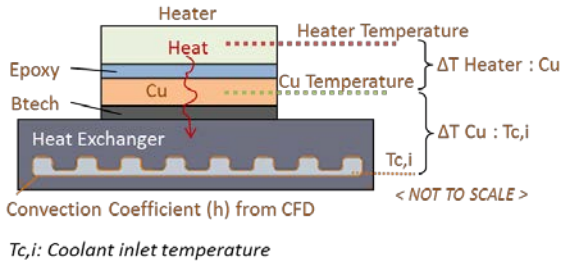

Figure 18: Interface thermal resistance estimation for epoxy and Btech bonding layers

System Level impacts

Once the CFD model results for the heat exchanger design were validated against the experimental results, the next step involved evaluating the cooling impacts for an insulated gate bipolar transistor (IGBT)/diode package. The heat exchanger was designed to operate in the flow configuration shown in Figure 19 in which each IGBT/diode package is cooled in parallel. In addition to the assumed flow arrangement, other assumptions were applied related to the heat distribution and maximum component temperatures. The ratio of heat in the IGBT to the heat in the diode was set to 3:1, and the maximum device temperature was limited to 150°C. The bond between the package and the heat exchanger was also assumed to provide equivalent thermal performance as solder. The inlet WEG coolant temperature was fixed at 70°C.

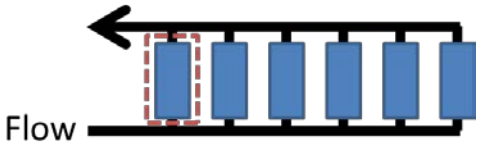

Figure 19: Assumed parallel flow arrangement for system-level analysis

Results

The key results from the work performed during FY13 are summarized below. The results are broken into sections covering the modeling results, experimental results, and system-level impacts.

Design Modeling Results

Heat spreader performance as compared to alternative package arrangements is shown in Figure 20 and Figure 21. The primary goal of the research was to enable high thermal performance (IGBT heat flux) with less aggressive cooling (higher heat exchanger side thermal resistance). Early in the design process, a targeted cooling performance range was identified as highlighted in Figure 20, which was selected from past experience related to power electronics cooling with WEG.

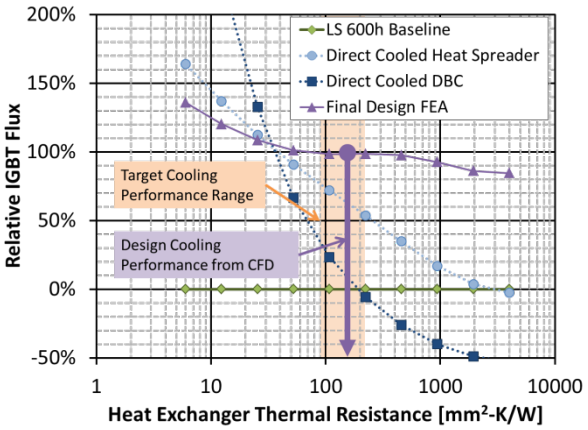

Figure 20: Thermal FEA comparing IGBT heat flux of heat spreader design showing the original target cooling performance range and the final design

The final design was compared against three potential baseline package configurations with the LS 600h package representing the reference. The direct-cooled DBC approach shows significant potential to increase IGBT heat flux, but the improved heat flux is only available with more aggressive

This report is available at no cost from the National Renewable Energy Laboratory (NREL) at www.nrel.gov/publications.

cooling that exceeded our targets for the cooling performance range. The direct-cooled heat spreader configuration shows a performance increase over the LS 600h reference within the targeted cooling performance region, but it does not meet the target of doubling the IGBT heat flux within the target cooling performance range. Through thermal FEA analysis, the final design shows the potential to meet the target to double the heat flux relative to the LS 600h module configuration over the targeted cooling performance region. The heat exchanger cooling performance of the final design obtained from CFD is also shown in Figure 20, showing that it falls within the targeted cooling performance range.

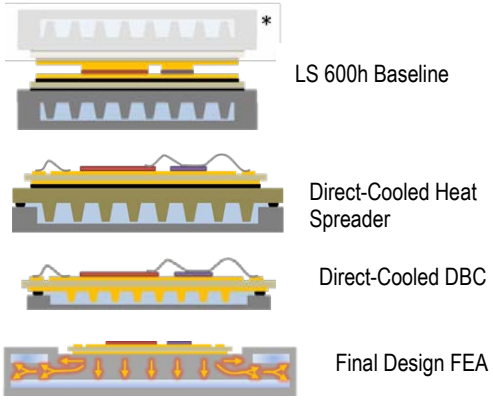

* All packages are compared based on single-sided cooling for consistency.

Figure 21: Package illustrations of configurations highlighted in Figure 20

CFD analysis of the heat exchanger fin geometry was used to design the shape of the flow channels. As mentioned previously, the goal was not to maximize the heat transfer coefficient, but rather to design a heat exchanger within manufacturing constraints to minimize cost while achieving the targeted cooling performance. Figure 22 highlights some of the CFD analyses. Figure 22 shows the fluid flow velocities within the channels. The key result to highlight is the uniform flow velocities within the channels.

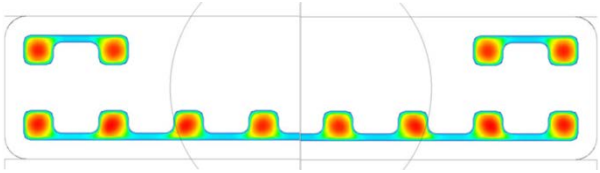

Figure 22: Channel inlet fluid velocity

Experimental Testing

The procedure for validating the simulation results with experimental data was described previously. The results are highlighted below. The experimental validation focused on the heat exchanger flow and temperatures results. Figure 23 compares the difference between the experimental temperature and CFD model temperature within the copper spreader block. The difference between the model and the experimental results was found to be within about 2% over all of the flow rates and heat exchangers tested.

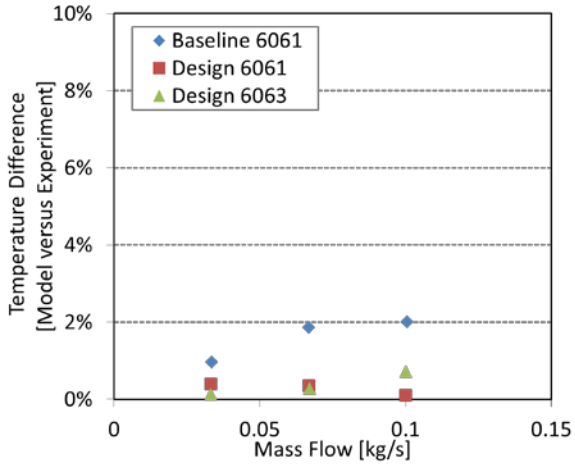

Figure 23: Temperature validation

Figure 24 compares the experimentally measured pressure drop with the CFD model results. The difference between the model and the experimental results was within about 9% across all flow rates and heat exchangers that were tested. With the analysis, it was found that the pressure drop is affected by small variations in the channel geometry. We used a high-resolution digital microscope to measure the manufactured channel dimensions for each heat exchanger and applied the results to the CFD model.

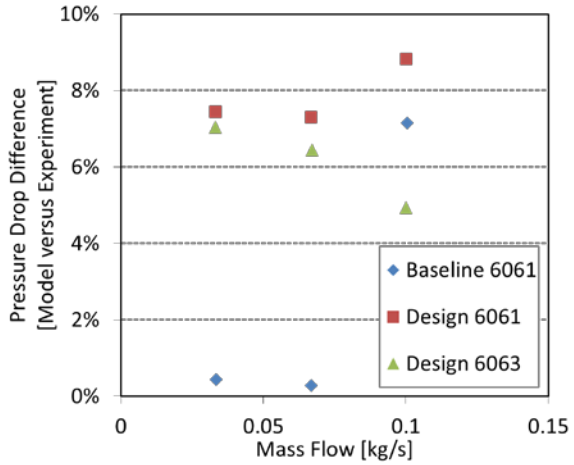

Figure 24: Pressure Drop validation

System-level impacts

The system-level impacts of the heat exchanger design were determined through simulation using the validated heat exchanger CFD model. Figure 25 compares the design against the LS 600h reference package and the baseline aluminum heat exchanger described in Figure 13. The comparison in Figure 25 is at the equivalent flow rate for the LS 600h package (0.0086 kg/s per side of package), which is based on past modeling and analysis efforts. At equivalent flow rate, the design improves the IGBT heat flux by a factor of 1.6 with a slight improvement in

This report is available at no cost from the National Renewable Energy Laboratory (NREL) at www.nrel.gov/publications.

package heat density. When the flow rate is held constant, the pressure drop across the design heat exchanger is significantly lower than the LS 600h reference or the baseline. With the improved heat transfer and reduced pressure drop, the coefficient of performance for the design improves by a factor of 7.9 as compared to the reference LS 600h.

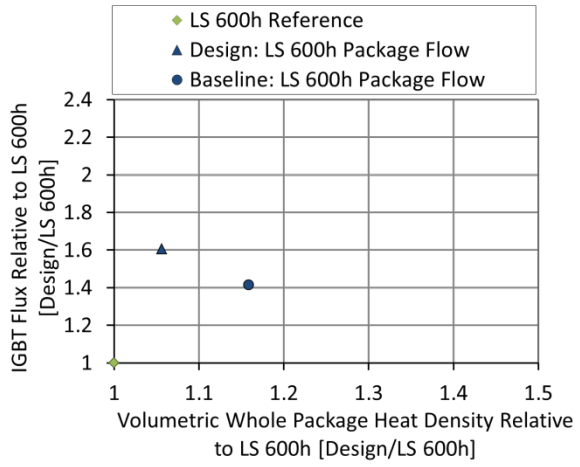

Figure 25: Model results for design and baseline comparison at LS 600h package flow rate

When evaluated at the target system flow rate of 10 L/min in the parallel configuration shown in Figure 19, the design meets the performance targets defined at the beginning of the project. Figure 26 shows the results with 1/6 of the system flow going to each package. The IGBT heat flux improved by about a factor of two, and the package heat density improves over 30%. The design heat exchanger also exceeds the performance of the baseline at the same fluid parasitic power.

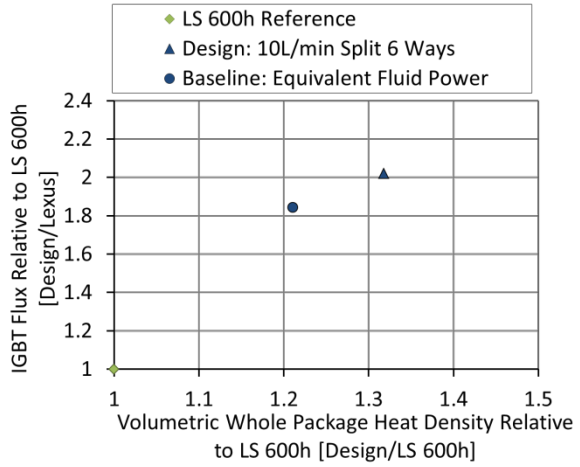

Figure 26: Model results for design at target flow and baseline at equivalent parasitic fluid power

As mentioned previously, the design was based on a parallel arrangement of the heat exchangers as shown in Figure 17 with one package or module per cooling branch. Preliminary investigations were also performed to investigate the impact of series connections on the effective convection coefficient within the channels. Figure 27 compares the average convection coefficient within the channels for three separate heat exchangers connected in series. As seen in Figure 27, the convection coefficient does drop as the flow passes through the first heat exchanger. The convection coefficient appears to stabilize as the flow passes through the second and third heat exchangers. The drop in the convection coefficient would need to be investigated as part of future work depending on the intended application.

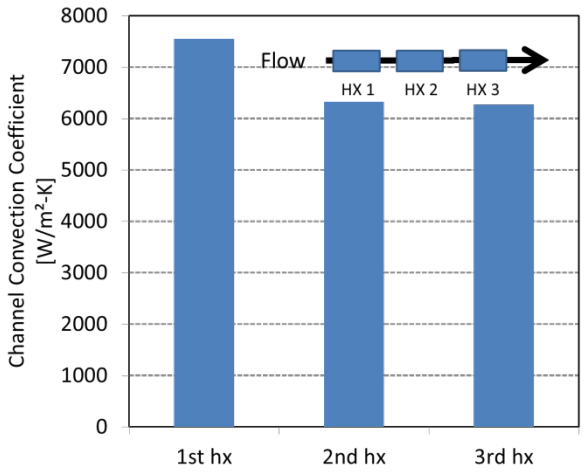

Figure 27: Effective channel convection coefficient in each section

Conclusions and Future Directions

This research project focused on the development and demonstration of a general design concept to enable less aggressive cooling while improving the system-level semiconductor package thermal performance to improve the capability of power semiconductor devices. The improved power capability directly relates to improving the cost per power of the power electronics

The performance of the design was compared against two baseline packages of power semiconductor devices. The design doubled the IGBT heat flux capability of the LS 600h reference with significant improvements in the coefficient of performance. The LS 600h package was selected as the reference because of its best-in-class performance of the modules benchmarked through the APEEM activity. The design also outperformed the baseline direct cooled base plate configuration with similar extruded fin geometry.

The design approach built upon a recently issued patent to enable high performance with less aggressive cooling. Future work could extend the concept to enable other cooling technologies with less effective coolants such as air or automatic transmission fluid. Directly cooling the power electronics with air or automatic transmission fluid could eliminate the dedicated WEG loop for cooling the power electronics and lead to potential cost reductions and elimination of cooling system components. The specific design can go through additional refinement for

This report is available at no cost from the National Renewable Energy Laboratory (NREL) at www.nrel.gov/publications.

specific power electronics applications and this work will be included on future industry collaborations related to cooling power electronics.

FY 2013 Publications/Presentations

1. K. Bennion and J. Lustbader, "Integrated Three-Dimensional Module Heat Exchanger for Power Electronics Cooling," U.S. Patent 20130082377 A10 4-Apr-2013
2. K. Bennion, J. Cousineau, J. Lustbader, "Integrated Power Module Cooling," Presentation at the VTO Annual Merit Review, Crystal City, VA, May 2013.
3. K. Bennion, J. Cousineau, J. Lustbader, "Integrated Module Heat Exchanger," Presentation to the DOE Vehicle Technologies Office Electrical and Electronics Technical Team, Southfield, MI, April 2013.
4. K. Bennion, J. Cousineau, J. Lustbader, "Integrated Module Heat Exchanger," Advanced Power Electronics and Electric Motors FY13 Kickoff Meeting, DOE Vehicle Technologies Office, Oak Ridge, TN, November 2012.

Acknowledgments

The author would like to acknowledge the support provided by Susan Rogers and Steven Boyd, Technology Development Managers for Advanced Power Electronics and Electric Motors, Vehicle Technologies Office, U.S. Department of Energy Office of Energy Efficiency and Renewable Energy. The significant contributions of Justin Cousineau, Jason Lustbader, Mark Mihalic (NREL) and Sapa Extrusions North America to the project are acknowledged.

References

1. Synthesis Partners, LLC, "Technology and Market Intelligence: Hybrid Vehicle Power Inverters Cost Analysis." July 2011.
2. U.S. Drive, "Electrical and Electronics Technical Team Roadmap," Partnership Plan, Roadmaps, and Other Documents, June 2013. Available: http://www1.eere.energy.gov/vehiclesandfuels/pdfs/program/eett_roadmap_june2013.pdf [Accessed: 10-Sep-2013].
3. K. Bennion and J. Lustbader, "Integrated three-dimensional module heat exchanger for power electronics cooling," US20130082377 A104-Apr-2013.
4. H. Yasui, H. Ishiyama, M. Inagaki, K. Mamitsu, and T. Kikuchi, "Power Control Unit for High Power Hybrid System," presented at the 23rd International Electric Vehicle Symposium, Anaheim, California, 2007.
5. M. O'Keefe and K. Bennion, "A Comparison of Hybrid Electric Vehicle Power Electronics Cooling Options," in IEEE Vehicle Power and Propulsion Conference (VPPC), 2007, pp. 116–123.
6. K. Bennion and G. Moreno, "Thermal Management of Power Semiconductor Packages — Matching Cooling Technologies with Packaging Technologies," in IMAPS 2nd Advanced Technology Workshop on Automotive Microelectronics and Packaging, Dearborn, MI, 2010.
7. K. Bennion and K. Kelly, "Rapid modeling of power electronics thermal management technologies," in IEEE Vehicle Power and Propulsion Conference (VPPC), 2009, pp. 622–629.
8. S. Narumanchi, M. Mihalic, K. Kelly, and G. Eesley, "Thermal interface materials for power electronics applications," in 11th Intersociety Conference on Thermal and Thermomechanical Phenomena in Electronic Systems (ITherm), 2008, pp. 395–404.
9. S. Narumanchi, M. Mihalic, G. Moreno, and K. Bennion, "Design of light-weight, single-phase liquid-cooled heat exchanger for automotive power electronics," in 13th IEEE Intersociety Conference on Thermal and Thermomechanical Phenomena in Electronic Systems (ITherm), 2012, pp. 693 –699.
10. R. Skuriat and C. M. Johnson, "Direct substrate cooling of power electronics," in 13th European Conference on Power Electronics and Applications, 2009, pp. 1–10.
11. K. Le, T. G. Ward, B. S. Mann, E. P. Yankoski, and G. S. Smith, "Power electronics substrate for direct substrate cooling," 816977901-May-2012.
12. J. Schulz-Harder, "Efficient cooling of power electronics," in 3rd International Conference on Power Electronics Systems and Applications (PESA), 2009, pp. 1–4.
13. T. Kurosu, K. Sasaki, A. Nishihara, and K. Horiuchi, "Packaging technologies of direct-cooled power module," in International Power Electronics Conference (IPEC), 2010, pp. 2115–2119.
14. R. Bayerer, "Advanced packaging yields higher performance and reliability in power electronics," Langford Lane, Kidlington, Oxford, OX5 1GB, United Kingdom, 2010, vol. 50, pp. 1715–1719.
15. Tien-Yu Lee, "Design optimization of an integrated liquid-cooled IGBT power module using CFD technique," IEEE Trans. Components Packag. Technol., vol. 23, no. 1, pp. 55–60, Mar. 2000.
16. F. Nishikimi and K. Nakatsu, "Power inverter," US8462531 B211-Jun-2013.
17. T. Matsuo, H. Hamada, A. Nishihara, and M. Musou, "Power inverter," 807276006-Dec-2011.
18. D. Harada and H. Ishiyama, "Electric power converter and mounting structure of semiconductor device," 750866824-Mar-2009.
19. C. Gillot, C. Schaeffer, C. Massit, and L. Meysenc, "Double-sided cooling for high power IGBT modules using flip chip technology," *IEEE Trans. Components Packag. Technol.,* vol. 24, no. 4, pp. 698–704, Dec. 2001.
20. T. Burress, C. Coomer, S. Campbell, A. Wereszczak, J. Cunningham, L. Marlino, L. Seiber, and H.-T. Lin, *Evaluation of the 2008 Lexus LS 600H Hybrid Synergy Drive System.* Oak Ridge National Laboratory. ORNL/TM-2008/185, Jan-2009.

This report is available at no cost from the National Renewable Energy Laboratory (NREL) at www.nrel.gov/publications.

21. F. Incropera and D. DeWitt, *Fundamentals of Heat and Mass Transfer,* 4th ed. John Wiley & Sons, 1981.
22. Sapa Extrusions North America. *Design Manual*. 2009.

This report is available at no cost from the National Renewable Energy Laboratory (NREL) at www.nrel.gov/publications.

Advanced Liquid Cooling Research and Development

Principal Investigator: Scot Waye/Sreekant Narumanchi
National Renewable Energy Laboratory (NREL)
Transportation and Hydrogen Systems Center
15013 Denver West Parkway
Golden, CO 80401
Phone: 303-275-4454
E-mail: Scot.Waye@nrel.gov

DOE Technology Development Manager: Susan A. Rogers
Phone: 202-586-8997
E-mail: Susan.Rogers@ee.doe.gov

NREL Task Leader: Sreekant Narumanchi
Phone: 303-275-4062

Start Date: October, 2010
Projected End Date: December, 2013

Objectives

The goal of the project is to design, fabricate, and experimentally demonstrate a light-weight, low-cost, high-thermal-performance, single-phase, water-ethylene glycol (WEG) liquid-cooled heat exchanger. This demonstration is being done within the framework of a commercial inverter from UQM Technologies Inc. The bulk of the heat exchanger is made of plastic material because the cooling is provided by the jets impinging directly on the back side of the power module base plates. Micro-structured surfaces fabricated on the copper base plates will be employed as a simple, passive means of enhancing heat transfer. This cooling approach of impinging jets on the base plate is compared to the baseline channel flow cooling approach typical of automotive heat exchangers.

The objectives for FY2013 were:

- Comprehensive computational fluid dynamics (CFD) analyses will be performed to further optimize and improve heat transfer, reduce pressure drop, and design the second version of the light-weight heat exchanger. Additionally, the use of the MicroCool-enhanced surfaces will be incorporated into the new design to further improve thermal performance. The new, improved designs will be fabricate and their performance will be characterized.
- Additional experiments are initiated planned to evaluate the long-term reliability of enhanced surfaces and ceramic substrates (direct-bond copper [DBC] and direct-bond aluminum [DBA]) subjected to WEG jets. Unlike the prior tests, these experiments will utilize automotive grade coolant (i.e., WEG with corrosion inhibitors) at coolant temperatures used in automotive power electronics applications (70°C). To minimize/eliminate oxidation and corrosion, the enhanced surfaces will be nickel plated. The effect of the impinging jets on the thermal performance of the enhanced surface and the integrity of the ceramic substrate will be evaluated over a one-year period.

Technical Barriers

Since it is a new technology or application for automotive power electronics, acceptance relies on proof of reliability of cooling technology performance and materials selected. The manufacturing processes of the heat exchanger must also be cost effective.

Technical Targets

This project is helping towards achieving 2015 and 2020 DOE Advanced Power Electronics and Electrical Motors (APEEM) Program goals (cost, power density, and specific power) for power electronics using high-temperature WEG coolant.

Accomplishments

- A jet impingement-based heat exchanger was fabricated out of high-temperature plastic and tested to characterize its thermal performance. Although the prototype was machined, it is possible to fabricate it with injection molding. CFD models were validated with the experimental data. Modeling at inverter-level power predicted full inverter thermal performance.
  - For the experiments, with 105 W heat dissipated, the thermal resistance was 5% lower for impingement on a plain surface and 13% lower for impingement on the microfinned-enhanced surface compared to the baseline, channel-flow-based heat exchanger.
  - Through modeling, with 2,520 W heat dissipated, the thermal resistance was 9% lower for impingement on a plain surface and 32% lower for impingement on the microfinned-enhanced surface.
  - Due to the reduction in weight and increased thermal performance, the specific power (kW/kg) increased up to 78% and the power density (kW/L) increased up to 47% (both values for the enhanced surface).
- Reliability testing indicated that the jet nozzle diameter does not change due to wear or clogging. Reliability testing for the enhanced surface thermal performance and DBC and DBA properties is ongoing.

✧ ✧ ✧ ✧ ✧

Introduction

Reducing cost and increasing power density and specific power are some of the key objectives of the DOE APEEM Program to meet the 2015 and 2020 Program targets and to

This report is available at no cost from the National Renewable Energy Laboratory (NREL) at www.nrel.gov/publications.

help increase market penetration of electric-drive vehicles. Thermal management techniques can be used to help achieve the overarching goals of the program. The objective of this work is to design, develop, characterize, and demonstrate a light-weight, low-cost, inverter-scale (based on a commercially available inverter) single-phase liquid-cooled (with WEG, [50%–50% mixture by volume] coolant) heat exchanger/cold plate, which is a significant improvement over conventional channel-flow-based heat exchangers. Single-phase liquid jets have been studied extensively in the literature [1-4]. These studies include experiments, theoretical analyses, and numerical simulations. Different configurations of impinging jets have been studied, including single free-surface jets [5], multiple free-surface jets [6-8], single submerged jets [5, 9, 10], multiple submerged jets [6, 9], and confined single submerged jets [3, 11-13]. Both planar and circular jets have been studied. In the context of electronic cooling, a large number of experimental correlations have been developed for the local and average heat transfer coefficients on the surface of the simulated chip [1-3]. Most of the simulated chips are either 10 mm^2 x 10 mm^2 or 12.7 mm^2 x 12.7 mm^2. Air jets have also been studied extensively [9]. Some of the non-dimensional heat transfer correlations developed from studies on air jets [9] can be applied to liquid jets also. Researchers have explored the impact of a vast array of parameters—such as jet velocity, jet diameter, impact angle, nozzle-to-chip spacing, nozzle-to-nozzle spacing, turbulence levels, nozzle shapes, nozzle length, jet pulsations, jet confinement, chip-surface enhancement, and fluid properties—on the chip-surface heat transfer coefficients. All these are covered in detail in comprehensive reviews [1-3, 9].

Moreover, studies have demonstrated that jet impingement heat transfer can be further enhanced through the use of surface roughening techniques for both liquid and air jets [14-17]. Gabour and Lienhard [15] investigated the impact of surface roughness on jet impingement heat transfer. Their results demonstrated that stagnation-point heat transfer increases with increasing roughness with the roughest surface producing 50% greater heat transfer as compared to the baseline surface. Moreover, the roughness enhancement increased with increasing Reynolds numbers. The enhancement was associated with the roughness structures protruding through the thermal boundary layer within the stagnation zone. Sullivan et al. [16] also reported enhancement using roughened heat sources in the submerged jet configuration. In the study [16], the heat transfer enhancements of the roughened surfaces were associated with mechanisms occurring within the wall jet region. It was speculated that roughened surfaces increased heat transfer by advancing transition to turbulent flow and by disrupting the viscous sub-layer within the turbulent region. The heat transfer performance on a 12.7-mm-diameter copper target surface of a number of enhanced surface configurations were presented in [17. The study [17] demonstrated the superior performance of the configuration of submerged/flooded jets impinging on a microfinned surface with respect to impingement on a plain surface as well as impingement on a number of other enhanced surfaces. These results were also noteworthy because of the feasibility of the submerged/flooded jet configuration for practical applications [18, 19].

In automotive power electronics, it is important to reduce cost and increase power density and specific power to help make electric-drive vehicles more cost effective and increase their market acceptance and penetration. Traditionally, channel flow-based cold plates using a WEG mixture (50%–50% by volume) are widely used in a majority of hybrid electric vehicles for cooling power electronics components [20].

Approach

Light-Weight Heat Exchanger

Design and Fabrication

Building on lessons learned from the first prototype fabrication and testing [21], a second prototype heat exchanger utilizing a submerged jet-impingement cooling approach and a light-weight plastic material was fabricated using a machining process. The two main differences of this prototype from the first prototype are the material and manufacturing process, and the flow path. The first prototype was a heat exchanger consisting of a fluid-manifold that was fabricated using a selective-laser-sintering rapid prototyping process using automotive-grade glass-fiber-reinforced nylon plastic. The second prototype was machined from Delrin, a high-temperature plastic, although this part could be injection molded from a variety of high-temperature plastics. The first prototype heat exchanger replaced the channel-flow with jets to impinge on the module surfaces. No other changes were made to the flow path from the baseline design. The second prototype removed unnecessary flow path to reduce the pressure drop, which increased with the introduction of the jets compared to the channel-flow technology.

The first prototype heat exchanger, shown in Figure 1, was designed to cool a commercially available inverter from UQM Technologies Inc. The new heat exchanger design implements a light-weight manifold that incorporates liquid jets directly impinging on the power module base plates. The second prototype heat exchanger, shown in Figure 2, shows the reduction in flow path with respect to the first prototype, as well as the jet nozzles. Parts of the manifold have been omitted from fabrication for ease of testing (for example, the platform for the capacitor bank). The jet impingement cooling approach eliminates the use of thermal interface material between the base plate and the heat sink/cold plate, and therefore is expected to improve thermal performance. Further details on the CFD modeling and design are given in [22].

Experimentation

Experiments were conducted to characterize the performance of the new heat exchanger, as seen in Figure 3.

Previous experiments have characterized the first prototype as well as the baseline channel-flow-based aluminum heat exchanger. The tests were carried out using WEG (50%–50% mixture by volume) as the coolant at a temperature of 70°C. An industry-standard flow rate of 10 L/min (1.67×10^{-4} m^3/s) as well as 2, 5, and 8 L/min were examined for the various heat exchangers. For these

This report is available at no cost from the National Renewable Energy Laboratory (NREL) at www.nrel.gov/publications.

experiments, the diodes on one power module were powered, and their temperature was measured using a transient thermal tester. Based on the information of diode junction temperature as well as the total power dissipated in the diodes, the total thermal resistance was computed.

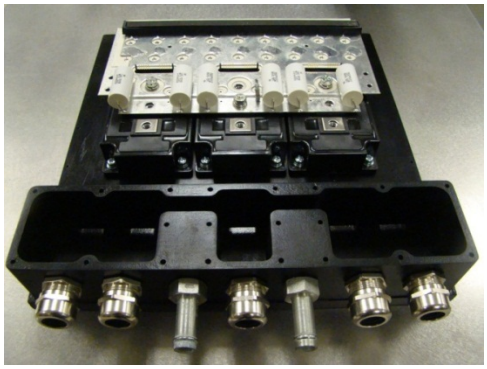

Figure 1: First light-weight, inverter-scale plastic heat exchanger prototype (Photo credit: Mark Mihalic, NREL).

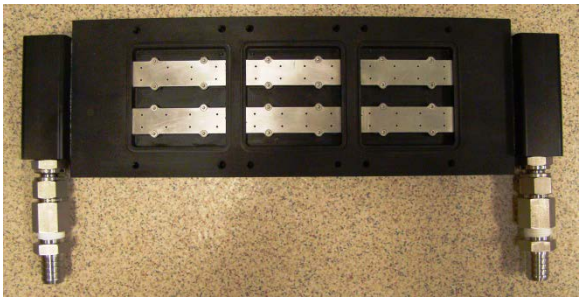

Figure 2: Second light-weight, inverter-scale plastic heat exchanger prototype (Photo credit: Scot Waye, NREL).

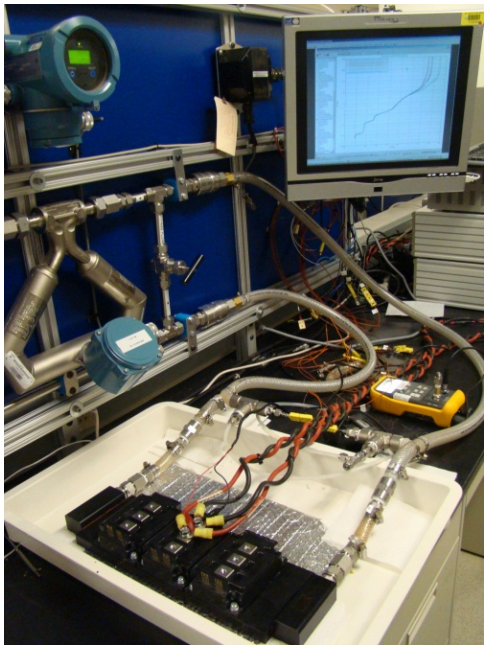

Figure 3: Second prototype testing on the WEG loop (Photo credit: Scot Waye, NREL).

For the second prototype heat exchanger experiments, two sets of modules were used. The first set had plain copper base plates. The second set had microfinned surface enhancement located under each insulated gate bipolar transistor (IGBT)/diode pair, as seen in Figure 4, with a close-up of the microfinned surface.

Full-scale inverter testing will be conducted using a dynamometer to simulate a real-world thermal load profile. The experimental results will be compared to full inverter power modeling results for the baseline and jet impingement-based heat exchangers.

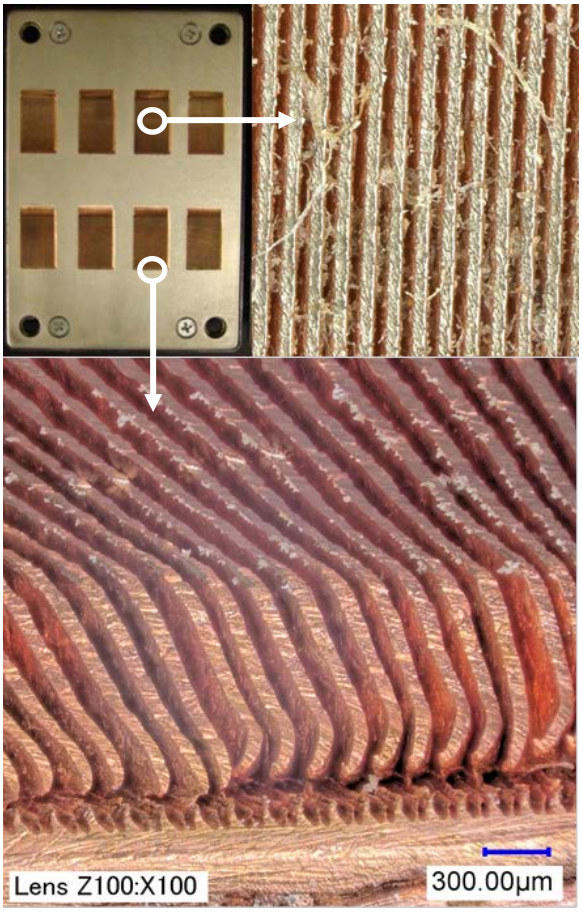

Figure 4: Wolverine Tube MicroCool finned surface technology on module (top left) and close-up (top right and bottom) (Photo credits: Scot Waye, Mark Mihalic, Gilbert Moreno, NREL).

Modeling

Through validated CFD modeling (via experiments), the improvement in thermal and overall performance of the impinging jet designs were analyzed at full power (2.5 kW) compared to the baseline channel-flow-based heat exchanger.

A CFD model was created using the same geometry and properties as the experimental setup. Using the experimental data obtained with four diodes powered to produce approximately 105 W of heat, the thermal resistance was matched in the model by adjusting the solder layer resistance for the jet-impingement cases and the thermal grease layer resistance for the channel flow cold plate case. The thickness and resistance of the solder and grease layers were unknown previously.

This report is available at no cost from the National Renewable Energy Laboratory (NREL) at www.nrel.gov/publications.

A k-ω turbulence model was used. The grid was adapted to yield a y+ (non-dimensional distance of grid centroids) of less than one on the impinging surface, and the average and maximum device temperatures were monitored. (All residuals were set to 10^{-3} except for energy, which was set to 10^{-6}).

All of the 24 IGBTs and 24 diodes were powered at a two-to-one ratio, yielding a heat generation rate of 1.944×10^9 W/m^3 (70 W per device) for the IGBTs and 2.12×10^9 W/m^3 (35 W per device) for the diodes, yielding 2,520 W of total heat dissipation.

A flow rate of 10 L/min for WEG at 70°C was used for the simulations. To predict the thermal performance for the micro-finned enhanced surfaces, the flow rate was doubled to double the jet velocity. Previous research [22] found that for the microfinned surface enhancement used, the heat transfer coefficient at 10 L/min with the enhanced surface was approximately the same as the coefficient at 20 L/min for a plain surface.

Reliability

Experiments were conducted to evaluate the long-term reliability of Wolverine's MicroCool enhanced surfaces and DBA and DBC substrate samples.

Previous reliability testing run over a 12-month period used 35°C WEG free jets at 2, 5, and 12 m/s on unplated microfinned surfaces. Results showed no degradation in nozzle diameter and a decrease in thermal performance on the microfinned surfaces at high velocities due to oxidation.

Additional reliability tests are running using a 65°C automotive grade WEG on two nickel-plated microfinned surfaces, three DBA substrates, and three DBC substrates at 5 m/s. A schematic of the test apparatus is shown in Figure 5. Near-continuous jet impingement testing has been performed for approximately four months.

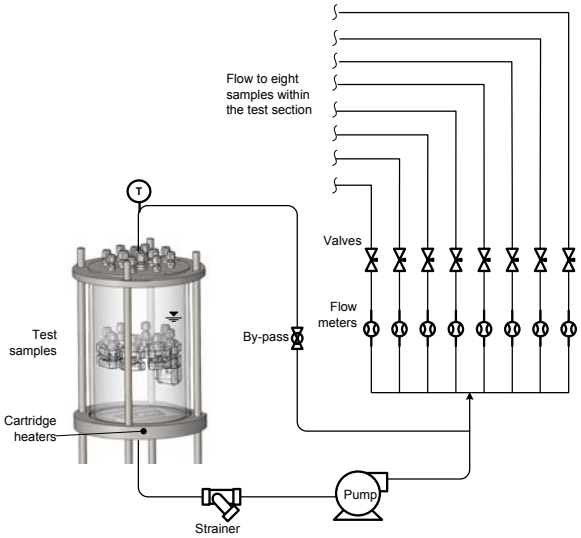

Figure 5: Test setup for long term reliability tests.

The Delphi DBA and DBC substrate samples are examined with several testing metrics (see Figure 6). Digital microscope images will examine surface characteristics and provide an overall qualitative comparison. A scanning acoustic microscope (CSAM) images layers below the surface, including the substrate interfaces. Laser profilometry examines the surface roughness and shape. Xenon flash is used to measure the thermal diffusivity.

The two Wolverine MicroCool nickel-plated samples are characterized using digital microscopy for surface images, and the heat transfer coefficient will be measured.

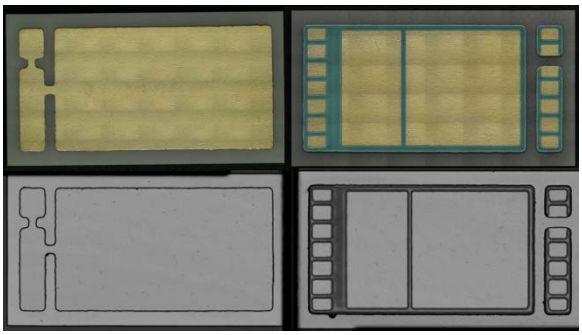

Figure 6: Digital images of the DBA top (top left) and bottom (top right); C-SAM images of the DBA top (lower left) and bottom (lower right) (Photo credit: Jana Jeffers, NREL).

Collaborations

For this project, NREL established collaborations with UQM Technologies Inc., which provided the baseline heat exchanger and will be assisting in full invertor testing using a dynamometer; Wolverine Tube Inc., which manufactured the microfinned enhanced surfaces; and Delphi, which provided DBC and DBA samples for reliability testing.

Results

Heat Exchanger Experimentation

Experimentation using a transient thermal tester yields structure functions which provide information on the thermal capacitance and the thermal resistance, which can ultimately be used to determine the thermal resistance of the passive stack and the cooling approach. By examining all the structure functions together regardless of flow rate or cooling strategy (channel flow cold plate, impingement on plain surfaces, impingement on enhanced surfaces), the point where the structure functions diverge indicates the boundary between the passive stack in the module and the convective cooling technology. For the PowerEx modules used in this testing, the thermal resistance of the passive stack was approximately 0.09 K/W.

For 8-L/min and 10-L/min flow rates, the junction to liquid thermal resistances ($R_{th,j\text{-}l}$ [K/W]) and percent reduction as compared to the baseline channel flow cold plate are provided in Table 1. The structure functions for various heat exchanger configurations at 10 L/min are given in Figure 7.

This report is available at no cost from the National Renewable Energy Laboratory (NREL) at www.nrel.gov/publications.

Table 1: Thermal resistance, $R_{th,j\text{-}l}$ [K/W] and improvement over channel flow heat exchanger for 8 L/min and 10 L/min: (1) designates first prototype, (2) designates the second prototype.

	Channel Flow	Jet/Plain (1)	Jet/Plain (2)		Jet/Microfinned (2)		
Target distance (mm)		0.5	0.5	1.95	0.3	1.75	3.475
			Resistance, $R_{th,j\text{-}l}$ [K/W]				
8 L/min	0.139		0.136	0.143	0.126	0.126	0.128
10 L/min	0.136	0.128	0.129	0.136	0.122	0.119	0.122
			Improvement over baseline				
8 L/min			2.2%	-2.9%	9.4%	9.4%	7.9%
10 L/min		5.9%	5.1%	0.0%	10.3%	12.5%	10.3%

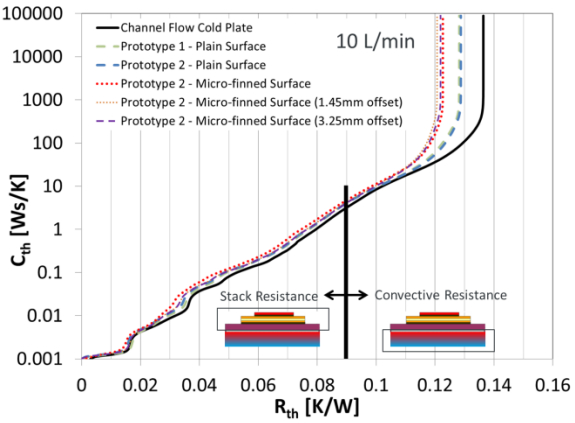

Figure 7: Structure functions of heat exchangers showing thermal resistance (x-axis) of various cooling technologies.

The test cases included the channel flow, the first prototype jet-impingement heat exchanger with plain surfaces, and the second prototype jet-impingement heat exchanger with plain and microfinned enhanced surfaces. For the jet-impingement heat exchangers, the nozzle-to-baseplate distance (target distance) was also examined. The nominal target distance was 0.5 mm. Offsets of 1.45 mm and 3.25 mm were introduced, yielding a 1.95 mm target distance for the plain surface. For the microfinned enhanced surface, the microfins extended approximately 200 µm into the flow, reducing the jet length to 1.75 mm and 3.475 mm with the two offsets, respectively.

For the plain surface, increasing the nozzle-to-target distance decreases the thermal performance. For the enhanced surface, the thermal performance slightly increases with increasing target distance, but as the target distance increases further, the thermal performance is reduced. The interaction of the jet with the surface to create a thin boundary layer and turbulence are important aspects to transfer the heat from the solid into the fluid. For very low velocities (flow rate and jet nozzle diameter) and large target distances, the momentum of the jet decreases and the jet core spreads, decreasing heat transfer on the surface. For enhanced surfaces, there is an optimal distance depending on the jet characteristics.

The thermal performance for the first and second prototypes with jets impinging on plain surfaces is nearly the same, which is expected due to keeping the jet design the same between iterations. For the jet-impingement on a plain surface heat exchanger, the thermal resistance was reduced by 5.1%. On the microfinned surface, the reduction was 12.5% at the best target distance and 10.3% at the nominally designed distance (0.5 mm).

The resistance of the passive stack was approximately 0.09 K/W. By subtracting this resistance from the total resistance, the convective resistance (the resistance from the solid to the fluid) ($R_{th,hx}$ [K/W]), or the part that is controlled by the heat exchanger design, is 15.2% lower for jet impingement on plain surfaces, and 37.0% lower for jet-impingement on microfinned enhanced surfaces. Additional reduction to the junction to liquid resistance can be achieved by more aggressive cooling strategies or reducing the resistance in the passive stack.

Table 2 shows the experimental pressure drop across the various heat exchanger designs at 8 L/min and 10 L/min. As previously discussed, the first prototype had a large increase in pressure loss due to the introduction of the jets. By removing unnecessary flow path in the second prototype, the pressure loss was closer to the baseline channel flow heat exchanger. Therefore, the improvement in the coefficient of performance, defined as the inverse product of the junction to liquid thermal resistance and the fluid power, was nearly the same for the jet impingement on the plain surface heat exchanger and 13% for the jet impingement on the microfinned surfaces heat exchanger.

Table 2: Experimental pressure drop across heat exchanger [Pa]. (1) denotes first prototype, (2) denotes second prototype.

	Channel Flow	Jet/Plain (1)	Jet/Plain (2)	Jet/Microfinned (2)
8 L/min	12,686		13,221	12,755
10 L/min	19,598	24,407	20,581	19,995

This report is available at no cost from the National Renewable Energy Laboratory (NREL) at www.nrel.gov/publications.

Table 3: Thermal Resistance and Device Temperatures for Modeled Heat Exchangers. *Flow rate doubled to match heat transfer coefficient of microfinned enhanced surface.

	Flow rate [L/min]	ΔP [Pa]	$T_{avg,devices}$ [K]	$R_{th,j\text{-}l}$ [K/W]	$T_{max,devices}$ [K]	$R_{th,j\text{-}l}$ [K/W]
Channel Flow Cold Plate	10	17,891	391.6	0.0192	395.8	0.0209
Jet/Plain (1)	10	20,800	386.7	0.0173	390.6	0.0188
Jet/Microfinned (1)	20*		376.6	0.0132	380.1	0.0147
Jet/Plain (2)	10	18,732	387.2	0.0174	391.2	0.0190
Jet/Microfinned (2)	20*		376.2	0.0131	380.2	0.0147

Heat Exchanger Modeling

Flow rates, pressure drops, average and maximum temperatures and junction to liquid thermal resistances based on the respective temperatures are given in Table 3.

The focus of the modeling was on a power ratio of two to one for the IGBTs and diodes for a total power of 2,520 W. Power ratios of one-to-one and three-to-one were also examined as well as total heat dissipation of 1,152 W and 3,456 W. In general, the overall resistance of the inverter remains the same at these three power levels.

The thermal resistance for the jet-impingement heat exchanger was reduced by 9% and 32% for the plain and microfinned surfaces, respectively. The average and maximum temperatures of the devices were reduced by approximately 5°C (Figure 8) and 15°C for the plain and microfinned surfaces with jet impingement, respectively, as compared to the baseline heat exchanger.

The channel flow heat exchanger removes heat from the aluminum plate via the fluid. The locations of the modules and devices are not as critical for the channel flow heat exchanger compared to the jet impingement configuration, as the aluminum acts as a heat sink. For the jet impingement heat exchanger, the aluminum cold plate is removed and the jets impinge directly on the module copper baseplate. This localized and directed cooling creates high local heat transfer coefficients where the heat is the highest, under the devices, as shown in Figure 9.

The reduction in thermal resistance from junction to liquid is greater for full inverter power than the partial power used in the experiments because the resistance is subject to not only the convective cooling resistance, which relies on the cooling strategy or technology, but also the heat flux magnitude and distribution. As the heat seeks the path of least resistance, as illustrated in Figure 10, either due to a low convective cooling resistance at the solid-fluid interface or the absence of multiple heat generating devices, it will manifest as a lower thermal resistance due to reduced heat spreading.

The coefficient of performance improves by up to 5% and 40%, specific power increases 29% and 55%, and power density increases 6% and 28% over the baseline for the plain and microfinned surfaces with jet impingement, respectively.

A 9% decrease in thermal resistance allows for 10% more heat to be dissipated. Using basic analytical equations for devices, this correlates to an approximate 6% increase in power per device area, or a 6% decrease in device area per power by varying only the current. Therefore, 6% of the device area (such as silicon) or number of devices could theoretically be removed, creating a cost savings. For example, a 32% decrease in thermal resistance translates to an approximate device area reduction of 22%.

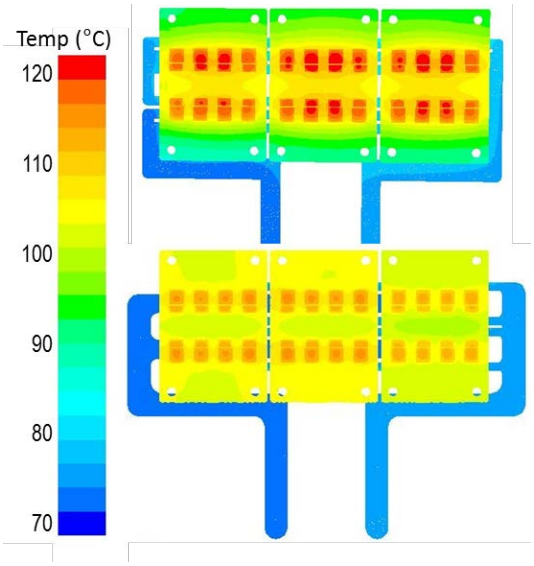

Figure 8: Temperatures of modules for baseline (top) and jet impingement on the plain surface for the first prototype (bottom). The second prototype has similar thermal performance.

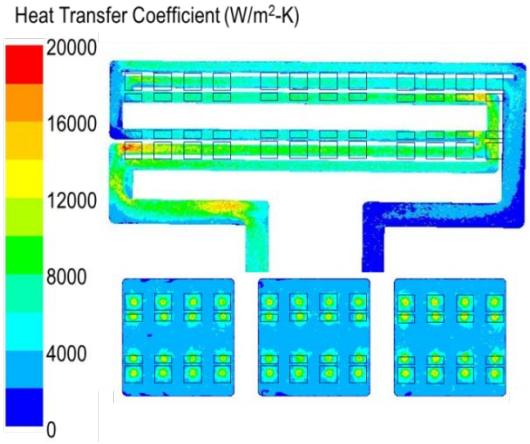

Figure 9: Heat transfer coefficient at the solid-fluid interface for baseline (top) and jet impingement on the plain surface of the first prototype (bottom). The second prototype has similar thermal performance.

This report is available at no cost from the National Renewable Energy Laboratory (NREL) at www.nrel.gov/publications.

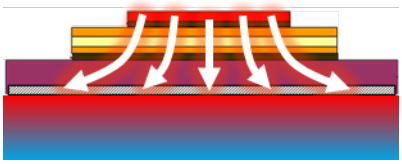

Figure 10: Heat spreading from junction to liquid.

Reliability

The reliability experiments have been running for almost four months. After 60 and 120 days, the samples were examined and potential defects were noted to observe closely as testing progresses. Because the entire substrate is submerged, there is a possibility of degradation from a reaction between the ceramic substrate and the WEG, which will be monitored (under normal operating conditions, one side may be exposed to WEG, but not completely submerged). Concerns of a reaction between the ceramic layers and WEG were realized. After 120 days, two DBA samples have severe degradation, possibly from a chemical reaction between the ceramic layers and the WEG. Reliability of jet impingement on the face of the substrate is the objective, so a completely submerged substrate may have caused unintended results. After 60 days, the thermal diffusivity of the substrate samples did not change outside of the uncertainty of the measurement. After 120 days, the thermal diffusivity is decreasing, especially for DBA1 and DBA3, which were the two samples that had degradation, as seen in Figure 11.

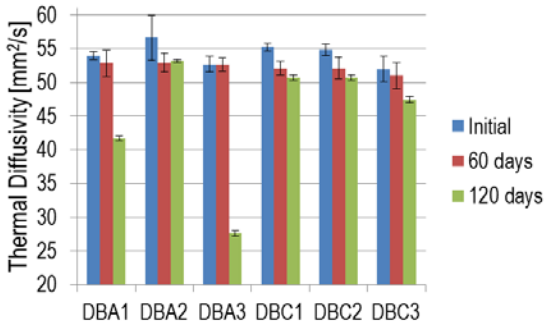

Figure 11: Thermal diffusivity of DBA and DBC substrates. Error bars represent a standard deviation of five measurements.

Conclusions and Future Directions

- A new light-weight heat exchanger designed to cool a commercially available inverter was fabricated.
- Experiments at low power demonstrate that the new heat exchanger can reduce the thermal resistance by 5% to 13% with plain and microfinned-enhanced surfaces, respectively, with respect to a baseline channel flow-based heat exchanger.
- CFD modeling at inverter power projects thermal resistance reductions of 9% and 32% for plain and micro-finned-enhanced surfaces, respectively. Along with a weight reduction of approximately 3 kg, specific power is improved by up to 78%, and power density by 47% as compared with the baseline, channel-flow-based heat exchanger design.
- The fabrication of the new heat exchanger out of light-weight plastic may also provide additional cost savings associated with inexpensive materials and cost-effective manufacturing techniques.
- Experiments were conducted to evaluate the reliability of the Wolverine MicroCool enhanced surfaces and DBA and DBC substrates when subjected to near-continuous impinging WEG jets. Testing is ongoing.
- Inverter-level experiments using a dynamometer are planned to characterize the improvement in thermal performance for the jet impingement heat exchanger compared to the baseline.

FY 2013 Publications/Presentations

1. Narumanchi, S. “Advanced Liquid Cooling R&D.” Presentation/Poster, DOE Annual Merit Review; May 13–15, 2013, Arlington VA.

Acknowledgments

The author would like to acknowledge the support provided by Susan Rogers and Steven Boyd, Technology Development Managers for Advanced Power Electronics and Electric Motors, Vehicle Technologies Office, U.S. Department of Energy Office of Energy Efficiency and Renewable Energy. The significant contributions of Sreekant Narumanchi, Mark Mihalic, Gilbert Moreno, Jana Jeffers and Kevin Bennion (NREL) to the project are acknowledged. The author would also like to acknowledge Jon Lutz (UQM) for providing very useful information on the UQM inverter, Sy-Jenq Loong (Wolverine Tube Inc.) for providing microfinned surface enhancements, as well as Ralph Taylor (Delphi) for providing the DBA/DBC substrates.

References

1. Webb, B.W., Ma, C.-F., “Single-phase liquid jet impingement heat transfer,” *Advances in Heat Transfer,* **26**, pp. 105–217, 1995.
2. Lienhard, J.H., “Liquid jet impingement,” *Annual Review of Heat Transfer*, pp. 199–270, 1995.
3. Garimella, S.V., “Heat Transfer and flow fields in confined jet impingement,” *Annual Review of Heat Transfer,* pp. 413–494, 2000.
4. Narumanchi, S.V.J., Amon, C.H., Murthy, J.Y., “Influence of pulsating submerged liquid jets on chip-level thermal phenomena,” *ASME Journal of Electronic Packaging,* **125**, pp. 354–361, 2003.
5. Womac, D.J., Ramadhyani, S., Incropera, F.P., “Correlating equations for impingement cooling of small heat sources with single circular liquid jets,” *ASME Journal of Heat Transfer,* **115**, pp. 106–115, 1993.

This report is available at no cost from the National Renewable Energy Laboratory (NREL) at www.nrel.gov/publications.

6. Womac, D.J., Incropera, F.P., Ramadhyani, S., "Correlating equations for impingement cooling of small heat sources with multiple circular liquid jets," *ASME Journal of Heat Transfer,* **116**, pp. 482–486, 1994.
7. Pan, Y., Webb, B.W., "Heat transfer characteristics of arrays of free-surface liquid jets," General Papers in Heat and Mass Transfer, Insulation and Turbomachinery, ASME, HTD - Vol. 271, pp. 23–28, 1994.
8. Yonehara, N., Ito, I., *Cooling characteristics of impinging multiple water jets on a horizontal plane*, Technical Report - Kansai University. pp. 267-28, 1982.
9. Martin, H., "Heat and mass transfer between impinging gas jets and solid surfaces," *Advances in Heat Transfer*, **13**, pp. 1–60, 1977.
10. Wadsworth, D.C., Mudawar, I., "Cooling of a multichip electronic module by means of confined two-dimensional jets of dielectric liquid," *ASME Journal of Heat Transfer,* **112**, pp. 891–898, 1990.
11. Garimella, S.V., Rice, R.A., "Confined and submerged liquid jet impingement heat transfer," *ASME Journal of Heat Transfer,* **117**, pp. 871–877, 1995.
12. Garimella, S.V., Nenaydykh, B., "Nozzle-geometry effects in liquid jet impingement heat transfer," *International Journal of Heat and Mass Transfer,* **39**(14), pp. 2915-2923, 1996.
13. Li, C.-Y., Garimella, S.V., "Prandtl-number effects and generalized correlations for confined and submerged jet impingement," *International Journal of Heat and Mass Transfer,* **44**, pp. 3471-3480, 2001.
14. Incropera, F.P., *Liquid cooling of electronic devices by single-phase convection,* John Wiley & Sons, Inc., 1999.
15. Beitelmal, A.H., Saad, M.A., Patel, C.D., "Effects of surface roughness on the average heat transfer of an impinging air jet," *International Communications in Heat and Mass Transfer*, **27**(1), pp. 1–12, 2000.
16. Gabour, L.A., Lienhard, J. H.V., "Wall roughness effects on stagnation-point heat transfer beneath an impinging liquid jet," *Journal of Heat Transfer*, **116**(1), pp. 81–87, 1994.
17. Sullivan, P.F., Ramadhyani, S., Incropera, F.P., "Use of smooth and roughened spreader plates to enhance impingement cooling of small heat sources with single circular liquid jets," San Diego, CA, USA, 206-2, pp. 103–110, 1992.
18. Moreno, G., "Characterization and development of advanced heat transfer technologies," FY2010 DOE Thermal Management of Advanced Power Electronics and Electrical Motors Annual Report, 2010.
19. Hassani, V., Vlahinos, A., Bharathan, D., "Low thermal resistance power module assembly," United States Patent Number 719058, 2007.
20. Narumanchi, S.V.J., Hassani, V., Bharathan, D., *Modeling single phase and boiling liquid jet impingement cooling in power electronics*, NREL Technical Report, NREL/TP-540-38787, http://www.nrel.gov/docs/fy06osti/38787.pdf, 2005.
21. Electrical and Electronics Technical Team Roadmap, http://www1.eere.energy.gov/vehiclesandfuels/pdfs/program/eett_roadmap_june2013.pdf, 2013.
22. Narumanchi, S. "Light-Weight, Single-Phase, Liquid-Cooled Heat Exchanger," FY2012 DOE Advanced Power Electronics and Electric Motors 2012 Annual Progress Report, 2012, pp. 193-197.
23. Narumanchi, S., Mihalic, M., Moreno, G., and Bennion, K., 2012, "Design of light-weight, single-phase, liquid-cooled, jet-based heat exchanger for an automotive inverter," Proceedings of the 2012 ITherm conference, San Diego, CA May 2012.
24. Moreno, G., Narumanchi, S., Venson, T., and Bennion, K., 2013, "Micro-structured surfaces for single-phase jet impingement heat transfer enhancement," *ASME Journal of Thermal Science and Engineering Applications*, **5**, pp.031004-1 – 031004-9.

This report is available at no cost from the National Renewable Energy Laboratory (NREL) at www.nrel.gov/publications.

Two-Phase Cooling of Power Electronics

Principal Investigator: Gilbert Moreno
National Renewable Energy Laboratory (NREL)
Transportation and Hydrogen Systems Center
15013 Denver West Parkway
Golden, CO 80401
Phone: 303-275-4450
E-mail: Gilbert.Moreno@nrel.gov

DOE Technology Development Manager: Susan A. Rogers
Phone: 202-586-8997
E-mail: Susan.Rogers@ee.doe.gov

NREL Task Leader: Sreekant Narumanchi
Phone: 303-275-4062

Start Date: October 2010
End Date: September 2014

Objectives

The overall project goal is to enable the U.S. Department of Energy (DOE) Advanced Power Electronics and Electric Motors (APEEM) Program's power electronics specific power, power density, and cost targets to be achieved through the use of two-phase cooling technology. Specific project objectives are listed below.

- Characterize and compare the performance of new candidate refrigerants for use in the two-phase–based cooling systems.
- Explore techniques to enhance two-phase heat transfer coefficients and critical heat flux (i.e., dry out).
- Demonstrate a compact, inverter-scale passive two-phase cooling system capable of dissipating automotive power electronic heat loads. Quantify the system's metrics including thermal performance, coefficient-of-performance, mass, and volume and compare them those of conventional automotive power electronics cooling systems.

Technical Barriers

Two-phase cooling is well known to provide very high heat transfer capacity as compared to other forms of cooling [1]; however, concerns regarding reliability and cost of two-phase–based cooling systems hinder their implementation within automotive-based applications. In this project, we attempt to demonstrate a two-phase cooling solution for automotive power modules based on a passive and indirect cooling strategy. The indirect cooling strategy eliminates direct contact of the refrigerant with the electronics and thus eliminates material compatibility issues. Moreover, this approach also eliminates electrical feed-through penetrations that may pose a refrigerant leakage potential. The passive approach (i.e., no compressor or pump) simplifies the system, which has implications for reduced cost and increased efficiency. Although not the conventional method of cooling automotive power electronics, passive two-phase cooling solutions have been used to cool power electronic components (Gate-Turn-Off thyristors) in mining haul truck and high-speed train systems [2-5].

Technical Targets

This project aims to enable achieving the DOE APEEM targets listed below by significantly improving thermal management:

- Power Density
- Specific Power
- Efficiency
- Cost.

Accomplishments

- We fabricated a proof-of-concept passive two-phase cooling system (evaporator and condenser) designed to cool six Delphi discrete power modules. We experimentally demonstrated that the cooling system could dissipate at least 2.7 kW of heat with 250 mL (330 grams) of the refrigerant hydrofluorocarbon (HFC)-245fa.
- We identified techniques to improve the thermal performance and reduce the weight and size of the evaporator. A Record of Invention describing these innovations was submitted. The new evaporator design combined with an improved condenser will constitute the second-generation power electronics two-phase cooling system. Tests are planned to fully characterize the performance of this system.
- We initiated experiments to evaluate the long-term reliability of enhanced surface coatings.

Introduction

An efficient thermal management strategy can be an effective means of reducing the size and cost of electronics as well as improving performance and reliability. In this project, we are evaluating two-phase heat transfer as a means of cooling automotive power electronics. The high heat transfer rates and isothermal characteristics of two-phase heat transfer allow for increased power density and specific power, which may enable achieving the DOE APEEM Program technical targets. The intent is to demonstrate superior thermal performance, increased efficiency, reduced weight and volume with the two-phase cooling system(s) developed. Passive (pump-less) two-phase systems with an air-cooled condenser will be developed due to their inherent efficiency and simplicity.

Approach

In this project, we performed both fundamental and system-level research to evaluate two-phase (boiling/evaporation) heat transfer as a potential power electronics cooling solution. Figure 1 depicts the strategy for this project. As shown, initial research efforts were focused on characterizing the pool boiling

This report is available at no cost from the National Renewable Energy Laboratory (NREL) at www.nrel.gov/publications.

performance of novel coolants/refrigerants as well as investigating promising boiling enhancement techniques. These fundamental research results then fed into the design of the system-level components. The system-level study is focused on developing a prototype passive two-phase cooling system capable of dissipating automotive power electronic heat loads. Small-scale experiments were first conducted to understand and improve the performance of a passive two-phase cooling system (i.e., evaporator and condenser). Current efforts are now focused on demonstrating an inverter-scale passive two-phase system for automotive power modules (Delphi's discrete power switches).

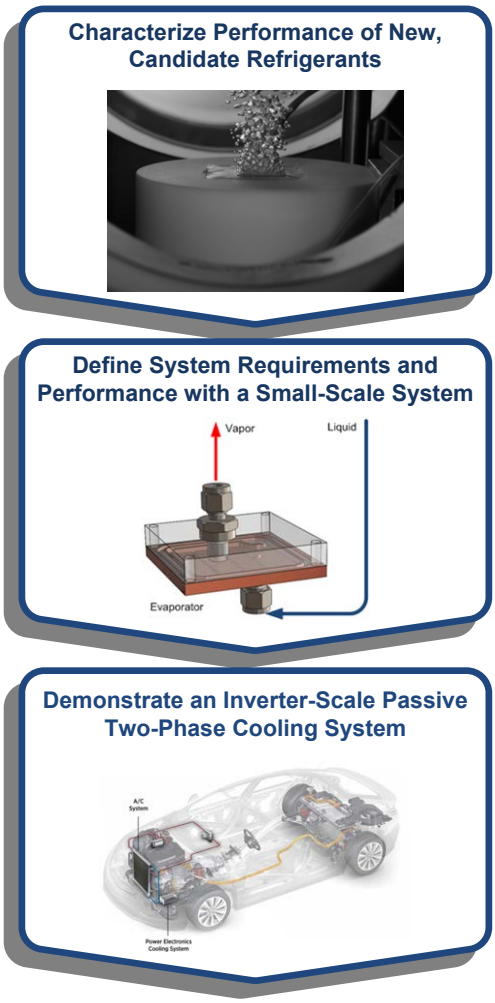

Figure 1: Flow chart depicting the project approach.

Results

Comparing the Performance of Candidate Refrigerants

Two refrigerants are being evaluated for use in the two-phase–based cooling systems developed in this project: hydrofluoroolefin (HFO)-1234yf and HFC-245fa. HFO-1234yf's nearly identical thermophysical properties to HFC-134a [6] and low global warming potential (GWP = 4) [7, 8] make it the leading candidate as the next generation refrigerant in automotive air-conditioning systems. The use of automotive air-conditioning refrigerants for two-phase cooling of automotive power electronics is an attractive option because these refrigerants are already qualified for automotive use [9], and because it may allow for potential consolidation of cooling systems as proposed by Campbell et al. [10]. In the first year of this project, the boiling heat transfer performance of HFO-1234yf was characterized on both plain and microporous-enhanced surfaces. The results from these tests have been published in Ref. [11]. More recently, we characterized the pool boiling performance of HFC-245fa [12]. HFC-245fa's higher critical temperature, non-flammable nature, and lower operating pressure make it a good candidate for two-phase cooling of electronics. The higher critical temperature ($T_{critical}$ = 154°C) allows for higher operating temperatures, which has implications for reducing the system condenser size.

In Figure 2, the boiling heat transfer coefficients for HFO-1234yf, HFC-245fa, and HFC-134a are plotted versus the saturation temperature. The temperature range evaluated pertains to potential operating temperatures for a two-phase–based cooling system for automotive power electronics. The performance of HFC-134a is provided as a comparison because this refrigerant is currently utilized in automotive cabin cooling systems. The performance for the refrigerants on plain surfaces (sandpaper polished with a surface roughness Ra = 0.3 µm) and microporous-coated surfaces are shown in Figures 2a and 2b, respectively. The microporous coating used in these experiments was developed by 3M [13]. The coating, shown in Figure 3, is composed of copper micrometer-sized particles bonded to the surface to form an approximately 150-µm-thick microporous coating with an estimated 40%–50% porosity.

In boiling heat transfer, heat transfer coefficients are dependent on the imposed heat flux. In this case, the heat transfer values provided in Figure 2 are taken at a heat flux of 20 W/cm^2. For the plain surface case, HFC-245fa was found to provide heat transfer values that were approximately 44% and 49% lower than the heat transfer coefficients of HFO-1234yf and HFC-134a, respectively. At the same saturated temperature, HFC-245fa operates at a lower reduced pressure P_r (P_r = vapor pressure / critical pressure) as compared with the other two refrigerants resulting in its lower performance. The reduced pressure is well known to play a critical role in boiling heat transfer, with boiling heat transfer coefficients increasing with increasing reduced pressure [14, 15].

As shown in Figure 2b, the use of the 3M microporous coating greatly enhanced heat transfer coefficients for all three refrigerants. Less variation in heat transfer rates between the various refrigerants was observed for the microporous-coated surfaces. With the coatings, all refrigerants produced high transfer coefficients that can exceed 100,000 W/m^2-K. These high heat transfer values enable higher device power densities that may translate to more compact and efficient cooling systems. Increased evaporation within the coating's porous structure, combined with increased nucleation site density, increased wetted area, and capillary wicking within the coating, are believed to be the mechanisms responsible for the microporous-coating heat transfer enhancements.

This report is available at no cost from the National Renewable Energy Laboratory (NREL) at www.nrel.gov/publications.

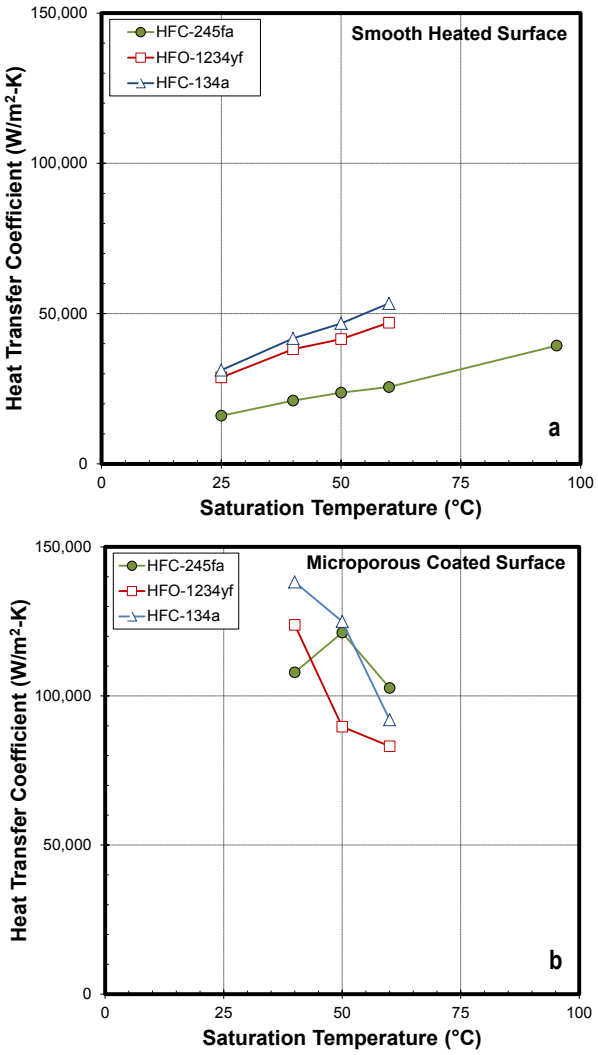

Figure 2: Heat transfer coefficient values plotted versus the saturation temperature for a sandpaper-polished (a) and microporous coated (b) surfaces. The coefficient values are taken at a heat flux of 20 W/cm^2.

Passive Two-Phase Cooling System

Research has also been conducted to design a complete (evaporator and condenser) passive two-phase cooling system for automotive power electronics. An initial proof-of-concept passive two-phase cooling system has been designed and fabricated. The cooling system was designed to cool six Delphi discrete power modules and has a maximum operating pressure of 1.03 MPa. Structural finite element analysis was used to design the system components for the elevated pressure requirements. Once fabricated, the system was hydrostatically pressure-tested to verify the system's pressure rating. The system's pressure rating allowed it to be charged with refrigerants HFO-1234yf or HFC-245fa.

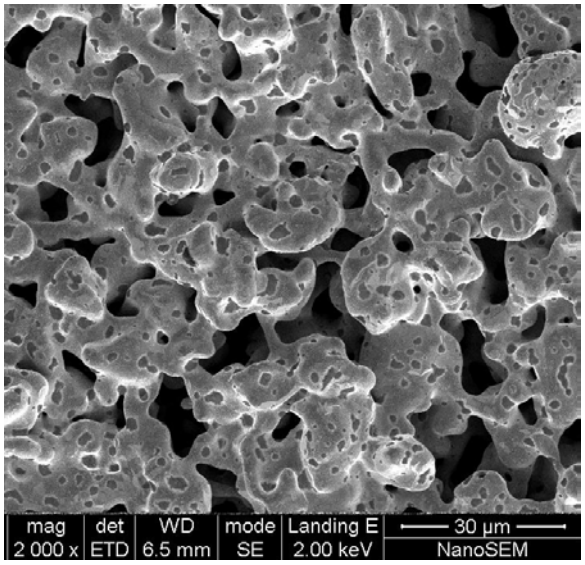

Figure 3: Scanning microscope image of the 3M boiling enhancement, microporous coating.

The main objective of these tests was to determine if the evaporator could dissipate 3.5 kW of heat with only 250 mL of refrigerant without reaching dry-out. Dry-out occurs at elevated heat fluxes when vapor restricts liquid access to the cooled surface, causing temperatures to significantly increase. The 3.5-kW target is based on the estimated maximum steady-state heat dissipation requirements of automotive power electronics components rated for 55 kW peak power requirements. Prior tests with a smaller-scale cooling system were used to size the volume of the evaporator. Based on those results, it is estimated that it requires ≤ 250 mL of refrigerant to dissipate about 3.5 kW of heat using a passive two-phase cooling configuration.

Equipment and Procedures

The condenser for this proof-of-concept system consisted of ten finned tubes that were connected together at the top and bottom. The total air- and condensate-side surface areas for the condenser were 1 m^2 and 0.05 m^2, respectively. The finned structures on the exterior of the tubes allowed for a larger surface area on the air-side. Calibrated K-type thermocouples were used to measure the inlet-air, liquid, vapor, and heater temperatures. System vapor pressure was measured using an absolute pressure transducer. A schematic of the cooling system is shown in Figure 4.

This report is available at no cost from the National Renewable Energy Laboratory (NREL) at www.nrel.gov/publications.

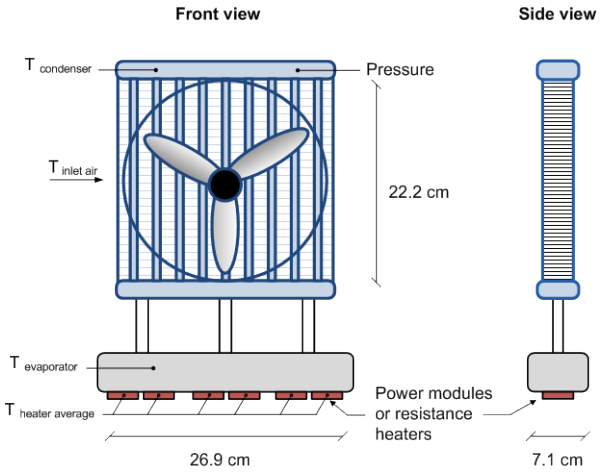

Figure 4: Schematic of the two-phase cooling system.

Existing thermal transient power supplies do not have the capacity to heat the Delphi power modules above about 150 W. Therefore, the initial experiments were conducted using six ceramic resistance heaters in place of the six Delphi power modules. The dimensions of the ceramic heaters (25 mm × 15 mm × 2.5 mm) were similar to those of the Delphi modules. Each heater can generate about 580 W of heat (total power for six heaters: 3.5 kW). The ceramic heaters were externally attached to the evaporator using thermally conductive grease as the thermal interface material. The temperatures of the heaters were measured via thermocouples embedded within the ceramic heaters.

Once the heaters were attached to the evaporator, the air in the system was evacuated using a vacuum pump. Pressure within the system was allowed to decrease to about 10 Pa to indicate that most of the air was removed from the system. The system was then charged with refrigerant via a transfer tube connected above the cooling system. A valve between the transfer tube and the system was opened, allowing the 330 grams (250 mL of liquid) of HFC-245fa to enter the system. Once the refrigerant was transferred, the valve between the transfer tube and the system was closed, and the transfer tube was disconnected from the system. Measurements of the vapor temperature and pressure confirmed saturated conditions verifying that no air was present within the system.

Experimental Results and Discussion

The unit (area-weighted) thermal resistance of the cooling system is plotted versus the heat dissipated in Figure 5. These results are for an evaporator without any boiling enhancement coating. Because ceramic heaters attached via thermal interface material were used as a substitute for actual power modules attached via bonded interface materials (e.g., thermoplastics, solder), the thermal resistance values are not necessarily indicative of the thermal performance of the cooling system. However, the main objective of these initial tests was to measure the maximum heat dissipation of the system (i.e., dry-out heat flux).

The heater-to-evaporator resistance is defined per Equation 1:

$$R''_{th,\ evaporator} = \frac{(\overline{T_{htr}} - T_l)}{Total\ power} \times\ Heater\ area \quad (1)$$

The condenser-to-air resistance is defined per Equation 2:

$$R''_{th,\ condenser} = \frac{(T_v - T_a)}{Total\ power} \times\ Heater\ area \quad (2)$$

$\overline{T_{htr}}$ is the average temperature of the six heaters. T_l, T_v, and T_a are the liquid, vapor, and inlet-air temperatures. The *total power* is the total heat dissipated by the system, and *heater area* is the total surface area of the six heaters.

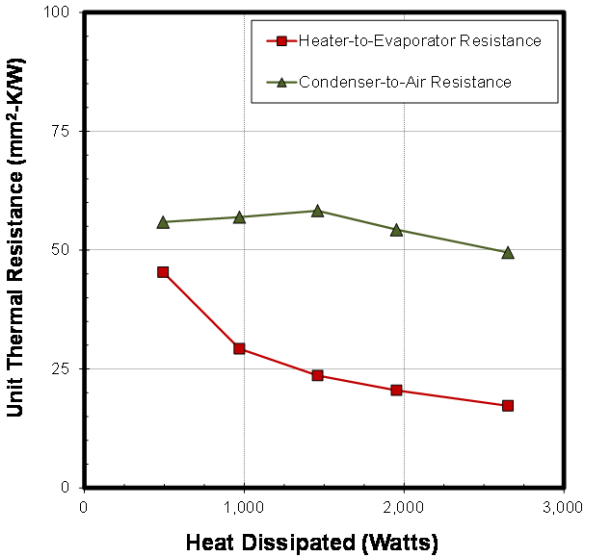

Figure 5: Area-weighted thermal resistance versus the heat dissipated.

As shown in Figure 5, the heater-to-evaporator resistance decreases with increasing heat dissipation. This effect is associated with an increased contribution from two-phase heat transfer (i.e., boiling/evaporation) at higher power levels, which improves thermal performance. The system's temperature and pressure increased with increasing heat dissipation. Boiling heat transfer rates will increase with increasing pressure; thus, this effect also contributes to the observed heater-to-evaporator decreasing resistance trend. The thermal resistance of the condenser is less affected by the increasing heat dissipation (i.e., increasing system temperature and pressure).

The maximum heat dissipated by the passive two-phase cooling system was approximately 2.7 kW. This limit on the total heat dissipated was not a thermal limitation, but instead a pressure limitation of the system. Increasing the amount of heat imposed into the system increased the system's temperature and pressure. At the maximum heat dissipated (2.7 kW), the vapor pressure reached the maximum operating pressure of the system, causing the system to shut down, and prevented testing to higher power levels.

This report is available at no cost from the National Renewable Energy Laboratory (NREL) at www.nrel.gov/publications.

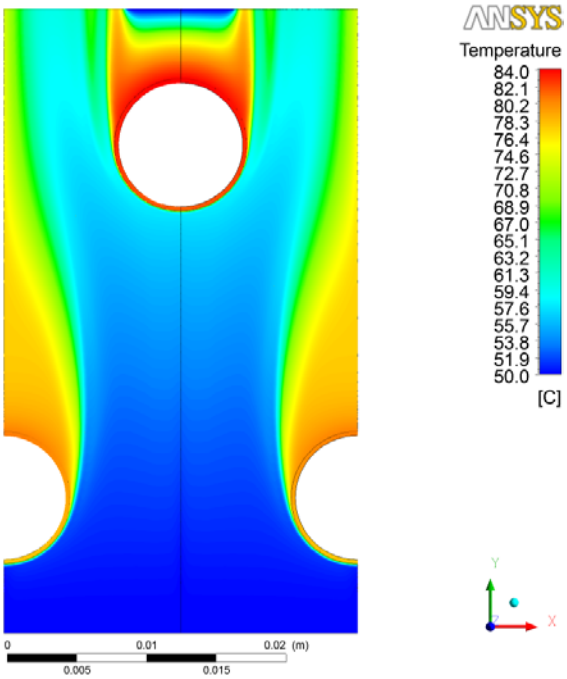

Figure 6: Computational fluid dynamics air temperature contours.

Increasing the condensing capacity of the system will decrease the condenser resistance and allow for operation at lower temperatures and pressures. A new condenser has been designed and is currently being fabricated by a heat exchanger coil manufacturer. The new condenser will be fabricated using common fabrication techniques (i.e., inexpensive) and will have higher fin densities (i.e., increased air-side surface area) as compared to the existing condenser. It has been designed to dissipate 3.5 kW at a maximum inlet-air temperature of 50°C while maintaining device junction temperatures just below 150°C. Computational fluid dynamic simulations were performed to size the condenser (Figure 6). Compared to the existing condenser, the new condenser's overall dimensions/footprint will be slightly smaller, but its air-side and condensation-side surface areas will be increased by 180% and 130%, respectively. Two new condensers will be fabricated, one with condensation-enhanced surfaces and one with plain/smooth surfaces. Comparing the performance of the two condensers will allow us to evaluate the effect of condensation enhancement techniques on a passive two-phase cooling system. Condensation-side enhancements have the potential to improve performance and reduce the size and weight of the condenser.

Techniques to improve the evaporator performance and reduce its size have been identified, and a Record of Invention has been submitted. The techniques incorporate features to reduce the evaporator resistance while utilizing low-cost fabrication techniques and materials (e.g., aluminum). A computer-aided-design model of the Delphi power modules mounted on the improved evaporator design was generated and incorporated all the thermal resistance interfaces (i.e., solder layer and bonded interfaces). The model was then imported into ANSYS Workbench for thermal analysis. Finite element simulations combined with experimentally measured heat transfer coefficient values taken from the fundamental research were used to evaluate the performance of this advanced evaporator design.

The unit/area-weighted thermal resistance results (junction-to-liquid) as predicted by finite element analysis are provided in Table 1. The Delphi module insulated gate bipolar transistor's area and temperature (i.e., junction temperature) were used to calculate the thermal resistance values. Two evaporator designs were analyzed: aluminum based and copper based. For comparison, the thermal resistance values (junction-to-liquid) of state-of-the-art automotive power modules are also shown in Table 1. The thermal resistance values of the aluminum (i.e., 23 mm^2-K/W) and copper (i.e., 17 mm^2-K/W) evaporators are about 33% and 48% lower, respectively, than that of the dual-side cooled 2008 Lexus power module. These reductions in the thermal resistance have the potential to increase power densities by 44%–80%. Moreover, the passive cooling approach also has implications for increasing the system efficiency.

Table 1: Unit thermal resistance (junction-to-liquid) values for the advanced evaporator design per finite element simulations. Automotive power module thermal resistance values are provided for reference.

	Nissan Leaf [1]	Toyota Prius (2010) [1]	Lexus Hybrid (2008) [2]	**Passive Two-Phase Advanced Design**
Unit Thermal Resistance R''_{th} (mm^2-K/W)	52	47	33	**17-23**
	Single-side cooled		Dual-side cooled	

[1] Liang [16]

[2] Sakai et al. [17]

Enhanced Surface Reliability Studies

An experimental system has been fabricated and procedures have been established to experimentally evaluate the long-term reliability of boiling enhancement coatings. The objective for these experiments is to evaluate for coating delamination and its effect on thermal performance. The coating evaluated for these tests is the 3M microporous coating shown in Figure 3.

For these experiments, three coated samples are housed within a pressure vessel charged with refrigerant HFC-245fa. An image of the samples submerged in refrigerant within the vessel is provided in Figure 7. A schematic of a sample is provided in Figure 8. As shown, a cartridge heater is inserted into each copper sample to provide the heating capacity. Two calibrated (36 average wire gauge) K-type thermocouples are embedded within the 10-mm-diameter length of the samples to allow for calculation of the total heat and surface temperature, assuming one dimensional and steady-state heat transfer. The total heat and the surface temperature combined with the refrigerant liquid

This report is available at no cost from the National Renewable Energy Laboratory (NREL) at www.nrel.gov/publications.

temperature are then used to calculate an average two-phase heat transfer coefficient for the coated surface.

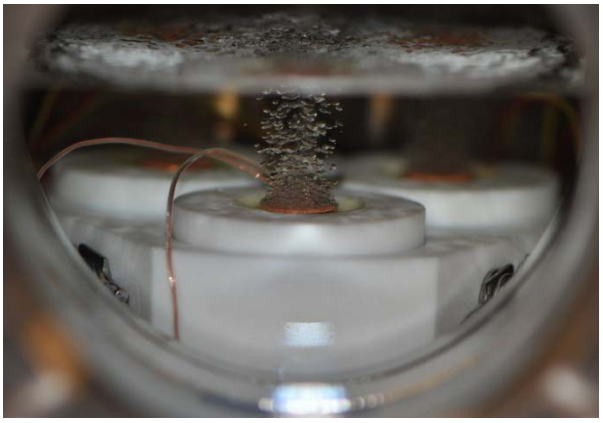

Figure 7: Picture of boiling occurring on one of the coated samples.

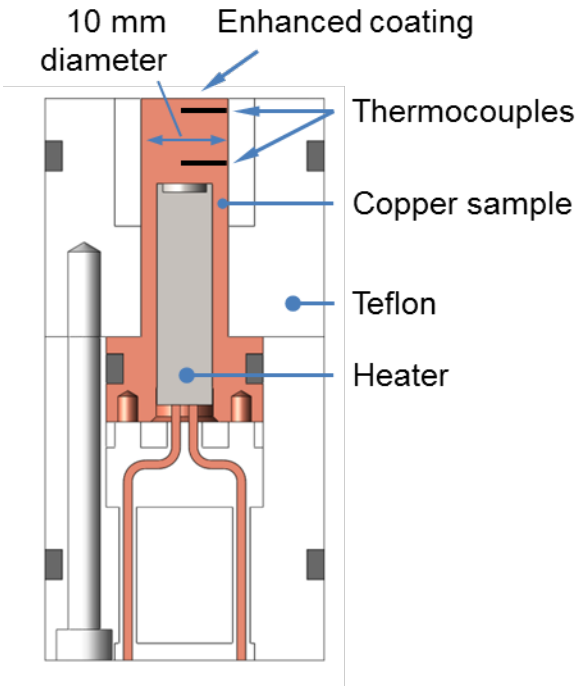

Figure 8: Schematic of the enhanced surface sample.

The testing procedures involve heating one sample at a time for a total of five minutes. Approximately 15 W/cm^2 are dissipated from the coated surface—enough heat to generate full nucleate boiling. Due to the small size of the samples, steady-state temperatures are typically achieved within a minute, but heat is maintained for a total of five minutes. The entire testing process is automated and operates unattended. The process is controlled via a LabVIEW program and dedicated computer, data acquisition system, and power supply.

To date, the samples have been subjected to approximately 8,000 on/off heating cycles. Thus far, results indicate some degradation in performance; however, the degradation is believed to be associated with contaminants collecting on the porous sample surface and not coating delamination. Evidence of some fouling on the surfaces was visually observed when samples were removed from the vessel. The source of the contaminants could be either from residual solder flux on the various thermocouple connections or contaminants within the sample that were not removed in the initial cleaning process. As stated before, the objective for these experiments is to evaluate for coating delamination. The samples and system are currently being cleaned. Once this process is complete, the reliability experiments will be restarted.

A parameter monitored during these tests is boiling incipient behavior. In boiling heat transfer, some amount of superheat (i.e., temperature of the heated surface minus the saturated/boiling temperature of the fluid) is required to initiate boiling on a heated surface. Ideally, the superheat required to initiate boiling should be low to prevent wide temperature cycling of the sample (e.g., electronic device being cooled). Microporous-coated surfaces are effective at reducing the superheat required to initiate boiling; however, their ability to maintain this performance under long-term use conditions is unknown. Although the temperature sampling rate used for these tests (measurement every ½ second) cannot measure every temperature (i.e., cannot sample at a continuous rate) during the heating process, based on the data collected we can conclude the following. The results suggest that for all three samples the superheat essentially remained unchanged for the entire 8,000 cycles. Moreover, the maximum temperature overshoot (sample's maximum temperature just prior to boiling incipience minus the sample's steady-state temperature) was observed for sample one and was approximately 3.5°C. In other cases (samples two and three), there was negligible temperature overshoot.

Conclusions and Future Directions

Future Directions

Work is currently underway to fabricate the advanced two-phase power electronics cooling system that consists of the new condenser and improved evaporator. Tests are planned to thoroughly characterize the thermal performance of the advanced design. The next steps for this project are summarized below.

1. Characterize the performance of the cooling system using refrigerants HFC-245fa and HFO-1234yf.
2. Understand the effect of inclination on performance by varying the inclination of the cooling system and measuring its thermal performance. These tests will evaluate the effect of vehicle inclination (e.g., climbing a hill) on the cooling system's performance.
3. Quantify the system's performance metrics (thermal performance, coefficient of performance, volume, weight) and compare with the performance metrics of a typical water/ethylene-glycol–cooled automotive system.

This report is available at no cost from the National Renewable Energy Laboratory (NREL) at www.nrel.gov/publications.

Conclusions

Research has been conducted to design, fabricate, and characterize the performance of a passive two-phase system. The major conclusions for this study are summarized below.

1. A proof-of-concept indirect, passive, two-phase cooling system (evaporator and air-cooled condenser) was fabricated. Experiments demonstrated that the system can dissipate at least 2.7 kW of heat with only 250 mL (330 grams) of HFC-245fa.
2. An advanced two-phase cooling system has been designed and is currently being fabricated. The new system consists of a custom-fabricated condenser and an improved evaporator. The evaporator incorporates features to reduce its thermal resistance and size while utilizing low-cost fabrication techniques and materials (e.g., aluminum). A Record of Invention detailing these enhancement techniques has been submitted. The new system is designed to dissipate 3.5 kW of heat at a maximum air-inlet temperature of 50°C while maintaining junction temperatures below 150°C. Finite element analysis of this advanced design indicates that the system can reduce the thermal resistance by as much as 48% as compared with the state-of-the-art automotive systems. The thermal resistance reductions have the potential to increase power density by as much as 80%.
3. Experiments to evaluate the reliability of boiling enhancement coatings have been initiated. To date, samples have been exposed to about 8,000 on/off cycles. Results indicate no delamination of the coated surfaces and no change to the boiling incipient superheat behavior.

Nomenclature

P	pressure
R''_{th}	area-weighed/unit thermal resistance, mm^2-K/W
T	temperature, °C
Subscripts	
a	air
htr	heater
l	liquid
r	reduced (e.g., reduced pressure)
v	vapor

FY 2013 Publications/Presentations

1. Moreno, G., Narumanchi, S., and King, C., 2013, "Pool Boiling Heat Transfer Characteristics of HFO-1234yf on Plain and Microporous-Enhanced Surfaces," *ASME Journal of Heat Transfer*, 135(11), pp. 111014.
2. Thiagarajan, S.J., Narumanchi, S., and Yang. R., 2013, "Effects of Flow Rate and Subcooling on Spray Heat Transfer on Microporous Copper Surfaces," *International Journal of Heat and Mass Transfer (in press),*
3. Moreno, G., Jeffers, J. R., and Narumanchi, S., "Effects of Pressure and a Microporous Coating on HFC-245fa Pool Boiling Heat Transfer, " *ASME Summer Heat Transfer Conference,* Minneapolis, MN, USA, July 2013, pp. 557-587.
4. Moreno, G., Jeffers, J., Narumanchi, S., and King, C., "Passive Two-Phase Cooling of Automotive Power Electronics using Refrigerant HFO-1234yf," *Proc. SAE Thermal Management Systems Symposium*, Scottsdale, AZ, USA, October 2012.

Acknowledgements

The author would like to acknowledge the support provided by Susan Rogers and Steven Boyd, Technology Development Managers for Advanced Power Electronics and Electric Motors, Vehicle Technologies Program, U.S. Department of Energy Office of Energy Efficiency and Renewable Energy. The significant contributions of Jana Jeffers and Charlie King (NREL) to the project are acknowledged. The author also thanks Phil Tuma (3M) for providing samples of the microporous copper coatings.

References

[1] Mudawar, I., 2001, "Assessment of High-Heat-flux Thermal Management Schemes," Components and Packaging Technologies, IEEE Transactions on, 24(2), pp. 122-141.

[2] Brown, G. M., Elbacher, B. J., and Koellner, W. G., "Increased Productivity with AC Drives for Mining Excavators and Haul Trucks," Proceedings EEE Industry Applications Conference, October 2000, pp. 28-37.

[3] Koellner, W. G., Brown, G. M., Rodriguez, J., Pontt, J., Cortes, P., and Miranda, H., 2004, "Recent Advances in Mining Haul Trucks," IEEE Transactions on Industrial Electronics, 51(2), pp. 321-329.

[4] Tantolin, C., Lallemand, M., and Eckes, U., "Experimental Study of Immersion Cooling for Power Components," Proceedings IEE International Conference on Control, CONTROL'94, March 1994, pp. 723-727.

[5] Tuma, P. E., "Design Considerations Relating to Non-Thermal Aspects of Passive 2-Phase Immersion Cooling," Proceedings Semiconductor Thermal Measurement and Management Symposium (SEMI-THERM), 2011 27th Annual IEEE, March 2011, pp. 1-9.

[6] Leck, T. J., "Evaluation of HFO-1234yf as a Potential Replacement for R-134a in Refrigeration Applications," Proceedings 3rd IIR Conference on Thermophysical Properties and Transfer Processes of Refrigerants, June 2009.

[7] Minor, B. H., and Spatz, M. A., "Evaluation of HFO-1234yf for Mobile Air Conditioning," Proceedings 2008 SAE World Congress, April 2008.

[8] Park, K.-J., and Jung, D., 2010, "Nucleate Boiling Heat Transfer Coefficients of R1234yf on Plain and Low Fin

This report is available at no cost from the National Renewable Energy Laboratory (NREL) at www.nrel.gov/publications.

Surfaces," International Journal of Refrigeration, 33(3), pp. 553-557.

[9] U.S. Environmental Protection Agency, 2012, "Protection of Stratospheric Ozone: Amendment to the HFO-1234yf SNAP Rule for Motor Vehicle Air Conditioning Sector," Federal Register

[10] Campbell, J. B., Tolbert, L. M., Ayers, C. W., Ozpineci, B., and Lowe, K. T., 2007, "Two-Phase Cooling Method Using the R134a Refrigerant to Cool Power Electronic Devices," IEEE Transactions on Industry Applications, 43(3), pp. 648-656.

[11] Moreno, G., Narumanchi, S., and King, C., 2013, "Pool Boiling Heat Transfer Characteristics of HFO-1234yf on Plain and Microporous-Enhanced Surfaces," ASME Journal of Heat Transfer, 135(11), p. 111014.

[12] Moreno, G., Jeffers, J. R., and Narumanchi, S., 2013, "Effects of Pressure and a Microporous Coating on HFC-245fa Pool Boiling Heat Transfer " ASME Summer Heat Transfer Conference Minneapolis, MN, USA, pp. 557-587.

[13] 3M, 2009, "3M™ Microporous Metallic Boiling Enhancement Coating (BEC) L-20227," 3M.

[14] Nishikawa, K., Fujita, Y., Ohta, H., and Hidaka, S., 1982, "Effects of System Pressure and Surface Roughness on Nucleate Boiling Heat Transfer," Memoirs of the Faculty of Engineering, Kyushu University, 42(2), pp. 95-111.

[15] Webb, R. L., and Pais, C., 1992, "Nucleate Pool Boiling Data for Five Refrigerants on Plain, Integral-Fin and Enhanced Tube Geometries," International Journal of Heat and Mass Transfer, 35(8), pp. 1893-1904.

[16] Liang, Z., "Power Device Packaging," Oak Ridge National Laboratory, Electrical and Electronics Technical Team Presentation, March 2012.

[17] Sakai, Y., Ishiyama, H., and Kikuchi, T., "Power Control Unit for High Power Hybrid System," SAE International, April 2007, pp. 25–29.

This report is available at no cost from the National Renewable Energy Laboratory (NREL) at www.nrel.gov/publications.

Air-Cooling Technology for Power Electronics Thermal Management

Principal Investigator: Scot Waye
National Renewable Energy Laboratory (NREL)
Transportation and Hydrogen Systems Center
15013 Denver West Parkway
Golden, CO 80401
Phone: 303-275-4454
E-mail: Scot.Waye@nrel.gov

DOE Technology Development Manager: Susan A. Rogers
Phone: 202-586-8997
E-mail: Susan.Rogers@ee.doe.gov

NREL Task Leader: Sreekant Narumanchi
Phone: 303-275-4062

Start Date: FY11
Projected End Date: FY15

Objectives

The overall project objective is to develop and apply air-cooling technology to improve power electronics thermal management design and influence industry, enhancing system performance to help meet the U.S. Department of Energy (DOE) Advanced Power Electronics and Electric Motors (APEEM) Program power electronics technical targets for weight, volume, cost, and reliability. This overall objective includes the following:

- Develop and demonstrate commercially viable, low-cost air-cooling solutions for a range of vehicle applications and assess their potential for reducing the cost and complexity of the power electronics cooling system.
- Enable heat rejection directly to ambient air, simplifying the system by eliminating liquid coolant loops, thereby improving weight, volume, cost, and reliability.
- Collaborate with Oak Ridge National Laboratory (ORNL) to demonstrate the feasibility of using a high-temperature air-cooled inverter to achieve DOE technical targets.
- FY 13 objectives included:
  - Determine the feasibility of high-temperature air-cooled inverter
  - Build a system-level test bench and begin investigation of balance-of-system components
  - Begin thermal design optimization to ensure that effective designs are being used to determine the bounds of air-cooled inverter design space.

Technical Barriers

The use of air as a coolant has several benefits, drawbacks, and challenges. Air is free, it does not need to be carried, it is benign (no safety or environmental concerns), and it is a dielectric. As a heat transfer fluid, however, it has a number of drawbacks. Air has a low specific heat, low density, and low conductivity. These make it a poor heat transfer fluid and cause a number of design challenges. To reject the high power densities required by electric drive power electronics using the heat transfer coefficients achievable with air, large increases in wetted area are needed. When increasing area, spreading resistance, fin efficiency, weight, volume, and cost need to be considered. Due to the low specific heat, larger mass flows of air are required to remove the heat. This can lead to parasitic power issues, especially coupled to the pressure loss of extended surfaces. This requires careful consideration of the system coefficient of performance. Depending on the location of the inverter, environmental loads and ducting to better air sources may need to be considered. Location can also affect the need for noise suppression for the prime mover (blower/fan). For example, the Honda system incorporated a silencer [1] because the inverter was located in the passenger compartment. In order to push heat transfer performance higher, small-channel heat exchangers can be used, but filtering must be addressed. If needed, filtering can add pressure drops and maintenance issues may need to be addressed.

Technical Targets

The DOE technical targets applicable to this research are the 2015 and 2020 APEEM Program targets for power electronics with 30-kW continuous and 55-kW peak power.

Accomplishments

- Revised heat generation analysis for updated device data from ORNL using conservative assumptions to yield 25 W per device heat load for a nine-module inverter approach and 45 W per device heat load for a six-module inverter approach.
- Through modeling, showed the heat transfer feasibility of a high-temperature, air-cooled inverter. Predicted 3.2 kW of heat rejection, surpassing the conservative target of 2.7 kW, using 0.054 m^3/s (115 CFM) of air. This predicted flow rate and pressure drop could be provided by a 50-W fan. This flow rate is less than that used by a typical automotive climate control system.
- Using computational fluid dynamics (CFD), developed optimization driver combined with assumptions about remaining inverter components, conducted parametric study over design space to identify candidate heat exchanger designs that meet future DOE technical targets for weight and volume while limiting parasitic losses. Found designs exceeding 2015 targets with fan parasitic power similar to automotive climate control system condensers or fans.
- Combined module-level optimization with balance-of-system components (ducting) to optimize heat exchanger design for system-level performance, which incorporated assumptions from experimentally obtained ducting pressure losses.
- Built test apparatus for sub-module testing for model validation.

This report is available at no cost from the National Renewable Energy Laboratory (NREL) at www.nrel.gov/publications.

✧ ✧ ✧ ✧ ✧

Introduction

All commercially available electric-drive vehicles, with the notable exception of the low-power Honda system, use liquid-cooled power electronic systems. All the heat from a vehicle, however, must ultimately be rejected to the air. For liquid-cooled systems, heat from the power electronics is transferred to a water-ethylene glycol coolant via a heat exchanger and then pumped to a separate, remote liquid-to-air radiator where the heat is rejected to the air. Air cooling has the potential to eliminate the intermediate liquid-cooling loop and transfer heat directly to the air.

Eliminating the intermediate liquid-cooling loop using direct air cooling of the power converter can reduce system complexity and cost by removing or reducing the pump, coolant lines, remote heat exchanger, remote heat exchanger fan, and coolant. In order to realize these gains, however, effective system-level design of the direct air-cooled system heat exchanger, fan, and ducting is needed. Decoupling the inverter/converter from the liquid cooling system also has the potential to provide increased flexibility in location. Honda took advantage of this benefit by placing its 12.4-kW power electronics system behind the rear seat of the vehicle cabin and integrating closely with the battery thermal management system [1].

As power electronic semiconductor and electronic packaging technology advances, higher allowable junction temperatures will further expand the feasible designs and benefits of direct air-cooled power electronics. Currently, silicon insulated gate bipolar transistors (IGBTs) have a maximum allowable junction temperature between 125°C and 150°C [2,3] that may be extended to 175 °C in the future [3], while advanced semiconductor technologies such as silicon carbide (SiC) and gallium nitride (GaN) allow operation above 200°C [4–6] and may also improve the inverter efficiency at lower temperatures [5].

The Honda system is a mass-produced, commercially available solution. It is low power, however, with a peak power delivery of 12.4 kW [1]. The electric Mini-E uses an air-cooled AC Propulsion drive system. This has a 50-kW continuous, 150-kW peak power, but does not meet DOE technical targets and is low production volume [7]. Additional research adds to commercial solutions. Toshiba Corporation is researching and developing a new power module design for forced-air cooling systems for a power converter [8]. ETH Zurich University has published a number of studies on this topic recently and is actively researching high-temperature, air-cooled power electronics for automotive and other applications. One of these papers found that, combined with a Peltier element, a high-temperature SiC automotive inverter could operate at a 120°C ambient [9]. Another reports the possibility of using extremely high-temperature SiC devices (234°C and higher) to create an air-cooled electric-drive vehicle inverter with a power density of 51 kW/L and operating at 120°C ambient [10]. For aggressive, high-flux cooling of electric-drive vehicle inverters, Aqwest is investigating circulating liquid metal flow loops to enable forced air cooling [11].

Approach

- Use a system-level approach that addresses the cooling technology, package mechanical design, balance-of-system, and vehicle application requirements.
- Research each of these areas in depth and apply findings to develop effective system-level designs.
- Develop experimental and analytical/numerical tools and processes that facilitate high-quality and rapid research results.
- Investigate the effect high-temperature power semiconductor devices have on air-cooled inverter design.
- Work closely with industry, university, and national laboratory partners to ensure relevant and viable solutions.

The objective of NREL's Air-Cooling Technology for Power Electronics Thermal Management project is to assess, develop, and apply air-cooling technology to improve power electronics thermal control design and influence industry's products, thereby enhancing system performance to meet DOE technical targets for weight, volume, cost, and reliability. This research effort seeks to develop the necessary heat transfer technology and system-level understanding to eliminate the intermediate liquid-cooling loop and transfer heat directly to the air. The relative merits of air-cooled, high-heat-flux automotive power electronic thermal management systems and the influence of high-temperature, wide bandgap semiconductors on this design space will be quantified, evaluated, and demonstrated under steady state and transient conditions.

Effectively and viably accomplishing these goals requires an air-cooled system thermal design understanding and approach. As shown in Figure 1, this project will use modeling and experimentation to address each aspect of the system: heat transfer cooling technology, power electronics package thermal design, balance-of-system (prime movers, ducting, etc.), and their interconnected interactions. It is also critical to account for and understand the effects of constraints and inputs into the air-cooled thermal management system: thermal environment, device type, and vehicle context. The thermal environment constraints have a direct impact on the driving temperature difference available for air-cooled heat transfer and can vary depending on design targets and system location in a vehicle. Under-hood temperatures are approximately 100°C–140°C and are therefore unsuitable for cooling. External ambient air at 30°C–45°C is highly suitable for cooling, and some additional benefit can be gained from using cabin air, but it must be balanced with the added parasitic load on the air conditioning system. The device type will determine both the maximum junction temperature and efficiency and thus influences the maximum allowable package surface temperature and heat load. Advanced power semiconductors, such as silicon carbide and gallium nitride, have the potential to greatly expand the air-cooling feasibility range by increasing the allowable junction temperature from

This report is available at no cost from the National Renewable Energy Laboratory (NREL) at www.nrel.gov/publications.

125°C to 200°C or higher while possibly improving efficiency. Vehicle context determines the power electronics duty cycle, affecting the total heat rejection needs and also imposing constraints on the system volume and weight. Understanding the in-vehicle demands on the power electronics systems will allow for modulated designs to meet cooling needs, reducing system overdesign and minimizing parasitic losses.

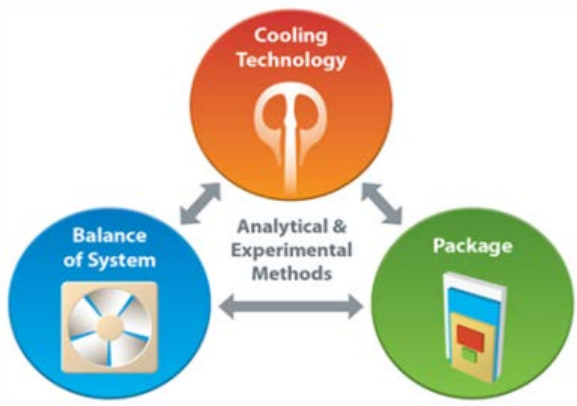

Figure 1: Power electronics air-cooled thermal management system research and design approach

To move ideas from concept to implementation, four levels of research, development, and demonstration will be used: novel cooling technology fundamental heat transfer, system-level heat transfer and balance-of-system, module-level application and demonstration, and inverter-level demonstration (Figure 2). This process will both ensure that each level of complexity assists in achieving the overall objectives and serve to screen ideas so that only the best approaches pass to the next level.

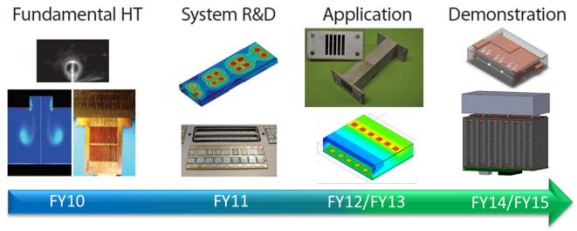

Figure 2: Air-cooling system research, development, and demonstration approach

Project Timeline

In FY11, NREL completed a proof-of-principle analysis using a system-level approach [12]. In this analysis, as expected, the baseline liquid-cooled system significantly outperformed the air-cooled system. The relative performance of the air-cooled system improved with increasing allowable junction temperature and/or use of the improved concept spreader. At an allowable junction temperature of 200°C or 150°C plus the use of the advanced spreader, the air-cooled system was able to match the power density of the liquid-cooled approach. The air-cooled system using advanced technology could meet or exceed the power per total insulated-gate bipolar transistor (IGBT) area of the liquid-cooled system. This analysis indicated that a high-temperature air-cooled system held significant promise and should be pursued in more depth.

Based on these results, NREL established a high-temperature air-cooled inverter collaboration with ORNL. The goal of this project is to demonstrate the feasibility of meeting DOE's 2015 technical targets by using a high-temperature air-cooled inverter. ORNL is leading the advanced wide-bandgap-device evaluation and selection and electrical topology design. NREL is leading the thermal management design and evaluation at both the module- and system-level. The thermal system design approach for this collaboration is shown in Figure 3. This is an iterative process between NREL and ORNL that involves other industry partners at various stages.

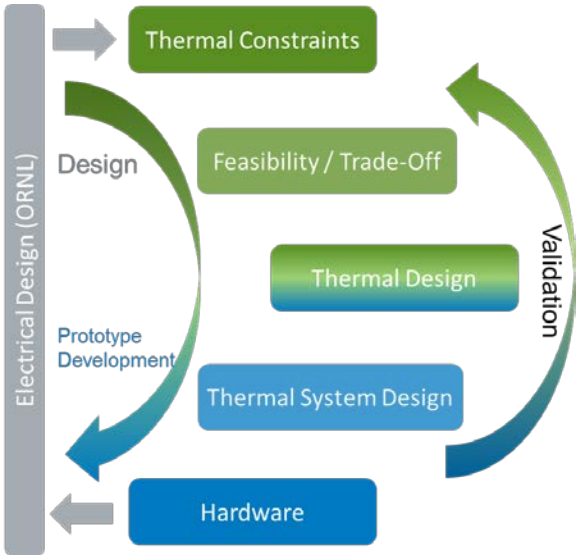

Figure 3: High-temperature, air-cooled inverter thermal design approach

In FY12, electrical design information was passed from ORNL to NREL, which then converted the information into thermal design targets. Based on this information, a feasibility/trade-off study was conducted using CFD modeling and experimental validation. After determining the feasibility, NREL applied modeling and experimental tools to begin a detailed thermal design to ensure an optimized prototype.

In FY13, the optimization continued and a sub-module section of the baseline design was fabricated to validate the models. Further optimization and exploration of the design space yielded viable solutions to meet targets without incurring excessive parasitic power.

In FY14, an optimized design will be chosen, prototyped, and tested. This will be combined with the module electronics from ORNL and tested as an operational unit. The thermal and electrical performance will be tested in parallel, and lessons learned will be applied to further improve the design. A feasible ducting solution will be analyzed for flow characterization and pressure losses to size an appropriate fan for the system. The full system thermal feasibility will also be determined.

In FY15, the goal is to build and demonstrate an operational high-temperature, air-cooled inverter.

Experimental Methods

The Air Cooling Technology Characterization Platform, shown in Figure 4, was updated in FY12. Compressed air is

This report is available at no cost from the National Renewable Energy Laboratory (NREL) at www.nrel.gov/publications.

supplied to a desiccant dryer to remove moisture. The air is dried to a dew point of -20°C or lower. It is passed through a 5-µm particulate filter and regulated to a constant pressure of 68 to 137 kPa. This regulated pressure served as the source air for a mass flow controller, Sierra model C100L, which provided a range of flow from 3.3 cm^3/s to 166 cm^3/s. Next, a laminar flow element, CME model 10 (0–166 cm^3/s), is used for more accurate measurement of the actual air flow rate. This more accurate measurement is used to adjust the upstream mass flow controller set point. The air passes through a plate heat exchanger for optional temperature control. It then enters the fin test section. Ceramic resistance heaters provide the heat flux necessary, and power is adjusted to yield the desired junction temperature. Air flow exiting the fin section passes through porous aluminum foam to mix the air and get an accurate bulk air exit temperature. The test section was wrapped in insulation and placed in a Plexiglas enclosure to minimize the effect of ambient air motion in the laboratory. Heat transfer measurements were fully automated and controlled by a computer and a National Instruments data acquisition system.

The heater assembly had a copper base plate in contact with the fin section. Small grooves were machined to allow thermocouple placement. The assembly was fixed together with thermal epoxy. The channel flow experimental uncertainty was calculated in accordance with American Society of Mechanical Engineers (ASME) standard PTC 19.1-2005 [13].

In FY12, an air-cooling system-level test bench was completed (Figure 5). This test bench is intended for fan performance characterization, duct and plenum measurement, inverter module-level testing, and system-level demonstration. The air flow measurement section of the test bench follows ANSI/AMCA Standard 210-07 [14]. By using a series of nozzles, the flow chamber can maintain high accuracy measurements over a 5–500 CFM range. In the current configuration, air enters the chamber at plane 1, passing through the device under test (fan currently), and through plane 2, entering the larger chamber. Using a combination of the variable exhaust fan and blast gate controls, the pressure at plane 7 is controlled for back pressure on the fan. The air passes through settling screens and across the nozzle plate. The pressure drop across the nozzles, plane 5 to plane 6, is used to determine flow rate. The air then passes through additional settling screens and exits through the blast gate and variable exhaust blower.

The test bench was checked for repeatability, transducer hysteresis, and instrument impedance effects, all of which had negligible errors. An optical fan speed sensor was used to measure fan speed. Uncertainty and propagation of error analysis, per ASME standard PTC 19.1-2005 [13], determined an average U_{95} uncertainty in flow of ±1.2% and an average uncertainty in pressure of ±0.94%.

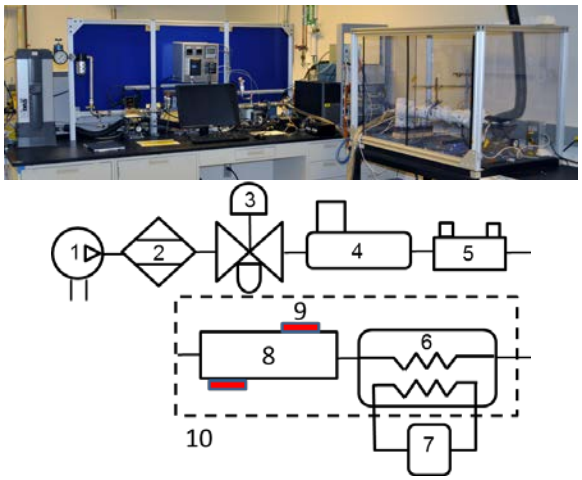

Figure 4: Photograph (top) and schematic (bottom) of the channel flow experimental setup: (1) compressed air, (2) desiccant dryer, (3) filter/regulator, (4) mass flow controller, (5) laminar flow element, (6) plate heat exchanger, (7) temperature control bath, (8) fin test section, (9) ceramic resistance heaters, and (10) isolation box

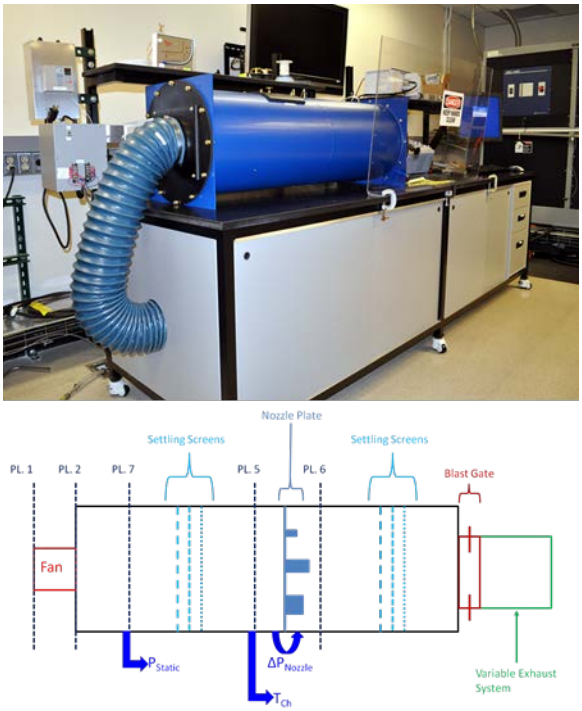

Figure 5: System-level air-cooling test bench picture and schematic

Numerical Methods

CFD models were created in ANSYS Fluent software for several stages of this project. For most of these models, convergence criteria were 10^{-3} for all residuals except energy and continuity for which the convergence criteria were tighter. More stringent convergence criteria were tested with minimal impact on results. Velocity and pressure residuals were also monitored. When needed, a k-ε turbulence model with enhanced wall treatments was utilized. For each model, the

This report is available at no cost from the National Renewable Energy Laboratory (NREL) at www.nrel.gov/publications.

results were confirmed to be mesh independent. To reduce computational expenses for the parametric optimization study, a full mesh sensitivity study was completed (Figure 6). It can be seen that as the mesh size increases, the time to converge increases and the relative error decreases. The circled point was selected for the parametric simulations to balance run time and accuracy. Simulations were run on a high-performance computer, using up to 32 computational cores in parallel.

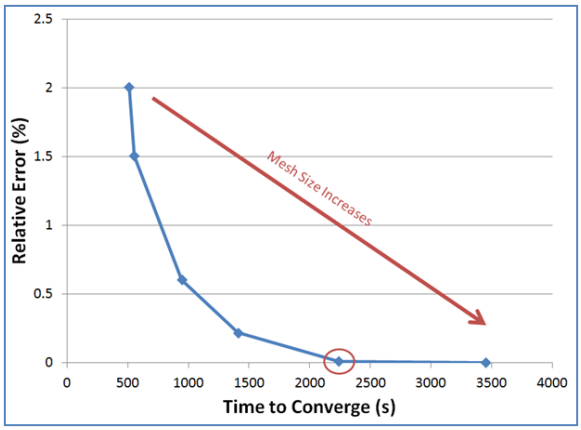

Figure 6: Mesh sensitivity plot for parametric optimization study. The circled point was selected.

Results

Thermal Constraints

Previous thermal constraints were revisited with updated device data provided by ORNL. Analytical equations were used to estimate the heat generation loads. The analytical model followed methods found in the literature for calculating conduction and switching losses for pulse-width modulation (PWM) inverters [15,16].

ORNL provided experimental data for high-temperature semiconductor device parameters collected as part of its wide bandgap benchmarking efforts. Data included device voltage as a function of temperature and current, turn-on energy losses, turn-off energy losses, and reverse recovery losses. Using the data provided, the transistor conduction loss, diode conduction loss, transistor switching loss, and diode switching loss were calculated over a range of operating conditions. These results were checked for consistency and also compared with overall inverter efficiency estimations.

Although heat loads will vary depending on operating conditions, the current operation condition, power factor, and junction temperature were all conservative. A safety factor of 1.5 was added to the metal-oxide-semiconductor field-effect transistor (MOSFET) heat loss, and that value was used for all devices, even though half of the devices are diodes with a lower heat generation rate under motoring conditions.

From this analysis, a design target for nine parallel modules (each module has 12 devices) of 2.7 kW of heat dissipation was determined, equating to a 95% efficient inverter (55 kW peak motoring power), as shown in Figure 7. The heat generation rate of all the devices was set at 25 W per device. For six parallel modules, a design target of 3.26 kW (94% efficiency, 45 W per device) was established, seen in Figure 8. Maximum junction temperatures ranging from 150°C to 200°C were selected to represent a range of near- to mid-term technologies, with 175ºC used for most analysis.

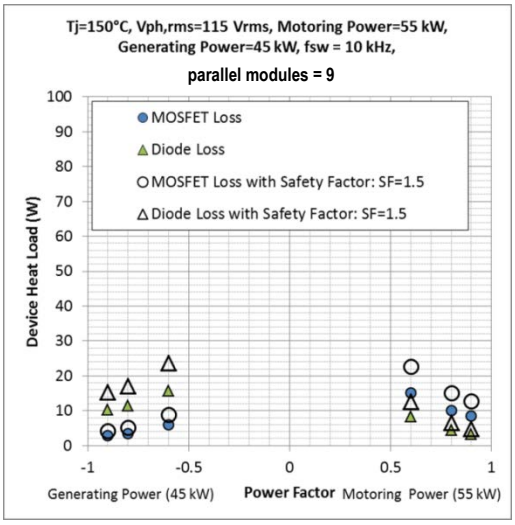

Figure 7: Heat generation rates for MOSFET and diode power electronic devices for nine parallel modules

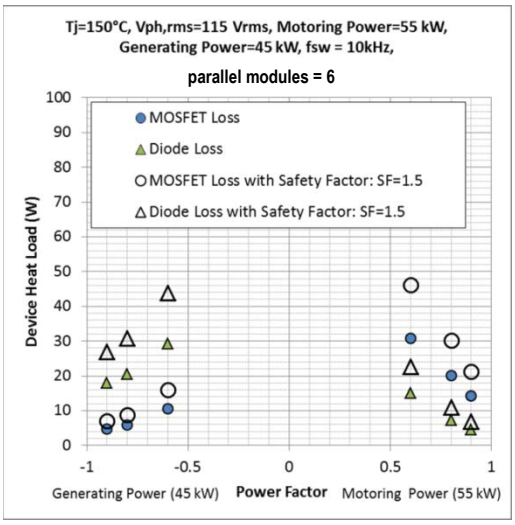

Figure 8: Heat generation rates for MOSFET and diode power electronic devices for six parallel modules

Heat Exchanger Optimization

With updated heat generation rates, optimization of the thermal design continued. The process is described in the previous year's annual report [17], but a short summary is provided here.

Using ANSYS Fluent and an NREL-developed "ANSYS Driver" tool, simulation parameters were selected and used in an iterative process, as described in [18]. Each device had a fixed heat generation rate and the air flow rate was updated using a Newton-Raphson method until the maximum device temperature (of either device) was 175ºC±1°C. Therefore, designs were compared on an equal heat transfer performance basis and this ensured that they would all meet the thermal requirements if allowed sufficient air flow rate.

This report is available at no cost from the National Renewable Energy Laboratory (NREL) at www.nrel.gov/publications.

The optimization was to reduce weight, cost, and fluid power (the product of volumetric flow rate and pressure drop). Reducing fluid power (parasitic losses) and weight and volume can be competing goals.

The baseline geometry was a design from ORNL consisting of rectangular fins. A one-sixth portion of the module (with one device on the top and one on the bottom of this sub-module) (Figure 9) was modeled simplify computational expense. Symmetry was used for full module extrapolation. Previous optimization showed the effect of various parameters, such as device location, fin thickness, and baseplate thickness. A constraint of 1 mm was also set for minimum thickness due to manufacturing concerns. Many of the parameters could be set at a near optimal level, while the length and height of the fins were the predominant parameters in meeting weight, volume, and acceptable fluid power targets.

In order to compare the design to the DOE targets for weight (specific power) and volume (power density), several assumptions must be made about the other components of the inverter in addition to the fin heat exchanger. The casing for the assembly was scaled with the fin block. ORNL provided several metrics for other components. The capacitor was assumed to be 1.62 kg and 1.13 L. The gate driver and control board were assumed to be 0.42 kg and 0.88 L. These values are typical or conservative. A 9x1 array of modules (Figure 10) is examined with the substrate for this model being based on direct-bond copper (DBC).

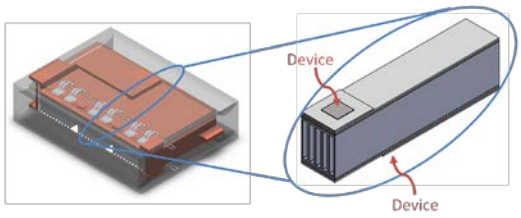

Figure 9: CFD model domain for fin optimization

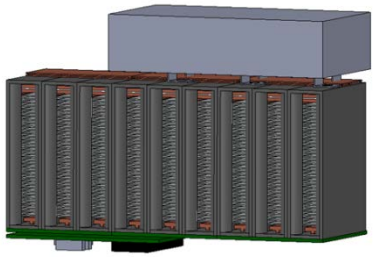

Figure 10: Illustration of inverter assembly for 9x1 arrangement

Using the same width as the baseline as well as fin thickness and channel width, the length and height of the fins were parametrically examined. Combining the weight and volume data with the other module components a map of designs can be shown. Figure 11 shows the normalized fluid power (fluid power of the new design normalized by the fluid power of the baseline) versus the specific power for fin heights (h) from 15 to 24 mm and fin lengths (l) of 30 to 60 mm. The 2015 and 2020 targets are also illustrated. Figure 12 shows the same map for power density.

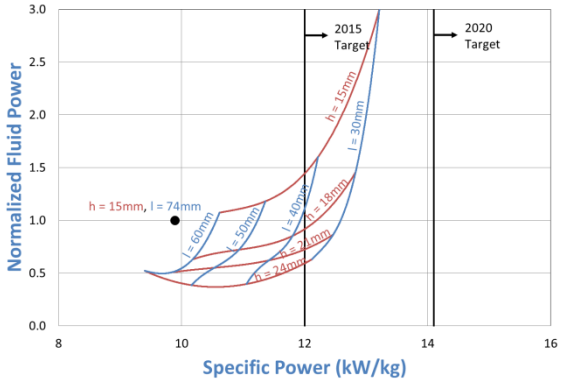

Figure 11: Optimized geometries with varying fin heights and lengths compared to baseline (black circle) and DOE's specific power technical targets for power electronics, 175°C junction temperature, 9x1 array, DBC, 25 W per device

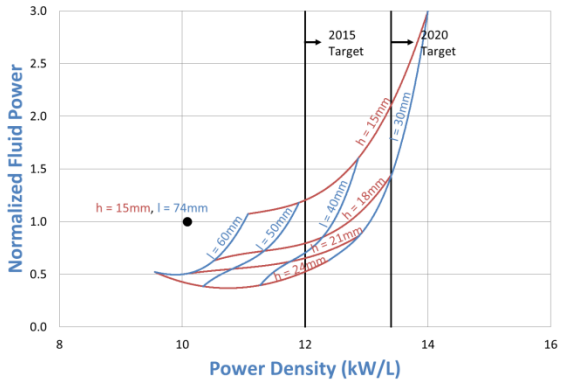

Figure 12: Optimized geometries with varying fin heights and lengths compared to baseline (black circle) and DOE's power density technical targets for power electronics, 175°C junction temperature, 9x1 array, DBC, 25 W per device

For both specific power and power density metrics, designs that were shorter in length (air flow direction) and taller in height were generally more favorable. Shorter fins reduced weight and volume, allowing the design to meet future targets. Increasing the height dropped the module fluid power.

In both cases, the contours become steeper, moving to the right. This indicates that there is a finite amount of material and volume that can be removed from the heat exchanger. To continue to improve the specific power and power density, improvements in other component weight and volumes must also be achieved. Figure 13, for example, shows the breakdown of the component weights. 2015 targets are met with the reduced weight of the heat exchanger assembly, but it becomes increasingly difficult to attain 2020 targets by reducing heat exchanger weight only. The same holds true for volume as well.

This report is available at no cost from the National Renewable Energy Laboratory (NREL) at www.nrel.gov/publications.

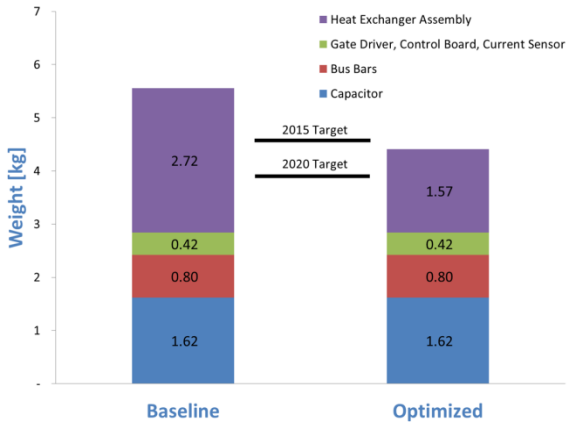

Figure 13: Modeled inverter weight breakdown by major components

Temperature contours of the sub-modules show the heat distribution of the devices to the aluminum fin block, as seen in Figure 14. The optimized fin block has a more symmetrical temperature gradient, indicating that the fins are efficient and maximizing the conduction through the solid as the air convects the heat out of the fin block.

A full module model was created for the baseline design to compare to the sub-module with symmetry design. The agreement between the two is fairly close, with some slight end effect variations, as seen in Figure 15. Note that Figure 14 has a device heat generation of 25 W per device whereas Figure 15 is for 30 W per device due to a different simulation being run.

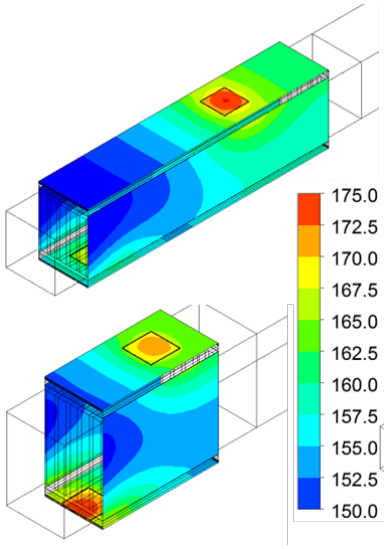

Figure 14: Temperature contours of baseline (top) and optimized (bottom) geometries [°C] for junction temperature of 175°C, direct-bond aluminum (DBA) substrate, 25 W per device

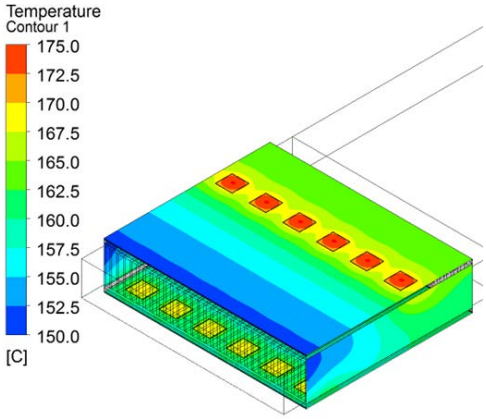

Figure 15: Full module baseline model temperature contours, 175°C junction temperature, 9x1 array, DBA, 30 W per device

Figure 16 shows the predicted performance of a 9x1 arrangement with 175°C junction temperature in more detail for an optimized geometry with a fin height of 21 mm and fin length of 30 mm. The intersection of the fan curve and the predicted 9x1 inverter pressure loss results in a 0.054 m^3/s (115 CFM) flow rate. The heat dissipation at this flow rate is approximately 3.2 kW, exceeding the conservative 2.7 kW target.

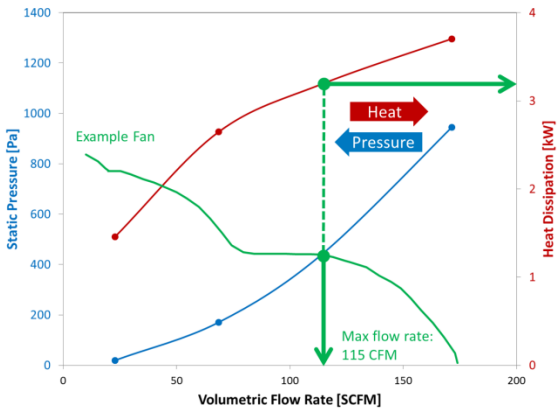

Figure 16: Pressure loss and heat dissipation for optimized fin geometry operating at a 175°C junction temperature

Although the module may be optimized for thermal performance compared to the baseline, which is somewhat arbitrary, it is more beneficial to examine the module thermal performance in the context of the entire system.

System Performance Optimization

Previous work measured the pressure loss of various production ducts using the system level test bench (Figure 17). Two of the ducts are combined to estimate the inlet and outlet ducting from the inverter as a surrogate for the ducting system required.

The fluid power required for various flow rates is generally much higher for the ducting than it is for the air-cooling heat exchanger. Therefore, a system-level analysis is needed to draw conclusions about the optimized design. It may be that the heat exchanger is optimized to minimize fluid power on the inverter level due to a high flow rate and low pressure drop

This report is available at no cost from the National Renewable Energy Laboratory (NREL) at www.nrel.gov/publications.

across the fins, but for the system level, this would cause a higher overall fluid power requirement. In general, for the system, a lower flow rate is desired because the pressure drop across the ducting rises as the square of the flow velocity.

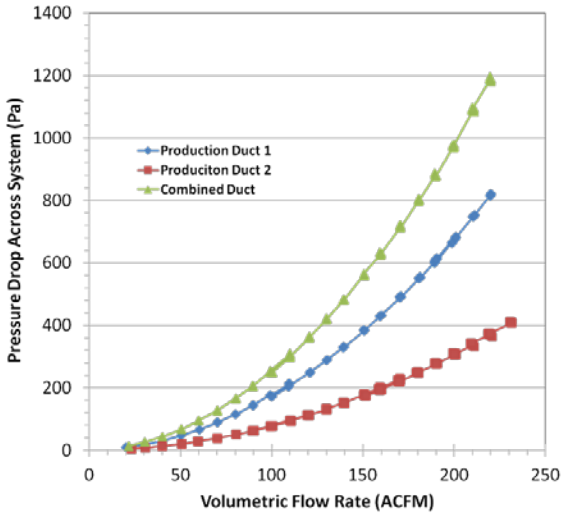

Figure 17: Pressure loss of production ducts

A similar parametric study using DBA substrates was conducted. The differences between using DBA and DBC substrates is small, and the overall conclusions based on geometry optimization are consistent.

Fin geometries with heights of 18 mm to 27 mm and fin lengths of 30 to 60 mm were examined with heat generation rates of 25 W per device (9x1 array of modules [see Figure 10]) and 45 W per device (6x1 array of modules) with DBA substrates and a maximum junction temperature of 175°C. The sub-module had a fixed width of 15 mm (same as the baseline design) and five channels (fin thickness of 1 mm, channel width of 2 mm).

Figure 18 shows the map of results for the 9x1 array of modules. The scale is maintained for direct comparison with the 6x1 array, Figure 19. For reference, the value for the baseline design is shown.

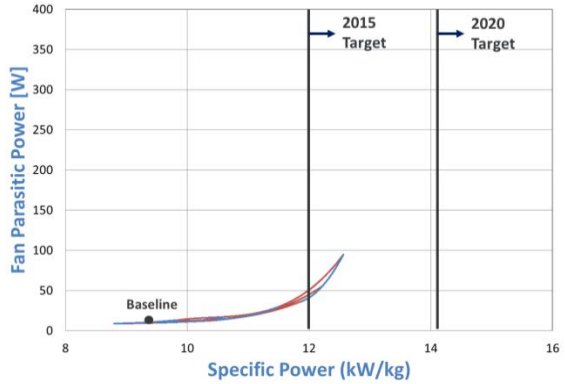

Figure 18: Specific power and fan parasitic power for 9x1 array of modules, 175°C junction temperature, DBA, 25 W per device

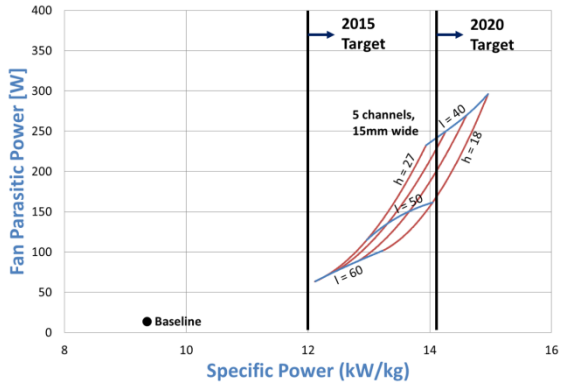

Figure 19: Specific power and fan parasitic power for 6x1 array of modules, 175°C junction temperature, DBA, 45 W per device, five channels per device pair (top and bottom devices)

When using a system-level analysis to achieve weight and volume targets (Figure 20), the fins tend to need to be shorter in height. By making the fin block shorter in length, the specific power and power density increase for the same fin height, but a penalty is paid with an increased fluid power requirement. For just the module, optimization indicated that the fin block should be taller in height and shorter in length. On this system level, it is more advantageous to allow for a higher pressure drop across the module while decreasing the flow rate so that the fluid power requirement of the ducting is limited as much as possible while still being able to dissipate the heat requirement.

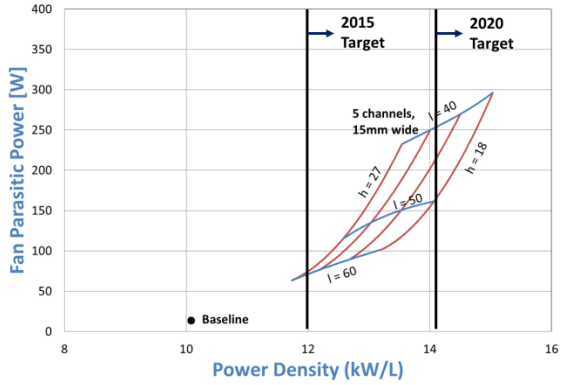

Figure 20: Power density and fan parasitic power for 6x1 array of modules, 175°C junction temperature, DBA, 45 W per device, five channels per device pair (top and bottom devices)

Although there are no technical targets for the coefficient of performance or parasitic power, this metric should be examined for market acceptability. For comparison, a typical vehicle air-conditioning blower or condenser pulls about 50 W of power at steady-state conditions and 150 W of power under peak loads.

By expanding the design space but still using a simple rectangular channel design, further potential designs are found. Variations of channel width, fin thickness, number of channels per top and bottom devices (the sub-module modeled) while maintaining the 175°C junction temperature and 45 W per device heat generation were examined, with a

This report is available at no cost from the National Renewable Energy Laboratory (NREL) at www.nrel.gov/publications.

few potential promising designs. For example, a sub-module design with 10 channels instead of 5, which also makes the whole module wider, yields parasitic power below 50 – 75 W, while attaining around 13 kW/kg specific power.

The thermal design must remove the amount of heat targeted within the constraints given, but the electrical design must also fit on the heat exchanger footprint. Additional constraints are being iterated on in discussions with ORNL, especially minimum footprint and spacing requirements for the devices. Although a thermal design may be optimal for heat removal, it must also work for the electrical topology. Conversely, the electrical design must be such that a heat exchanger can be designed to remove the heat while meeting the weight and volume targets.

The heat exchanger approach has been to keep the design relatively simple so that it may be easily manufactured. The current design of rectangular channels is conducive to extrusion techniques. Extruding aluminum is also advantageous over casting because aluminum with higher thermal conductivity may be used. In addition to meeting the thermal requirements, the design may be optimized for manufacturability to reduce costs.

Experimental design validation

The air cooling technology characterization platform test section was updated for a two heater-fin test section, as seen in Figure 21. Figure 22 shows the test section. The tabs on the side are for experimental assembly purposes. Results will be used to validate and update the models.

Figure 21: Test section for testing baseline aluminum fins with two heaters for model validation; pressure calibration testing shown. (Photo Credit: Scot Waye, NREL)

Figure 22: Baseline aluminum fin block sub-module test section

Conclusions and Future Directions

- A heat exchanger design based on nine modules may attain 2015 targets, but the dimensions may be prohibitive for the electrical design. The six-module solution, even though the heat generated and dissipated is higher, appears to be more promising to reach 2015 as well as 2020 targets.
- A system-level analysis is critical to the thermal design so the heat exchanger design rejects the heat while maintaining a maximum junction temperature and meets weight and volume targets without requiring excessive parasitic power to drive the flow.
- The thermal design must also consider the electrical topology for allowance of all the required components and spacing as well as the ability to manufacture it at an acceptable cost.

Future work includes:

- Prototype and test optimized and advanced fin designs. Improve models based on test results. Down select best design for prototype module.
- Test balance-of-system components (fans and ducting). Incorporate results into system-level model. Develop initial high-temperature air-cooled inverter balance-of-system design. Demonstrate operation of thermal system design.
- Test optimized module design for thermal performance and in combination with high-temperature electronics from ORNL. Results will feed into improved design and future high-temperature air-cooled inverter demonstration with ORNL.

FY 2013 Patents/Publications/Presentations

1. Arik, M., Sharma, R., Lustbader, J., He, X., 2013, “Steady and Unsteady Air Impingement Heat Transfer for Electronics Cooling Applications.” *ASME Journal of Heat Transfer,* 135, pp. 111009-1 – 111009-8.
2. Bennion, K., Lustbader, J. U.S. Patent. “Integrated three-dimensional module heat exchanger for power electronics cooling.” Number US 8541875, September 24, 2013.

This report is available at no cost from the National Renewable Energy Laboratory (NREL) at www.nrel.gov/publications.

3. Lustbader, J. "Air Cooling Technology for Power Electronics Thermal Control." Presentation, DOE Annual Merit Review; May 13–15, 2013. Arlington VA.

Acknowledgments

The author would like to acknowledge the support provided by Susan Rogers and Steven Boyd, Technology Development Managers for Advanced Power Electronics and Electric Motors, Vehicle Technologies Office, U.S. Department of Energy Office of Energy Efficiency and Renewable Energy. The significant contributions of Jason Lustbader, Casey Smith, Matt Musselman, Charlie King, and Kevin Bennion (NREL) to the project are acknowledged. Collaboration with Madhu Chinthavali from ORNL has been important in balancing the electrical and thermal design and constraints. The author would also like to acknowledge SAPA for providing aluminum fin block prototypes.

References

1. Staunton, R.H.; Burress, T.A.; Marlino, L.D. *Evaluation of 2005 Honda Accord Hybrid Drive System.* ORNL/TM-2006/535. Oak Ridge, TN: Oak Ridge National Laboratory, September 2006.
2. "Semikron Application Manual 1998" http://www.semikron.com/skcompub/en/application_manual-193.htm. Section 3.1. Accessed on July 7th, 2011.
3. Matsumoto, S. "Advancement of Hybrid Vehicle Technology." *European Conference on Power Electronics and Applications,* Dresden, Germany, September 2005.
4. Uesugi, T.; Kachi, T. "GaN Power Switching Devices for Automotive Applications." CSMan Tech Conference, Tampa, Florida, May 2009.
5. Renken, F.; Knorr, R. "High Temperature Electronics for Future Hybrid Powertrain Application," *European Conference on Power Electronics and Applications*, Dresden, Germany, September 2005.
6. Funaki, T.; Balda, J.; Junghans, J.; Kashyap, A.; Mantooth, H.; Barlow, F.; Kimoto, T.; and Hikihara, T., 2007, "Power conversion with SiC devices at extremely high ambient temperatures," *IEEE Transactions on Power Electronics*, 22- 4, pp. 1321 –1329.
7. Chow, Y. (media contact) "AC Propulsion Partners with BMW to Build 500 Electric Vehicles." Press release. 2008. http://www.acpropulsion.com/pressreleases/11.20.2008%20BMW%20Press%20Release.pdf. Accessed July 6th, 2011.
8. Kodani, K.; Tsukinari, T.; and Matsumoto T., "New Power Module Concept by Forced-Air Cooling System for Power Converter." *IEEE 2010 International Power Electronics Conference*, Sapporo, Japan, July 2010.
9. Bortis, D.; Wrzecionko, B.; Kolar, J.W. "A 120°C ambient temperature forced air-cooled normally-off SiC JFET automotive inverter system." *IEEE 26th Annual Applied Power Electronics Conference and Exposition (APEC)*, Fort Worth, TX, March 2011.
10. Wrzecionko, B.; Biela, J; and Kolar J. "SiC Power Semiconductors in HEVs: Influence of Junction Temperature on Power Density, Chip Utilization and Efficiency." *IEEE 35th Annual Industrial Electronics Conference,* Porto, Portugal, November 2009.
11. Vetrovec, J. "High-Performance Heat Sink for Interfacing Hybrid Electric Vehicles Inverters to Engine Coolant Loop." *SAE World Congress.* Paper# T11PFL-0459, Detroit, MI, April 2011.
12. Lustbader, J., Bennion, K., He, X. 2011, "Air-Cooling Technology for Power Electronics," FY2011 DOE Annual Progress Report for Advanced Power Electronics and Electric Motors.
13. Dieck, R.H., Steele, W.G., Osolsobe, G. *Test Uncertainty*. ASME PTC 19.1-2005. New York, NY. American Society of Mechanical Engineers. 2005.
14. Laboratory Methods of Testing Fans for Certified Aerodynamic Performance Rating. Standard ANSI/AMCA 210-07, ANSI/ASHRAE 51-07. AMCA: Arlington Heights, IL. August 2007.
15. Mestha, L.K., Evans, P.D., 1989, "Analysis of on-state losses in PWM inverters," *Electric Power Applications, IEEE Proceedings B*, 136- 4, pp. 189–195.
16. Infineon, "Dimensioning Program IPOSIM for Loss and Thermal Calculation of Infineon IGBT Modules." February 2006.
17. Lustbader, J. 2012, "Air-Cooling Technology for Power Electronics Thermal Management," FY2012 DOE Annual Progress Report for Advanced Power Electronics and Electric Motors.
18. Bennion, K., Cousineau, J., Lustbader, J. 2012, "Integrated Module Heat Exchanger," FY2012 DOE Annual Progress Report for Advanced Power Electronics and Electric Motors.

This report is available at no cost from the National Renewable Energy Laboratory (NREL) at www.nrel.gov/publications.

Electric Motor Thermal Management

Principal Investigator: Kevin Bennion
National Renewable Energy Laboratory (NREL)
Transportation and Hydrogen Systems Center
15013 Denver West Parkway
Golden, CO 80401
Phone: 303-275-4447
E-mail: Kevin.Bennion@nrel.gov

DOE Technology Development Manager: Susan A. Rogers
Phone: 202-586-8997
E-mail: Susan.Rogers@ee.doe.gov

NREL Task Leader: Sreekant Narumanchi
Phone: 303-275-4062

Start Date: October 2009
End Date: September 2013

Objectives

With the push to reduce component volumes, lower costs, and reduce weight without sacrificing performance or reliability, the challenges associated with thermal management increase for power electronics and electric motors. Thermal management for electric motors will become more important as the automotive industry continues the transition to more electrically dominant vehicle propulsion systems. The transition to more electrically dominant propulsion systems leads to higher-power duty cycles for electric drive systems. Thermal constraints place significant limitations on how electric motors ultimately perform, and as thermal management improves, there will be a direct trade-off between motor performance, efficiency, cost, and the sizing of electric motors to operate within the thermal constraints (Figure 1).

The goal of this research project is to characterize the current state of thermal management technologies for electric traction-drive motors and quantify the impact of thermal management on the performance of electric motors. The ultimate goal is to identify areas for improvement and knowledge gaps that would benefit from additional research, leading to focused efforts within the identified areas. The research objectives are summarized as follows:

- Establish a foundation on which to evaluate potential improvements to electric motor thermal management
- Quantify opportunities for improving cooling technologies for electric motors
- Link thermal improvements to their impact on advanced power electronics and electric motor (APEEM) targets to prioritize future research
- Increase available information to support thermal management of electric motors in the public domain.

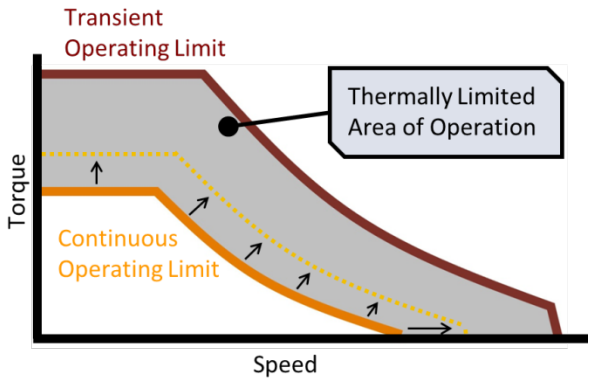

Figure 1: Illustration of thermal management impact on motor performance as continuous power demands increase with higher electrical duty cycles

The focus for FY13 emphasized the final objective to increase the available information to support thermal management of electric motors. Past work highlighted potential areas where improvements in motor thermal management could impact motor performance [1], and during FY13, NREL's core thermal analysis and experimental capabilities were developed and applied to increase available data to improve the thermal design of electric motors. The work is on the path towards commercialization because the data and results have been used by industry and are necessary to improve motor designs.

Technical Barriers

The technical challenge of motor thermal management is summarized by Hendershot as "[h]eat transfer is as important as electromagnetic and mechanical design. The analysis of heat transfer and fluid flow in motors is actually more complex, more nonlinear, and more difficult than the electromagnetic behavior." [2]. A significant barrier to research in motor thermal management is the wide variation in motor types and designs. The analysis, data collection, and thermal management technologies should be applicable to as many motor configurations as possible. For this reason we collaborated with industry, university and research partners with expertise in alternative electric motor designs. The variation in thermal loads in terms of location and magnitude for different operating conditions presents another significant challenge. The variation in heat generation magnitude and location based on the operating conditions of the motor require the ability to evaluate the impact of thermal management technologies under multiple operating conditions.

Technical Targets

The DOE technical targets applicable to this research are the goals outlined in the Electrical and Electronics Technical Team Roadmap [3]. Specifically, the 2015 motor technical targets are $7/kW, 1.3 kW/kg, and 5 kW/L. Thermal management of electric motors supports improvements in each of the technical targets because of impacts on current density, material costs, and magnet costs (dysprosium). In addition, thermal management of the electric motor impacts efficiency and reliability.

This report is available at no cost from the National Renewable Energy Laboratory (NREL) at www.nrel.gov/publications.

Accomplishments

- Designed and fabricated an experimental apparatus to test the forced convection heat transfer performance of automatic transmission fluid (ATF)
- Evaluated the effects of temperature and jet velocity on ATF heat transfer coefficients
- Estimated the thermal performance of ATF jet impingement cooling of electric motors by testing samples with surface features simulating wire bundles
- Increased publically available information on ATF jet impingement cooling performance
- Expanded lamination tests to measure the thermal contact resistance between laminations, which is critical for modeling the axial flow of heat through the electric motor.

✧ ✧ ✧ ✧ ✧

Introduction

The ability to remove heat from the electric motor depends on the passive stack thermal resistances within the motor and the convective cooling performance of the selected cooling technology. The passive thermal design refers to the geometrical layout, material selection, and thermal interfaces that affect the heat spreading capabilities within the motor. The ability for heat to spread through the motor affects the thermal temperature gradients within the motor. The convective cooling technology is the cooling mechanism that ultimately removes the heat from the motor and transfers the heat to another location to reject the heat to the ambient environment. Without the ability to remove heat, the motor cannot operate without sacrificing performance, efficiency, and reliability.

During FY13, work continued from past efforts to characterize the passive thermal stack of the motor. Past work generated preliminary thermal data for materials and key thermal interfaces within the electric motor. The thermal data were incorporated into parametric thermal models for electric motors. The interest from industry into the passive thermal stack measurement results led to expanded tests to characterize the thermal contact resistance between motor laminations. During FY13, the test procedure was developed, and tests were performed for one sample lamination material. This work will continue as part of a new project in FY14, and a publication is scheduled for FY14 to outline the procedure and results.

The primary focus during FY13 involved characterizing the convective cooling technologies incorporating ATF. Figure 2 provides a cut cross section view illustrating general convective cooling approaches for automotive traction drive applications. One approach to cooling the motor includes a cooling water jacket incorporated into the motor housing that surrounds the motor stator. The water jacket is typically cooled with a mixture of water and ethylene glycol. When the motor is packaged within the transmission it is also possible to use ATF or other oils to cool the motor. While ATF does not perform as well as the water/ethylene glycol mixture as a coolant, the ability to use ATF

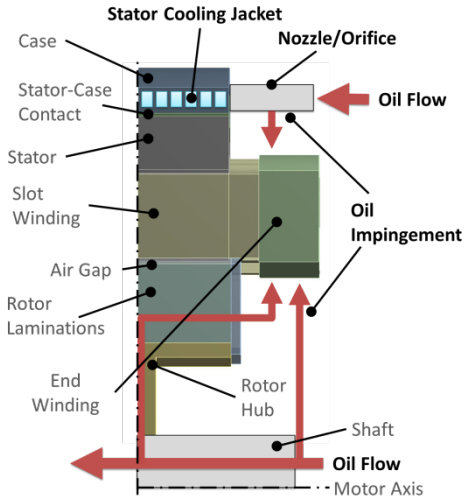

Figure 2: Illustration of typical thermal management approaches incorporating a stator cooling jacket and oil cooling with ATF within the rotor and end windings

to directly cool the rotor or motor end windings has significant advantages for removing heat. However, the flow of the ATF oil as it impinges onto the end winding is a complicated heat transfer and fluid dynamics problem. An understanding of the heat transfer of the ATF as it impinges onto the end windings is critical for motor designers in industry in order to maximize the performance of the motor while providing the required reliability and efficiency. The lack of available data for the convective cooling performance of ATF impinging jets is an important gap in the ability to model and design electric motors for automotive traction drive systems. During FY13, we focused on addressing this gap.

ATF Convective Cooling Performance

Cooling of the electric motors in some hybrid vehicles is accomplished by impinging ATF jets onto the motor's copper windings [4]. This cooling method is practical because ATF fluid is a dielectric and because, in some cases, the electric motors are housed within the vehicle's transmission or transaxle where ATF fluid is readily available. Although this cooling method is common, currently there is minimal publicly available information regarding the jet impingement performance of ATF fluids.

In this study, we provide the results of recent experiments characterizing the thermal performance of ATF jets. Ford's Mercon LV was the ATF evaluated in this study. Experiments were carried out at various ATF temperatures and jet velocities to quantify the influence of these parameters on heat transfer coefficients. Fluid temperatures were varied from 50°C to 90°C to encompass potential operating temperatures within an automotive transaxle environment. The jet nozzle velocities were varied from 0.5 to 10 m/s. The lower jet velocities are typical of ATF jet impingement velocities within current automotive motor cooling systems. Higher jet velocities up to 10 m/s were included to investigate the impact of more aggressive jet impingement.

This report is available at no cost from the National Renewable Energy Laboratory (NREL) at www.nrel.gov/publications.

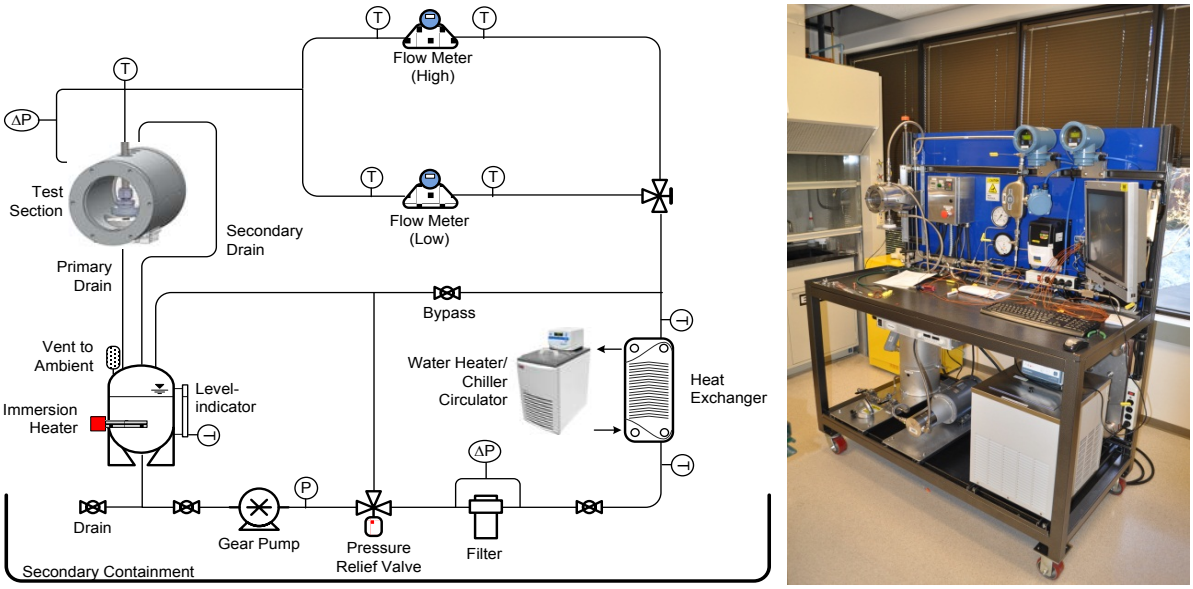

Figure 3: Test flow loop schematic (left) and picture (right)

The experimental ATF heat transfer coefficient results provided in this report are a useful resource for engineers designing ATF-based motor cooling systems. Moreover, results from this study may also be applicable to potential ATF cooling strategies for automotive power electronics components to support situations where the power electronics are integrated with the electric motor.

Approach

A schematic of the experimental test loop is provided in Figure 3. The test loop was designed and fabricated to characterize the forced convection thermal performance of ATF. The loop can be configured to conduct jet impingement or channel flow tests and can accommodate a variety of test articles (e.g., small test heaters or larger electric motors). Fluid flow rates of up to 20 liters per minute (Lpm) and fluid temperatures of up to 110°C can be produced by the system.

Approximately 15 liters of Mercon LV ATF are contained within the loop. The fluid is circulated through the loop via a variable-frequency-drive-controlled gear pump. Two Coriolis mass flow meters are provided to measure fluid flow rates. The low-flow-rate flow meter has a range of 0–2 Lpm and provides accurate measurements at lower flow rates. The high-flow-rate flow meter has a range of 2–20 Lpm and allows for accurate measurements at higher flow rates. System fluid temperatures are controlled and maintained constant using a heater/chiller bath circulator and flat-plate heat exchanger system as well as an immersion heater located within the reservoir tank. Temperature (K-type thermocouples) and pressure sensors are located throughout the loop as shown in Figure 3.

ATF jet impingement experiments were conducted within the test section shown in Figure 4. Fluid entered the test section through a tube at the top of the chamber. Fluid then flowed through a nozzle plate to generate an impinging jet onto the test sample. The nozzle was a simple orifice type with a 2-mm orifice diameter (d). Drain ports at the front and back of the vessel allowed the fluid to gravity drain and create a free-jet condition (i.e., non-flooded). A thermocouple located just upstream of the test section measured the fluid inlet temperature. A differential

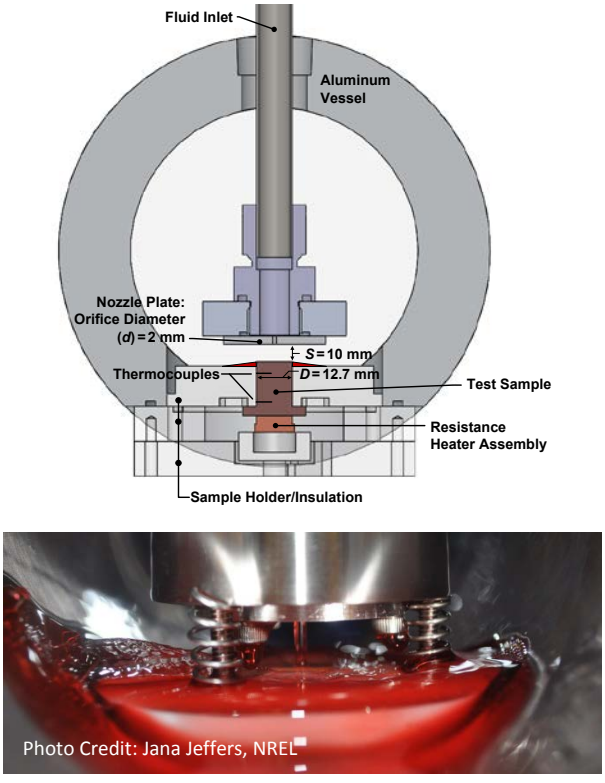

Figure 4: Schematic (top) and picture (bottom) of the test section showing the nozzle and test sample

This report is available at no cost from the National Renewable Energy Laboratory (NREL) at www.nrel.gov/publications.

pressure transducer measured the pressure drop across the nozzle. Viewports on the front and back of the test section enabled visualization of the experiments as shown in Figure 4.

The test samples, fabricated from oxygen-free copper, had an impingement or cooled surface diameter (D) of 12.7 mm. The copper test samples were inserted into Teflon disks ("sample holder/insulation" part in Figure 4) for support and thermal insulation. A combination of high-temperature silicone sealant and epoxy was applied around the test samples and between the samples and Teflon to prevent fluid leaks. Two calibrated K-type thermocouples were embedded within the sample to measure heat fluxes and to calculate surface/wall temperature. The sample was heated using a computer-controlled power supply that powered a resistance heater assembly attached to the lower side of the sample. Thermal interface material (grease) applied between the resistance heater assembly and the test sample reduced the contact resistance between the resistance heater assembly and the test sample.

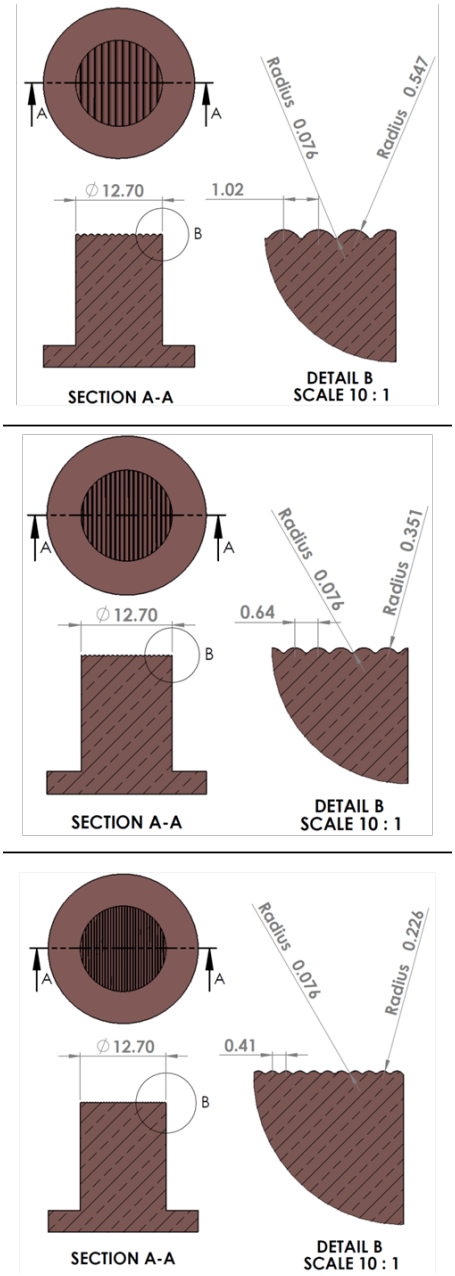

Figure 5: Computer-aided design models of the 18 AWG (top), 22 AWG (middle), and 26 AWG (bottom) samples. Dimensions shown are in millimeters. The top 12.7-mm-diameter surface was the jet impingement surface.

The thermal performance of four test samples with different surface features were evaluated under jet impingement (free-jet) cooling conditions. The baseline sample was sandpaper-polished (600 grit) to create a smooth/plain impingement surface. The other three samples were fabricated (via wire electrical discharge machining) with surface features that were intended to simulate wire bundles found in electric motors. The features on these samples consisted of a series of parallel circular ridges running straight across the impingement surface (Figure 5 and Figure 6). The radius of these ridges corresponds to the radius of the American wire gauge (AWG) (i.e., 18 AWG, 22 AWG, or 26 AWG) plus the thickness of the wire insulation based on Polyurethane-180 heavy build insulation from MWS Wire Industries. Relevant dimensions of these test samples along with impingement surface area measurements are provided in Table 1.

Table 1: Test Sample Feature Dimensions and Surface Area Measurements

	Baseline	18 AWG	22 AWG	26 AWG
Radius, mm (wire and Insulation)	N/A	0.547	0.351	0.226
Total wetted surface area, mm^2	126.7	148.2	143.3	139.2

The nozzle and test sample assembly were aligned vertically and the nozzle-to-impingement-surface distance (S) was set to 10 mm (S/d = 5). The test sample and nozzle assembly were then installed within the test section. The gear pump was

Figure 6: 18 AWG surface target: Top view (left), side view (right).

This report is available at no cost from the National Renewable Energy Laboratory (NREL) at www.nrel.gov/publications.

activated, and the fluid was circulated through the loop. The bath circulator and the immersion heater were then turned on to achieve the desired test section fluid inlet temperature. Once the system reached the set point temperature, the pump speed was adjusted and the bypass valve was throttled to achieve the desired flow rate. Upon achieving the desired fluid conditions, the experiments were initiated.

A LabVIEW program controlled and monitored experiments via a data acquisition system and direct current power supply. For these experiments, the power supply powered the resistance heater that heated the test sample. Power was adjusted to achieve a test sample impingement surface temperature of approximately 110°C. Once temperature equilibrium was reached, the program recorded temperature, pressure, and flow rate data and calculated the heat transfer coefficient values. For every case, the heat transfer coefficients ($\bar{h}$) were defined according to Equation 1.

$$\bar{h} = \frac{Q}{A_p(T_w - T_l)} \quad (1)$$

Q is the heat dissipated through the top 12.7-mm-diameter surface, and Tw is the sample's average impingement surface temperature. Both values (Q and Tw) were calculated via the two thermocouples embedded within the test sample, assuming one-dimensional, steady-state heat transfer. Due to the highly conductive properties of the oxygen-free copper samples, the calculated surface temperature (Tw) is taken to be an average of the surface temperatures. In other words, Tw is the average temperature of the stagnation and wall-jet regions on the test sample. For the baseline sample, Tw is the average impingement surface temperature. For the other samples, Tw is calculated at a plane of constant cross-sectional area just below the surface protrusions/features. Ap is the surface area of the 12.7-mm-diameter impingement area (the increased surface area from the features in the 18 AWG, 22 AWG, and 26 AWG samples is not included), and T_l is the temperature of the liquid jet, as measured by the thermocouple probe immediately upstream of the nozzle. System parameters relevant to this study are summarized in Table 2. Every test condition was repeated a minimum of three times.

Table 2: Test Sample Feature Dimensions and Surface Area Measurements

D (mm)	d (mm)	S (mm)	S/d	D/d
12.7	2.06	10	5	6.2

Results

Experiments were conducted to characterize the thermal performance of Mercon LV ATF impinging jets (free jets). The effect of fluid jet velocity and temperature on heat transfer coefficients was measured. Jet velocities of approximately 0.5 m/s, 2.8 m/s, 5 m/s, 7.5 m/s, and 10 m/s and fluid temperatures of 50°C, 70°C, and 90°C were studied. A significant amount of fluid heat was lost to the ambient environment at the highest fluid temperature tested. This prevented us from conducting experiments at lower fluid velocities with a fluid temperature of 90°C. Therefore, 90°C fluid temperature experiments were only conducted at velocities equal to or greater than 5 m/s.

Figure 7 displays the average heat transfer coefficient results for the baseline sample at inlet fluid temperatures of 50°C, 70°C, and 90°C. The heat transfer coefficient results provided are an average of all test runs completed. As expected, the heat transfer coefficients increased with increasing impinging jet velocity. Varying the inlet temperature had minimal influence on heat transfer coefficients for the flat target surface.

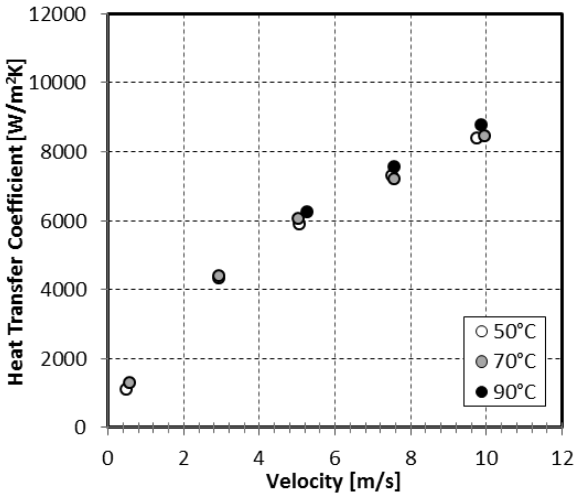

Figure 7: Baseline sample heat transfer coefficient results

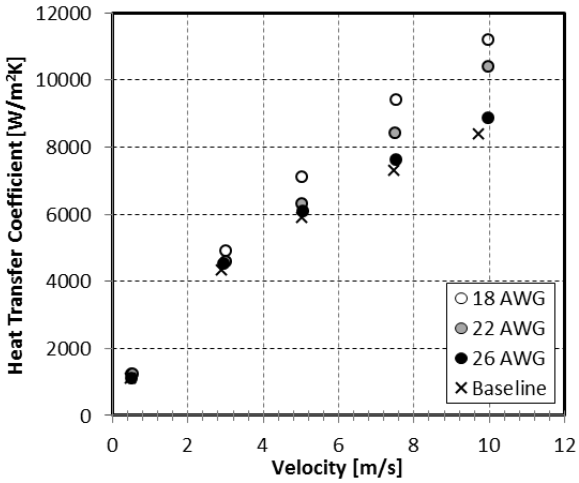

Figure 8: Heat transfer coefficients of all target surfaces at 50°C inlet temperature

This report is available at no cost from the National Renewable Energy Laboratory (NREL) at www.nrel.gov/publications.

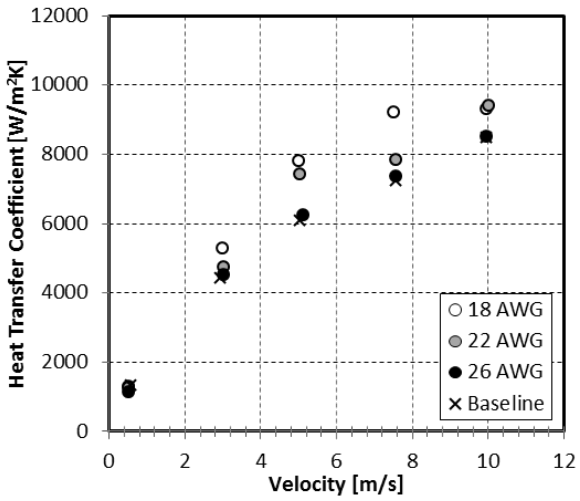

Figure 9: Heat transfer coefficients of all target surfaces at 70°C inlet temperature

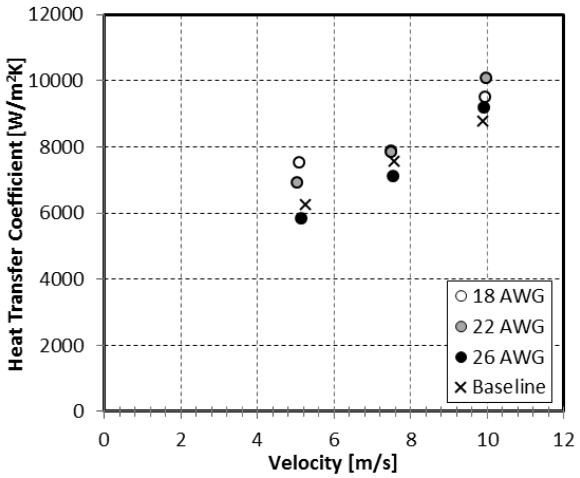

Figure 10: Heat transfer coefficients of all target surfaces at 90°C inlet temperature

Figures 8, 9, and 10 compare data from all samples tested at inlet temperatures of 50°C, 70°C, and 90°C, respectively. All the heat transfer coefficient values are averaged values computed from multiple test runs for each sample. At the lowest jet velocity tested (0.5 m/s), all four samples provided about the same performance (Figures 7 and 8). This suggests that the wire bundle features of the 18 AWG, 22 AWG, and 26 AWG samples had minimal effect on performance at this low jet velocity (i.e., a jet velocity consistent with automotive ATF motor cooling applications). Variations in the performance of the samples are more apparent at higher jet velocities. At more elevated jet velocities, the 18 AWG and 22 AWG test samples did provide some heat transfer coefficient enhancement as compared to the baseline sample. In all cases, the 26 AWG sample and the baseline sample produced almost identical results, indicating that the surface features on this sample had minimal effect on performance.

For the 50°C temperature case (Figure 8), the heat transfer coefficient results for the various samples are in line with the surface area measurements provided in Table 1—the greater the surface area, the higher the heat transfer coefficients. At 50°C, the 18 AWG sample with the highest surface area outperformed all samples. At lower jet velocities, the test samples with the wire features perform similar to the baseline flat surface.

The performance trends at higher fluid temperatures are less clear. At 70°C and 90°C (Figures 9 and 10), fluid splatter was observed for the 18 AWG, 22 AWG, and 26 AWG samples at higher jet velocities. This phenomenon is associated with fluid being deflected off the surface by the samples' round, protruding features. This deflection reduced the amount of fluid supplied to the outer sections of the samples, leading to reduced performance. This effect was a random, uncontrolled event leading to variation in the results and was more pronounced with the 18 AWG and 22 AWG samples. Evidence of this splattering effect is indicated by a plateau in the heat transfer coefficient curves at the higher jet velocities as seen in Figure 9. The effect is less clear at 90°C in Figure 10, but the 18 AWG sample shows the largest effects due to fluid splattering. Figure 11 shows images of the ATF jet impingement with and without the fluid splatter.

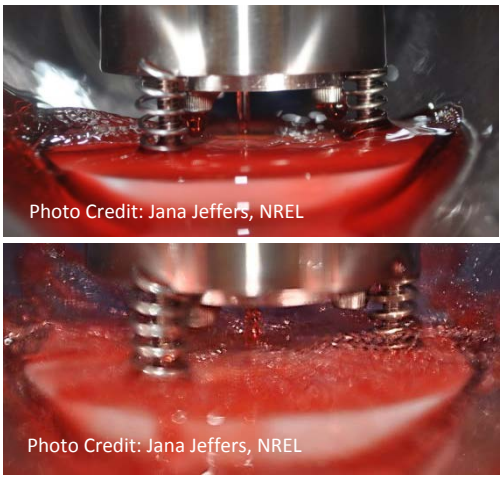

Figure 11: ATF flowing over surface (top), ATF deflecting off surface (bottom)

Figure 12 represents only data from the 18 AWG sample and focuses on the trends in the heat transfer coefficient with increasing jet velocity and inlet temperature. For the 50°C inlet temperature, the heat transfer coefficient increases almost linearly with nozzle velocity. At this temperature, the surface splattering described above did not occur. At a 70°C inlet temperature and at approximately 7.5 m/s, the fluid impinged on the center of the sample surface and moved outward over the entire surface. Conversely, at 10 m/s, some of the fluid deflected off the surface immediately after impingement, and this effect is manifested as a plateau in the 70°C heat transfer coefficient curve at the higher velocities. In the 90°C data, fluid splatter was observed to occur at lower velocities. Because the fluid splatter was more prevalent at higher temperatures, we speculate that the lower ATF viscosities at higher temperatures are more conducive to this splattering effect. The higher jet velocities

This report is available at no cost from the National Renewable Energy Laboratory (NREL) at www.nrel.gov/publications.

examined in this project are not currently used within automotive ATF motor cooling applications because of potential wire insulation reliability issues. These elevated velocities were evaluated here to characterize the thermal performance of ATF fluids over a wide jet velocity range.

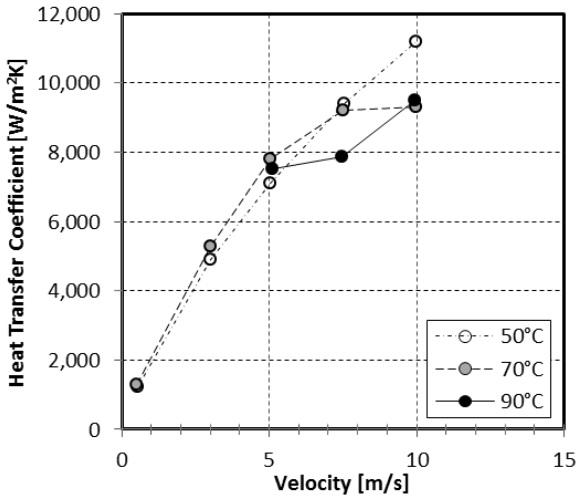

Figure 12: Heat transfer coefficients of 18 AWG sample for all inlet temperatures

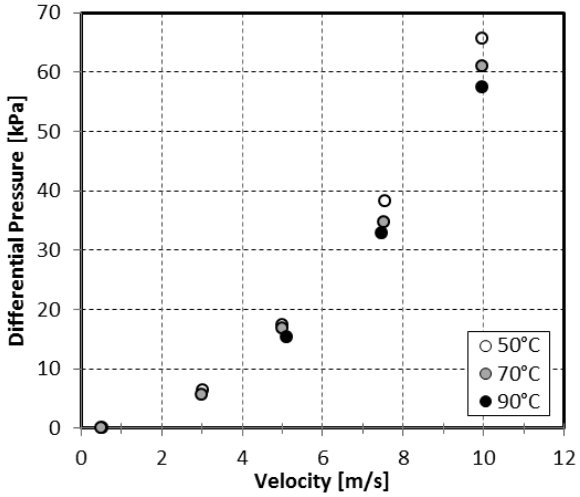

Figure 13: Differential pressure drop across the nozzle plotted versus the jet velocity

Figure 13 plots the pressure drop across the nozzle versus the jet velocity at the three fluid temperatures tested. This nozzle was utilized for all experiments presented in this study. The trend seen in Figure 13 illustrates that the pressure drop increases as the velocity/flow rate increases. This result aligns with accepted theories in fundamental fluid dynamics. The pressure drop is also seen to decrease for increasing inlet temperatures at the same nozzle velocity. This effect is associated with lower ATF viscosities at higher temperatures, which results in the observed decrease in pressure drop.

Conclusions and Future Directions

Experiments were conducted to measure the heat transfer coefficients of impinging ATF (Mercon LV) jets. Jet impingement cooling of motor windings was simulated by fabricating various test samples with wire-bundle features on the impingement surface. The effects of fluid jet velocity and temperature on thermal performance were evaluated. The major conclusions for this study are summarized below.

- For the baseline/smooth test sample, increasing the jet velocity increased heat transfer coefficients. Fluid temperature was found to have negligible effect on heat transfer coefficients for the baseline flat target surface.
- The wire-bundle features on test samples (18 AWG, 22 AWG, and 26 AWG) had minimal effect on heat transfer coefficients at the lowest jet velocity tested (0.5 m/s). At this low velocity, all three test samples yielded nearly identical results that were similar to the results for the baseline sample. At higher jet velocities, the 18 AWG and 22 AWG samples, for the most part, provided heat transfer values greater than those of the baseline sample. The performance of the 26 AWG sample mirrored that of the baseline sample at all temperatures and jet velocities.
- Fluid splattering/deflecting off the impingement surface was observed to occur on the 18 AWG, 22 AWG, and 26 AWG samples at higher jet velocities (≥ 7.5 m/s). This effect reduced the fluid available for heat removal and thus reduced heat transfer coefficients. This phenomenon was more pronounced with the two samples that had the larger surface features (i.e., 18 AWG and 22 AWG).
- The pressure drop across the nozzle was found to decrease with increasing fluid temperatures. This effect is associated with lower ATF viscosities at higher temperatures. Lower pressure drop implies lower parasitic power losses.
- The results presented in this study are intended to increase the amount of publicly available information on the thermal performance of ATF jet impingement cooling. The data may be used in designing ATF-jet-impingement-based motor cooling systems.

Future work is planned to further evaluate the forced convection heat transfer of automatic transmission fluids. A new project for FY14 is planned to focus on expanding this work in relation to convective cooling of electric motors with ATF. Future work is summarized below.

- Measure or obtain the ATF properties at various temperatures and utilize this information along with the current experimental results to generate correlations for ATF jet impingement cooling. The correlations can be used as a means to estimate the performance of ATF at various operating conditions (i.e., jet velocity and temperature).
- Utilize thermochromic liquid crystal technology and potentially infrared imaging to measure the spatial temperature variations on surfaces cooled by ATF impinging jets. Localized heat transfer coefficient information will allow us to map the heat transfer variation from the stagnation zone through the wall-jet region.

This report is available at no cost from the National Renewable Energy Laboratory (NREL) at www.nrel.gov/publications.

- Design and fabricate a larger test article that better simulates cooling of an electric motor. The test article may incorporate rotation to simulate the rotor. This is an effort to move toward more system-level research.
- Develop computational fluid dynamics models for the ATF impinging jet experiments and validate the model results with the available experimental data. This work will build confidence in modeling capabilities relative to ATF impinging jets, which will serve as a valuable guide for expanding confidence in larger-scale simulations with impinging jets on motor end windings.

FY 2013 Publications/Presentations

1. K. Bennion, J. Cousineau, J. Jeffers, C. King, M. Mihalic, and, G. Moreno, "Oil Cooling of Electric Motors – July 2013 Milestone Report," FY2013 DOE milestone report, July 2013.
2. K. Bennion, J. Cousineau, D. DeVoto, T. Jahns, S. McElhinney, M. Mihalic, and G. Moreno, "Electric Motor Thermal Management," 2013 DOE Vehicle Technologies Office (VTO) Annual Merit Review, Crystal City, VA, May 2013.
3. K. Bennion, J. Jeffers, and G. Moreno, "Electric Motor Thermal Management," Presentation to the DOE VTO Electrical and Electronics Technical Team, Southfield, MI, August 2013.
4. K. Bennion, J. Cousineau, D. DeVoto, T. Jahns, S. McElhinney, M. Mihalic, and G. Moreno, "Electric Motor Thermal Management," Advanced Power Electronics and Electric Motors FY13 Kickoff Meeting, DOE Vehicle Technologies Program, Oak Ridge, TN, November 2012.

Acknowledgments

The author would like to acknowledge the support provided by Susan Rogers and Steven Boyd, Technology Development Managers for Advanced Power Electronics and Electric Motors, VTO, U.S. Department of Energy Office of Energy Efficiency and Renewable Energy. The significant contributions of Justin Cousineau, Jana Jeffers, Charlie King, Mark Mihalic, and Gilbert Moreno (NREL) to the project are acknowledged.

References

1. K. Bennion and J. Cousineau, "Sensitivity Analysis of Traction Drive Motor Cooling," in IEEE Transportation Electrification Conference and Expo (ITEC), 2012, pp. 1 –6.
2. J. R. Hendershot and T. J. E. Miller, *Design of Brushless Permanent-Magnet Motors*. Magna Physics Pub., 1994.
3. U.S. DRIVE, "Electrical and Electronics Technical Team Roadmap," Partnership Plan, Roadmaps, and Other Documents, June 2013. [Online]. Available: http://www1.eere.energy.gov/vehiclesandfuels/pdfs/program/eett_roadmap_june2013.pdf. [Accessed: September 10, 2013].
4. Burress, T. A.; Coomer, C. L.; Campbell, S. L.; Wereszczak, A. A.; Cunningham, J. P.; Marlino, L. D.; Seiber, L. E.; Lin, H. T. *Evaluation of the 2008 Lexus LS 600H Hybrid Synergy Drive System*. Technical Report No. ORM-2008/185. Oak Ridge, TN: Oak Ridge National Laboratory, 2009.

This report is available at no cost from the National Renewable Energy Laboratory (NREL) at www.nrel.gov/publications.

Combining Fluid Loops on Electric-Drive Vehicles

Principal Investigator: John Rugh
National Renewable Energy Laboratory (NREL)
Transportation and Hydrogen Systems Center
15013 Denver West Parkway
Golden, CO 80401
Phone: 303-275-4413
E-mail: John.Rugh@nrel.gov

DOE Technology Development Manager: Susan A. Rogers
Phone: 202-586-8997
E-mail: Susan.Rogers@ee.doe.gov

NREL Task Leader: Sreekant Narumanchi
Phone: 303-275-4062

Start Date: FY 2011
Projected End Date: FY 2014

Objectives

- Improve vehicle range and reduce cost from combining thermal management systems
- Collaborate with industry partners to research the synergistic benefits of combining thermal management systems in vehicles with electric powertrains

Technical Barriers

Electric-drive vehicles (EDVs) have increased vehicle thermal management complexity. They introduce new requirements for thermal management of the energy storage system (ESS) as well as power electronics and electric motor (PEEM), including increased costs for separate cooling loops and increased energy consumption to meet thermal demands. The energy consumption increase is particularly critical for battery electric vehicles (BEVs), where it leads to decreased vehicle range and therefore user "range anxiety," which decreases market acceptance.

Technical Targets

- PEEM coolant loop with temperatures less than 105°C without requiring a dedicated system
- Maximize the usage of waste heat from the PEEM and ESS components and enable heat pump operation
- Reduce aerodynamic drag by minimizing the area and number of heat exchangers in the front end of the vehicle
- Reduce overall energy consumption for vehicle thermal systems and improve range

Accomplishments

- An experimental combined fluid loop (CFL) system was constructed
  - Prototype heat exchangers provided by partner Delphi
  - A prototype automotive electric compressor was provided by partner Halla Visteon Climate Control
- A test apparatus was constructed to simulate load, control, and measure the performance of the CFL system
  - The experiment can be operated in a variety of different test configurations over a range of vehicle operating conditions from very cold to very hot

Introduction

Plug-in hybrid electric vehicles and BEVs have increased vehicle thermal management complexity (e.g., PEEM, ESS, and vehicle cabin). Multiple cooling loops may lead to reduced effectiveness of fuel-saving control strategies. The additional cooling loops increase weight, volume, aerodynamic drag, and fan/pump power, thus reducing electric range. This reduces customer acceptance of BEVs by increasing range anxiety and presents a barrier for the penetration of BEVs into the national vehicle fleet. Our goal is to improve vehicle performance (fuel use or BEV range) and reduce cost by capturing the synergistic benefits of combining thermal management systems. The overall goal is to solve vehicle-level heat transfer problems, which will enable acceptance of vehicles with electric powertrains.

The objective of this project is to research the synergistic benefits of combining thermal management systems in vehicles with electric powertrains. Currently, EDVs typically have a separate cooling loop for the PEEM components. It would be beneficial to have a PEEM coolant loop with temperatures less than 105°C without requiring a dedicated system. Range would be increased in the winter by minimizing electrical resistance heating through a combined thermal management system that maximizes the usage of waste heat from the PEEM and ESS components and enables heat pump operation. With increased focus on aerodynamics, minimizing the area and number of heat exchangers in the front end of the vehicle has the potential to reduce drag. An additional benefit of combining cooling loops is that the ESS, passenger compartment, and thermal management fluid loops can be preconditioned.

In the first year of the project (FY 2011), Halla Visteon Climate Control, a Tier 1 automotive heating, ventilation and air conditioning (HVAC) component supplier, supplied detailed thermal component and system information. This included drawings, thermal and flow component data, and system performance data. The NREL researchers built component models in KULI [1] using the geometry, heat transfer, and pressure drop information. The individual component models were verified to function as expected. Cabin thermal, air conditioner (A/C), and PEEM cooling loop models were then developed by combining the individual component models into systems, which were then compared to test data.

This report is available at no cost from the National Renewable Energy Laboratory (NREL) at www.nrel.gov/publications.

In the second year of the project (FY 2012), the individual thermal models of the cabin A/C, cabin heater, PEEM, and ESS fluid loops were improved based on the results from comparisons to test data. A baseline electric vehicle thermal system model was created from these sub-system models, and its performance was evaluated. The A/C system and ESS cooling loop controls were updated with more sophisticated models, and several CFL strategies were investigated. The CFL system modeling demonstrated that the design properly conditioned the ESS during heating and cooling, maintained cabin air comfort temperatures, lowered PEEM temperatures to enable higher power, and reduced heating energy through heat recovery [2].

Approach

The overall approach of the project is to demonstrate the feasibility and energy savings benefits of an integrated vehicle thermal management (IVTM) system through modeling with KULI software and experimental validation using a bench testing apparatus. Previously conducted KULI modeling work demonstrated that the IVTM system decreased energy consumption while reducing the number of system components and satisfying the thermal management requirements of the ESS, PEEM, and cabin. An experimental test system was designed and constructed to validate the KULI modeling results previously obtained, as well as further investigate both heating and cooling performance.

To perform the experimental study, a test apparatus capable of evaluating the steady-state and transient performance of an electric vehicle thermal system was constructed. The ultimate goal of the test apparatus is to measure the impact of the IVTM technology on EDV range. In order to demonstrate the effect on vehicle range, a variety of drive cycles will be simulated on the IVTM experimental hardware over a range of ambient air temperatures from -30°C to 43°C.

In addition to measuring the energy efficiency enhancement, the experiment will also investigate control strategies and system configurations. This information will then provide feedback and insight for manufacturers when selecting system designs for vehicle implementation. The expectation is that the results will lead to a future project in which a prototype system is installed into a test vehicle with a design based on the KULI modeling and experimental test bench findings.

Combined Fluid Loop Concept

The CFL concept is an experimental system design that is one possible configuration for an IVTM system. The goal of the CFL design is to provide a platform through which a variety of IVTM operation modes can be tested. Choosing the best IVTM system configuration for a given vehicle will involve making tradeoffs between cost and capability or, in other words, complexity and energy savings. The CFL concept is designed to investigate a number of the possible system configurations in order to quantify their performance. As such, the experimental CFL design is more complex than would be expected for most vehicle applications.

The CFL concept that was developed for bench testing is intended to allow operation of the system with a variety of control strategies under a wide range of operating conditions. The system loads will be representative of a typical passenger BEV. In addition to cooling the cabin in A/C mode, it also enables waste heat recovery from the PEEM and ESS when beneficial, ambient cooling of the PEEM and ESS when possible, active cooling of the ESS as required, and heat pump operation.

In this CFL design, a “secondary loop” configuration is used, in which the vapor compression cycle transfers heat between the R134a refrigerant and the 50%/50% by mass water/ethylene glycol (WEG) liquid coolant mixture. This is accomplished through the use of aluminum brazed plate-type heat exchangers as the condenser and evaporator/chiller. One of the biggest advantages of this design is that it is more compact than the typical automotive design, which uses refrigerant-to-air heat exchangers at the front of the vehicle and within the vehicle console HVAC unit. This also eliminates the necessity for long lengths of permeable hose, reducing refrigerant leakage.

A basic component-level schematic of the CFL system is shown in Figure 1. The five three-way valves with “S” controllers represent solenoid valves capable of switching the flow between two ports. The two two-way valves with “S” controllers represent simple on/off solenoid valves. The three three-way valves with “Var.” controllers represent variable proportioning valves that can modulate the degree of heat exchanger flow bypass. The “PTC Heater” represents a supplementary positive temperature coefficient (PTC) electrical resistance heater.

For the experimental system being tested, Delphi has provided prototype heat exchangers from its “Unitary Heat Pump-A/C” system, as shown in Figure 2. In addition to the condenser and chiller heat exchangers shown, they have also supplied WEG-to-air heat exchangers for the low-temperature front-end heat exchanger (FEHX), cabin heater core, and cabin cooler core, as represented in Figure 1. These heat exchangers are designed to deliver the heating and cooling capacities necessary for a small to mid-size BEV.

This report is available at no cost from the National Renewable Energy Laboratory (NREL) at www.nrel.gov/publications.

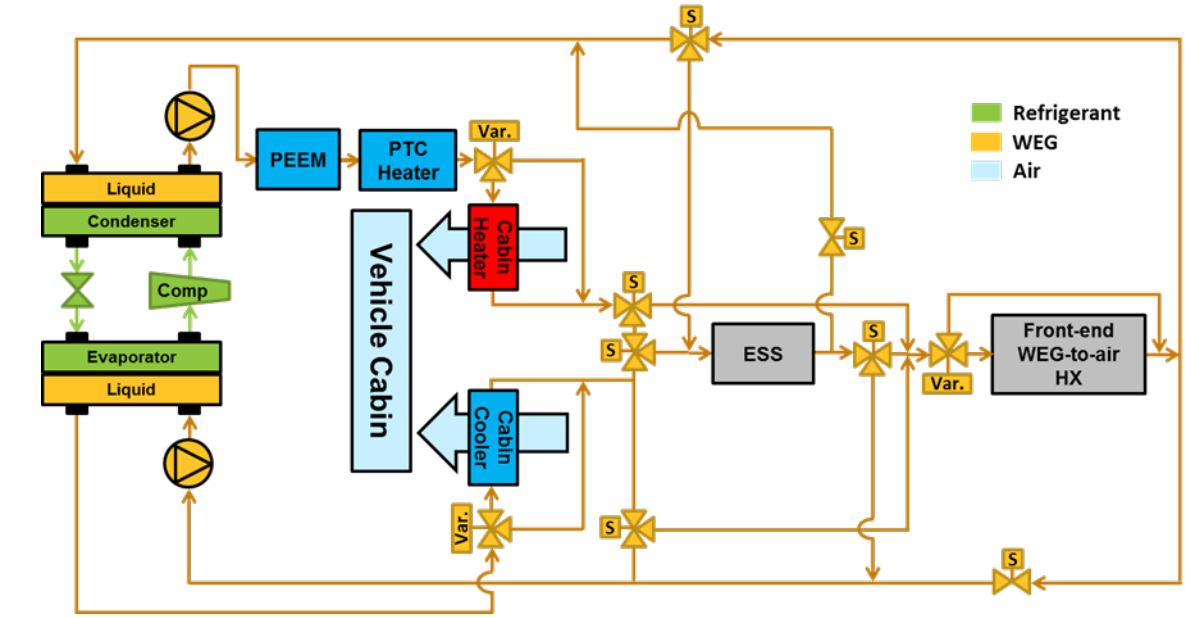

Figure 1. Combined fluid loop concept schematic

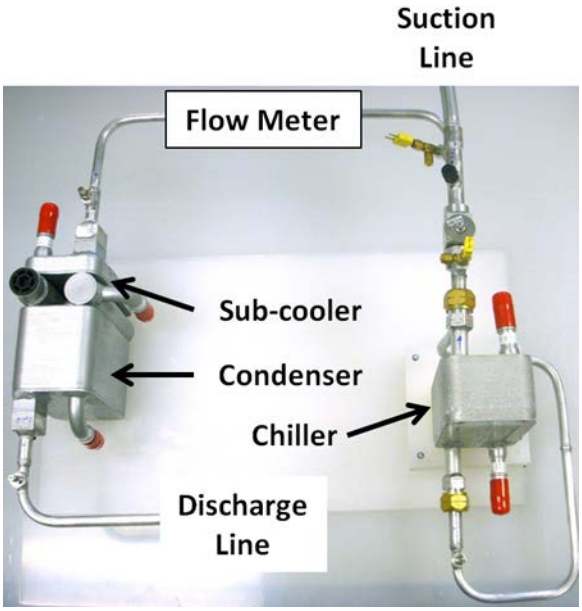

Figure 2: Prototype Delphi "Unitary HPAC" system

To complete the vapor compression cycle system, a compressor is needed. To most accurately reflect the performance in a passenger BEV, an automotive electric compressor is used instead of the more traditional automotive belt-driven compressor. The compressor was provided by Halla Visteon Climate Control and is shown in Figure 3. The compressor is a prototype unit that is designed to operate over a wider range of conditions than a typical automotive A/C compressor. The ability to handle extended conditions is necessary for the lower suction pressures and higher pressure ratios inherent to heat pump operation.

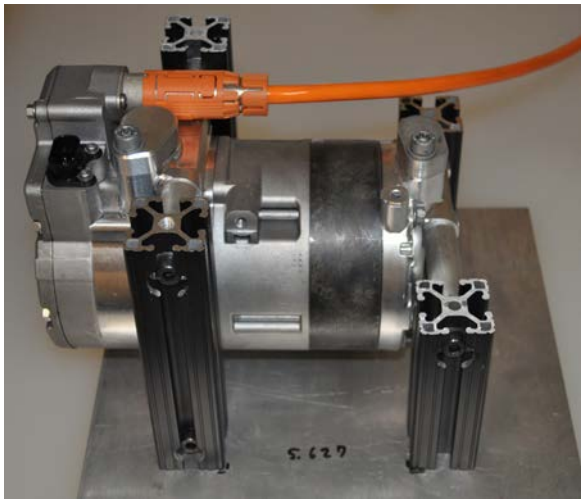

Figure 3: Halla Visteon Climate Control "E-comp" electric compressor

Test Apparatus

A test apparatus was constructed in order to subject the experimental CFL system to realistic loads and measure the resulting performance. The test apparatus consists of two air loops that are designed to condition and measure the air temperatures and flow rates to the air-side heat exchangers of the experimental CFL system. A basic schematic of the test apparatus is shown in Figure 4, and a picture of the completed assembly is shown in Figure 5.

This report is available at no cost from the National Renewable Energy Laboratory (NREL) at www.nrel.gov/publications.

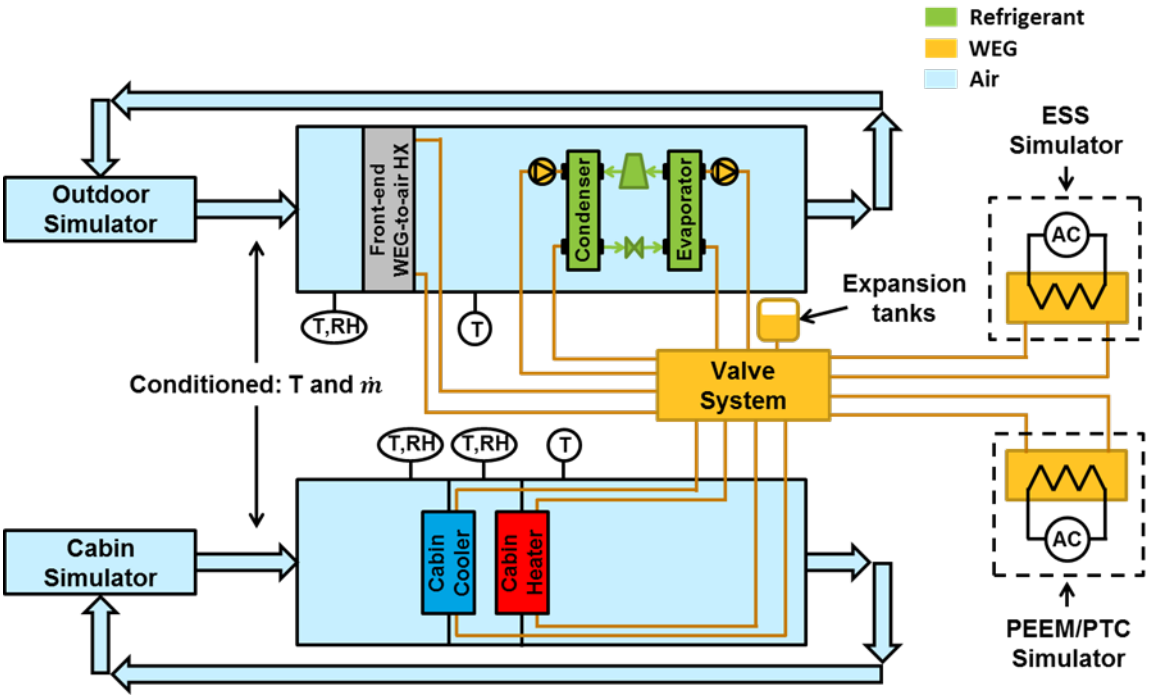

Figure 4: Basic overview of bench test apparatus design

The larger air duct delivers a constant air temperature and variable air flow rate to the FEHX to simulate the outdoor ambient air passing over the front of the vehicle. The smaller air duct delivers a variable air temperature and air flow rate to the cooler core and heater core heat exchangers to simulate the cabin recirculation temperature. The test apparatus also employs two electrical resistance heaters to simulate the PEEM/PTC and ESS heat loads on the experimental CFL WEG system.

Figure 5: Constructed bench test apparatus

All of the controlled parameters of the test apparatus are designed to simulate steady-state and transient vehicle operation. Without an environmental chamber housing the test apparatus, it is capable of operating at test conditions from the ambient room temperature, up to a 43°C outdoor temperature and a 63°C cabin soak temperature. The test apparatus is built on wheels so that it can be moved into an environmental control chamber for low temperature testing. When housed in a low-temperature environmental chamber, the range is extended down to -30°C for both the outdoor and cabin soak temperatures. The intention is that the experimental testing will simulate conditions of operating a vehicle in ambient outdoor conditions from -30°C to 43°C for both city and highway driving.

The instrumented measurement equipment of the test apparatus and CFL system include relative humidity sensors, air flow venturis, barometric air pressure sensors, air-side thermocouples, WEG flow rate Coriolis meters, WEG thermocouples, refrigerant turbine flow meter, refrigerant thermocouples, and refrigerant pressure transducers. The accuracies of the selected sensors were chosen to maintain propagated uncertainties for the key experimental parameters under 5%. This includes measurements such as flow rates, cooling and heating capacities, and coefficient of performance (COP). The thermocouples were calibrated to obtain accuracies better than 0.3°C.

To put realistic loads on the CFL system, LabVIEW [3] data acquisition and control code was written to simulate the loads and thermal responses of a BEV. Controls integrated into the LabVIEW code will modify the test apparatus hardware outputs as necessary to maintain the operational conditions specified by the software models. The mathematical models from NREL's Future Automotive Systems Technology Simulator (FASTSim) [4] vehicle simulation software were written into the LabVIEW code to calculate the simulated vehicle's propulsion loads based on

This report is available at no cost from the National Renewable Energy Laboratory (NREL) at www.nrel.gov/publications.

the selected drive cycle profile. The FASTSim models provide the waste heat outputs from the PEEM and ESS.

To calculate the expected thermal response of the PEEM and ESS components and their interaction with the CFL WEG system, the heat transfer models created for the KULI model [2] were written into the LabVIEW software. These models interact with the measured performance of the experimental CFL WEG system, i.e., inlet WEG temperatures, such that the temperatures of the simulated components can be calculated. Additionally, a heat transfer model was created for the vehicle cabin to predict the air and interior mass temperatures, including the temperature of the recirculation air of the HVAC unit. The cabin model is a transient, physics-based model developed by Gado [5]. The temperatures calculated by the ESS, PEEM, and cabin thermal models are particularly important as performance metrics because the CFL system must be able to maintain the ESS and PEEM temperatures within specific ranges to maximize performance and reliability, and the cabin temperatures can be used to predict passenger comfort.

Results

Initial testing of the CFL concept in the test apparatus is in progress.

Conclusions and Future Directions

An experimental CFL system was constructed using prototype heat exchangers from Delphi and a prototype automotive electric compressor from Halla Visteon Climate Control. The system is designed to be operated in a variety of different test configurations over a range of operating conditions from very cold to very hot. The CFL system enables cabin A/C, PEEM and ESS waste heat recovery, ambient cooling of the PEEM and ESS, active cooling of the ESS, and heat pump operation.

A mobile test apparatus was constructed to load, control, and measure the performance of the CFL system for a BEV. Mathematical models were integrated into the data acquisition and control system to simulate ESS, PEEM, and cabin loads due to propulsion and ambient conditions, as well as their thermal responses. The test apparatus imposes these transient loads on the CFL system via hardware in order to measure the energy consumption of the IVTM system. The measured energy consumption will then be used to estimate the improvement in vehicle range.

FY 2013 Publications/Presentations

1. Rugh, J. P., and Bennion, K., (2012) “Electric Vehicle Thermal Modeling to Assess Combined Cooling Loop Concepts,” Proceedings of the SAE Thermal Management Systems Symposium, October 31–November 1, 2012, Scottsdale, AZ.

Acknowledgments

The author would like to acknowledge the support provided by Susan Rogers and Steven Boyd, Technology Development Managers for Advanced Power Electronics and Electric Motors, Vehicle Technologies Office (VTO), U.S. Department of Energy (DOE) Office of Energy Efficiency and Renewable Energy as well as Lee Slezak and David Anderson of the U.S. DOE VTO. The contributions of Daniel Leighton, Jeff Tomerlin, and Cory Kreutzer (NREL) to the project are acknowledged as are those from Carrie Kowsky and Tim Craig of Delphi, and John Meyer and Tim VanBritson of Halla Visteon Climate Control.

References

1. “KULI: Overview.” [Online]. Available at http://kuli.ecs.steyr.com/ . Accessed: 18-Sep-2013.
2. Rugh, J. P., and Bennion, K., *Electric Vehicle Thermal Modeling to Assess Combined Cooling Loop Concepts.* SAE 2012 Thermal Management Systems Symposium, October 2012.
3. “LabVIEW: System Design Software.” Available at http://www.ni.com/labview/ . Accessed: 18-Sep-2013.
4. “NREL: Vehicle Systems Analysis – Future Automotive Systems Technology Simulator.” Available at http://www.nrel.gov/vehiclesandfuels/vsa/fastsim.html . Accessed: 18-Sep-2013.
5. Gado, A., *Development of a Dynamic Test Facility for Environmental Control Systems*. University of Maryland Ph.D. Dissertation, 2006.

This report is available at no cost from the National Renewable Energy Laboratory (NREL) at www.nrel.gov/publications.

Reliability of Bonded Interfaces

Principal Investigator: Douglas DeVoto
National Renewable Energy Laboratory (NREL)
Transportation and Hydrogen Systems Center
15013 Denver West Parkway
Golden, CO 80401
Phone: 303-275-4256
E-mail: Douglas.Devoto@nrel.gov

DOE Technology Development Manager: Susan A. Rogers
Phone: 202-586-8997
E-mail: Susan.Rogers@ee.doe.gov

NREL Task Leader: Sreekant Narumanchi
Phone: 303-275-4062

Start Date: FY10
Projected End Date: FY13

Objectives

- Investigate and improve the thermal performance and reliability of emerging bonded interface materials for power electronics packaging applications.
- Identify failure modes in emerging bonded interface materials, experimentally characterize their lives under known conditions, and develop lifetime estimation models.

Technical Barriers

In automotive power electronics packages, conventional thermal interface materials such as greases, gels, and phase-change materials pose bottlenecks to heat removal and are also associated with reliability concerns. The industry trend is toward high thermal performance bonded interfaces. However, because of coefficient of thermal expansion mismatches between materials/layers and resultant thermomechanical stresses, adhesive and cohesive fractures could occur, posing a reliability problem. These defects manifest themselves in increased thermal resistance.

Technical Targets

Improved package reliability is an enabler to achieve the U.S. Department of Energy (DOE) Advanced Power Electronics and Electric Motors (APEEM) Program power electronics targets for improved efficiency, performance, and lifetime.

Accomplishments

We present results for thermal performance and reliability of bonded interfaces based on thermoplastic (polyamide) adhesive, with embedded near-vertical aligned carbon fibers, as well as sintered silver material. The results for these two materials are compared to conventional lead-based ($Sn_{63}Pb_{37}$) bonded interfaces. These materials were bonded between 50.8-mm × 50.8-mm cross-sectional footprint silicon nitride substrates and Cu base plate samples. Samples of the substrate/base plate bonded assembly underwent thermal cycling from –40°C to 150°C according to Joint Electron Devices Engineering Council standard Number 22-A104D for up to 2,500 cycles. The dwell time of the cycle was 10 minutes, and the ramp rate was 5°C/minute. Damage was monitored every 100 cycles by acoustic microscopy as an indicator of an increase in thermal resistance of the interface layer. The acoustic microscopic images of the bonded interfaces after 2,500 thermal cycles showed that thermoplastics with embedded carbon fibers performed quite well with no defects, whereas interface delamination occurred in the case of the sintered silver material. Both these materials showed a superior bond quality compared to the $Sn_{63}Pb_{37}$ solder interface after 1,500 thermal cycles. The delamination percentage was calculated and compared between the three interface materials. Strain energy density values of $Sn_{63}Pb_{37}$ solder were obtained as an output from ANSYS simulations for lifetime estimation of the interface material.

✧ ✧ ✧ ✧ ✧

Introduction

In a power electronics module, a semiconductor chip/die is typically attached by a bonded interface material (BIM) such as solder to a metalized substrate. The substrate is composed of a ceramic bounded by Cu layers on either side and provides electrical isolation. This substrate is then mounted onto a base plate or directly to a heat exchanger, typically made of Cu or Al, via another BIM. A cross-section of a typical power electronics package is shown in Figure 1.

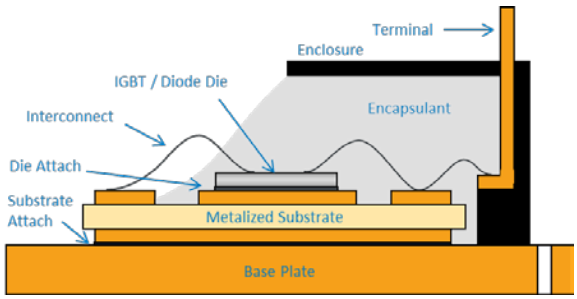

Figure 1: Traditional power electronics package

A coefficient of thermal expansion (CTE) mismatch between the ceramic substrate and the Cu base plate can cause defect initiation and propagation in the joining solder layer. Lead-based solders had predominantly been used in the electronics packaging industry; however, the Restriction of Hazardous Substances Directive [1] mandated lead-free solutions. Initially, the industry focused on various Sn, Ag, and Cu (SAC) compositions as a suitable lead-free alternative, with Innolot ($SnAg_{3.8}Cu_{0.7}Bi_{3.0}Sb_{1.4}Ni_{0.2}$) proving to be a promising solution [2–3]. Research found that varying the composition of the Ag and Cu content in the SAC solders would help minimize creep strain. Overall, reliability under temperature cycling continues to be a concern with lead-free

This report is available at no cost from the National Renewable Energy Laboratory (NREL) at www.nrel.gov/publications.

solders. To provide greater thermomechanical reliability under temperature cycling and to allow for higher temperature applications, sintered silver material has also emerged as a promising bonding solution in power electronics packages [4–5]. However, to reduce synthesis temperatures to below 300°C, up to 40 MPa of pressure must be applied to the package, causing a higher complexity in the production process and more stringent flatness specifications for the substrates. Hence, alternative bonding techniques are being developed to increase the thermomechanical reliability of this interface through the use of newer materials, such as thermoplastics with embedded micrometer-sized carbon fibers. Little information is available on the thermal performance and reliability of large-area attaches based on the more recently developed thermoplastic materials.

Prior work at the National Renewable Energy Laboratory (NREL) [6–7] focused on establishing a consistent and high-accuracy database, via the American Society for Testing and Materials steady-state approach [8], on the thermal performance of conventional as well as emerging thermal interface materials (TIMs). The conventional materials included greases, gels, phase-change materials, and filler pads. It was concluded that the tested conventional materials could not meet the thermal performance target of 5-mm^{2}K/W thermal resistance for a 100-µm bond line thickness. For a number of power electronics packaging stack-ups, the TIM stops being a bottleneck to heat removal when its resistance is on the order of 5 mm^{2}K/W; thus, it is a target. In addition, practical power electronics packaging configurations and manufacturing constraints dictate that the TIM has to fill gaps on the order of 100 µm.

Because BIMs are promising [9–13], work at NREL has focused on assessing their thermal performance and reliability. Conclusions on thermal performance and reliability from the present effort are intended to directly assist incorporation of these materials into automotive power electronics designs. This report focuses on thermoplastic (polyamide) adhesive with embedded near-vertical–aligned carbon fibers (8- to 10-µm diameter), sintered silver based on micrometer-sized Ag particles, and $Sn_{63}Pb_{37}$ solder as a baseline. The sample synthesis, characterization plan, and results are described below.

Approach

Materials and Sample Synthesis

The assembly consists of a 5-mm-thick Cu base plate attached to a 0.72-mm-thick active metal bonded substrate (0.32-mm-thick silicon nitride [Si_3N_4] with 0.2-mm-thick Cu foil on either side of Si_3N_4, 50.8 mm × 50.8 mm cross-sectional area footprint) via the bonding material. Before assembly, the Cu metallization layers in the substrate were plated with 4 µm of electroless Ni-P, 1 µm of Pd, and 0.3 µm of Ag to improve adhesion with the bonding material. The Cu base plate was electroplated with 5 µm of Ag. An assembled sample is shown in Figure 2.

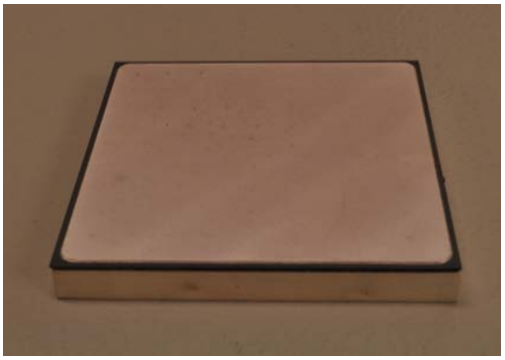

Figure 2: Representative metalized substrate/base plate assembly

A tabletop hot press was developed for synthesizing test samples requiring both temperature and pressure bonding parameters. Two hot plates were positioned, one on either side of the sample to be bonded, and were embedded with five 250-W cartridge heaters. Three heaters were inserted in the top hot plate and two in the bottom hot plate. A temperature controller adjusted the power of the heaters based on the temperature measurement by a thermocouple located in the bottom hot plate. The test sample and hot plates were placed between layers of mica and cold plates, and then inserted into an arbor press [14]. Glycol-water (50%–50% mixture by volume) coolant was circulated within the cold plates to isolate the high bonding temperatures from the hydraulic piston and the fluid. A screw jack was also placed between the hydraulic piston and top cold plate to provide fine adjustment to the applied bonding pressure. The pressure of the hydraulic fluid was electronically monitored to determine the force applied to the sample under bonding.

The HM-2 material, manufactured by Btech Corporation, is a composite structure consisting of 8- to 10-µm-diameter carbon fibers embedded in a polyamide/thermoplastic adhesive at approximately 40% fill factor by volume. The HM-2 was placed between the substrate/base plate assembly and subjected to a pressure of 689.5 kPa and a temperature of 190°C. Once the temperature was reached, the assembly was allowed to cool to room temperature while the pressure was maintained.

Bonded interfaces based on sintered silver particles were synthesized by Semikron. Corners of the Si_3N_4 substrate were rounded off to match the 2-mm radius of the Cu layers. The sample assembly was placed in a hot press and raised to its processing temperature, after which pressure was applied.

As a baseline, a $Sn_{63}Pb_{37}$ bond was also synthesized between the substrate/base plate assembly. A 127-µm-thick stainless steel stencil with 9-mm × 9-mm square openings and 1-mm separation was used to apply solder evenly to the substrate and base plate surfaces. After the solder was applied, the assembled sample was placed in a vacuum solder reflow oven. The reflow profile ensured that flux was removed from the bond and that voiding remained less than 2%.

Initial BIM Characterization

Degradation (e.g., cracks, voids, and delaminations) of the bonded interface can be non-destructively detected by

This report is available at no cost from the National Renewable Energy Laboratory (NREL) at www.nrel.gov/publications.

acoustic microscopy. After defect initiation, the thermal and electrical performance of the sample assembly degrades. A C-mode acoustic microscope (C-SAM) emits ultrasound waves with frequencies ranging from 5 MHz to 400 MHz into a sample suspended in water. The strength of the signal reflected back to the microscope's transducer from an interface within a sample depends on the relationship between the acoustic impedances of the two materials forming the interface. A crack, void, or delamination will create a solid-to-air interface, which will cause a strong reflection to be detected by the microscope's transducer. Samples were measured for their initial bonding condition and then subsequently tested every 100 thermal cycles. Images showing the bonded interface within samples before accelerated thermal testing are shown in Figure 3. The circular bands visible in each sample are artifacts of the C-SAM representing top surface curvatures as 2-D images and are not indicators of bond quality. The $Sn_{63}Pb_{37}$ solder, Btech HM-2, and sintered silver all exhibited uniform bonds between the base plate and substrate samples.

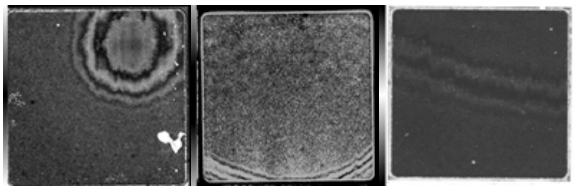

Figure 3: C-SAM images showing initial bond quality in $Sn_{63}Pb_{37}$ solder (left), sintered silver (center), and Btech HM-2 (right) (Photo credit: Doug DeVoto, NREL)

In addition to acoustic microscopy, the electrical resistance of the Si_3N_4 insulation layer was measured. In a high potential (hipot) test, a high voltage is applied to an electronic device's current-carrying components. The quality of the insulation in the device is determined by measuring the presence of a leakage current. Leakage current indicates that dielectric breakdown in the insulation layer has occurred [15]. A dielectric resistance tester was previously constructed based on the hipot testing process to detect when a crack in the Si_3N_4 has developed. A custom fixture contacts the top and bottom sides of a test sample, and a test voltage of 2.0 kV is applied for 20 seconds, which is sufficient voltage to cause an arc in the air through a defect or crack in the 0.32-mm-thick Si_3N_4 layer. Measurement of the leakage current from an arc indicates that damage occurred within the Si_3N_4 layer in the sample. The sample successfully passes the test if no current was measured over the analysis period. The results correlated with acoustic microscopy images, indicating that all initial samples exhibited no defects within the Si_3N_4 layer.

CTE mismatches within the samples cause package deformation and stresses to build up in the Si_3N_4 layer during the cooldown from the synthesis temperature to room temperature. These stresses can be sufficient to cause crack initiation and propagation within the Si_3N_4, leading to failure of the layer's electrical insulating properties. Representative CTE parameters for materials common within a power electronics package and examples of package deformation conditions are shown in Figure 4. As a package cools from a stress-free temperature, the Cu base plate's higher CTE relative to the substrate and silicon die causes it to contract more and induce a bow into the package. Heating will conversely cause the base plate to expand more quickly than the rest of the package and create a bow in the opposite direction.

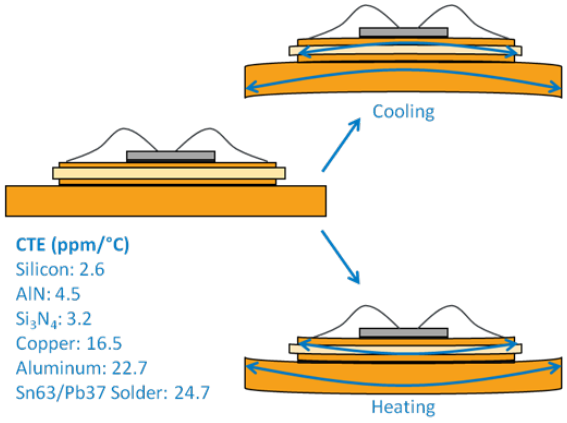

Figure 4: Power electronics package deformation caused by CTE mismatch under cooling and heating conditions

The high pressure and temperature synthesis requirements for sintered silver did not cause crack initiation within the Si_3N_4 substrate; however, package deformation was evident when samples were at room temperature. A laser profilometer was used to scan the top and bottom surfaces of sintered silver samples for accurate measurements of these deformations. Figure 5 shows the top surface profile of one sintered silver sample as well as a cross-section profile between two of the sample's corners. The height variation across the sample was measured to be 166 µm. Surface profile measurements were also taken for $Sn_{63}Pb_{37}$ solder and thermoplastic samples, but no significant package deformations were found.

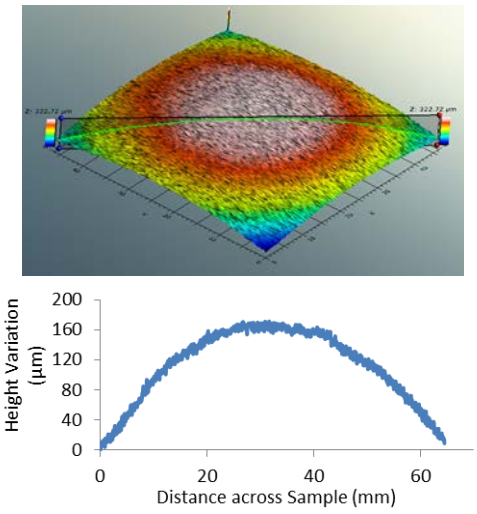

Figure 5: Surface profile of sintered silver sample at room temperature

Modeling of Strain Energy Density in $Sn_{63}Pb_{37}$ Solder

The BIM reliability modeling approach involves first calculating the accumulated viscoplastic strain energy density per cycle using finite element analysis. Results are then implemented into a fatigue model to obtain a correlation of the

This report is available at no cost from the National Renewable Energy Laboratory (NREL) at www.nrel.gov/publications.

strain energy density with experimentally determined number of thermal cycles to BIM failure. ANSYS Mechanical was selected for the finite element analysis because of its established accuracy in this field [16–20].

An ANSYS Parametric Design Language (APDL) code was developed that included model pre-processing, solver, and post-processing stages. The model geometry matched the experimental test sample geometry and consisted of a stackup of 50.8-mm × 50.8-mm cross-sectional area footprint composed of a Cu base plate, $Sn_{63}Pb_{37}$ solder BIM, and a Si_3N_4 substrate. A quarter symmetry of the package was utilized in the modeling to save computational space and time, shown in Figure 6.

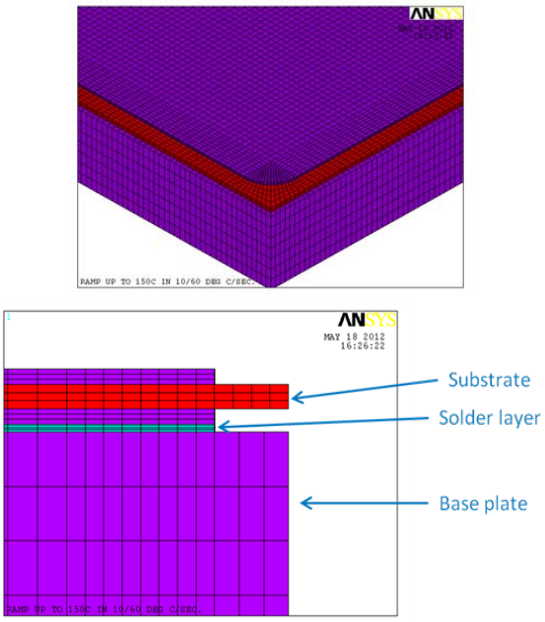

Figure 6: Quarter symmetry model (top) and layers in the bonded assembly (bottom)

After the geometry was constructed, material properties were assigned to the various layers within the package. The Anand constitutive model was used to define the viscoplastic nature of the solder interface while temperature-dependent, elastic properties were applied to the base plate and substrate layers [21–22]. Nine parameters in the Anand model were obtained from published literature. Various mesh controls, including element sizing, edge sizing, and meshing technique, were then used to create a structured mesh that increased in density at the bonded interface layer. Furthermore, these controls ensured that no mesh mismatch occurred between the model layers. The model was then subjected to a cyclic temperature load with maximum and minimum temperatures of 150°C and –40°C, respectively, a ramp rate of 5°C/min, and a dwell time of 10 minutes. Four such cycles were simulated to study the plastic behavior of the solder interface.

The package design was modified to create a fillet at the corner region to reduce the maximum strain energy distribution. The fillet was created both for the solder layer and for the Cu metallization layers in the substrate. The geometry construction and the meshing sections of the APDL code were significantly modified to incorporate the fillet at the corner region. Separate control over the mesh in the fillet region was achieved in the modified code. This was important for minimizing computational time and mesh size, as mesh density could then be increased in the solder fillet region independently of the solder inner region. An appropriate element size was chosen after conducting a mesh independence study to achieve a balance between computational time and accuracy of the results. Model variations with a fillet radius of 1.5 mm and 2 mm were analyzed as the application of a fillet onto a substrate's metalized layers is a common technique to increase the reliability of the solder layer in the corner region.

Results

BIM Condition after Thermal Cycling

After initial characterization of the test samples, conditions must be applied to create thermally induced stresses, leading to cracking, voiding, or delamination failures. Generally, three types of thermal duty cycles can be used to create thermally induced stresses: a temperature cycle, a thermal shock cycle, and a power cycle. A temperature cycle specifies the temperatures to which a sample under test will be exposed, the durations of exposure, and the rate of temperature change when the sample under test is brought to a new temperature set point. A thermal shock cycle is similar to a temperature cycle, but consists of rapid changes in the ambient temperature. Finally, a power cycle is created by heat dissipation in an actual electronic device to create realistic heat flow patterns and temperature distributions in a sample under test. Because the lifetimes of samples are too long to be tested in real time, an accelerated temperature cycling test procedure is employed to bring testing times down to a reasonable duration.

Samples were cycled between –40°C and 150°C, a common temperature range for electronics testing, to evaluate the quality of the bonded interfaces [23–26]. A soak, or dwell, time of 10 minutes at the maximum and minimum temperatures was chosen to promote solder fatigue and creep [23]. Ramp rates for thermal cycling must be sufficiently low to avoid transient thermal gradients in the test samples; therefore, ramp rates were in the 5°C/min range. Each sample was cycled up to 2,500 thermal cycles, or until degradation propagated to sufficient levels to separate the substrate from the base plate. A failure is defined as a crack in the Si_3N_4 substrate, a cohesive fracture within the BIM, or an adhesive/interfacial fracture between the BIM and either the substrate or base plate surface. A crack in the Si_3N_4 substrate would indicate loss of electrical insulation capabilities and the sample would immediately be considered failed. Cohesive or adhesive/interfacial fractures in the BIM would increase the thermal resistance of the power electronics package, eventually creating a thermal bottleneck that would elevate the operating temperature of a die above its maximum limit. For testing purposes, a fracture leading to 15% area delamination of the BIM is defined as a failure.

Thermoplastic HM-2 samples have undergone 2,500 temperature cycles and have shown no initiation of defects in

This report is available at no cost from the National Renewable Energy Laboratory (NREL) at www.nrel.gov/publications.

the Si_3N_4 substrate or the BIM. Figure 7 shows C-SAM images highlighting the corner regions of the Btech HM-2 interfaces after 1,000 temperature cycles, 1,500 cycles, and 2,500 cycles.

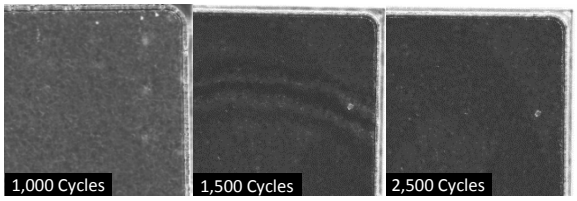

Figure 7: C-SAM images of Btech HM-2 thermoplastic material after select number of thermal cycles (Photo credit: Doug DeVoto and Paul Paret, NREL)

Sintered silver samples have also undergone 2,500 temperature cycles but have shown progressively increasing delamination of the BIM. This is observed in acoustic images of a corner region of the sintered silver material after 1,000 temperature cycles, 1,500 cycles, and 2,500 cycles, as shown in Figure 8.

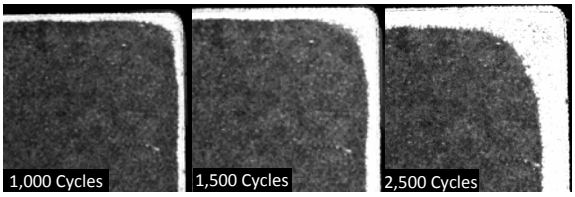

Figure 8: C-SAM images of sintered silver material after select number of thermal cycles (Photo credit: Doug DeVoto and Paul Paret, NREL)

Measurements of the delamination percentage within the sintered silver BIM were taken every 100 cycles from C-SAM imaging. Depending on the sample, this perimeter fracturing increased to 19%–32% of initial bonded area after undergoing 2,500 temperature cycles, as shown in Figure 9. Under these specific bonding and temperature cycling conditions, the sintered silver samples remained defect free until approximately 300 cycles. A period of transient rate delamination occurred after defect initiation until approximately 1,000 cycles, after which a constant rate delamination was observed to the conclusion of temperature cycling at 2,500 cycles.

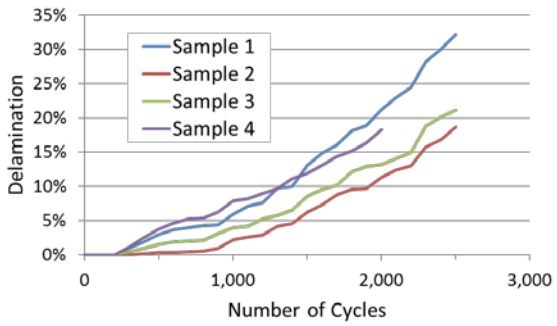

Figure 9: Perimeter delamination of sintered silver BIM as a function of number of thermal cycles

The fourth sample was cross-sectioned and the bonded interface layer was imaged after 2,000 temperature cycles. It was determined that the delamination observed in acoustic microscope images was the result of cohesive fracturing within the sintered silver material. The cohesive fracturing is shown in Figure 10. After 2,500 cycles, additional cross-sectioning and imaging confirmed that cohesive fracturing occurred in the remaining three sintered silver samples.

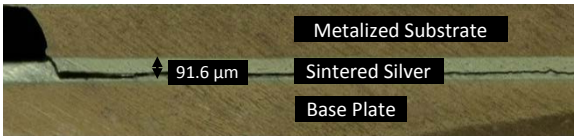

Figure 10: Cohesive fracture within sintered silver BIM after 2,000 temperature cycles

$Sn_{63}Pb_{37}$ solder samples have been subjected to 1,500 thermal cycles. C-SAM images show a higher amount of delamination, indicating a relatively poor performance of the BIM (Figure 11).

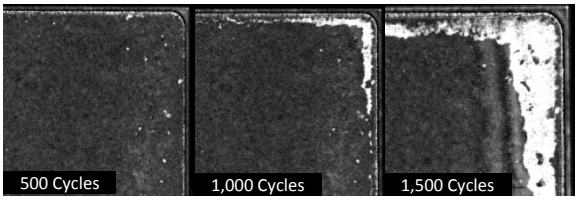

Figure 11: C-SAM images of $Sn_{63}Pb_{37}$ solder material after select number of thermal cycles (Photo credit: Doug DeVoto and Paul Paret, NREL)

The delamination percentage was calculated for the $Sn_{63}Pb_{37}$ solder material and compared with the other two interface materials. After 1,500 cycles, cohesive fracturing within the solder material reached 21%–24% delamination, and observed delamination rates were higher in the solder samples than in sintered silver or thermoplastic HM-2 samples. Delamination rates of all three interface materials are shown in Figure 12.

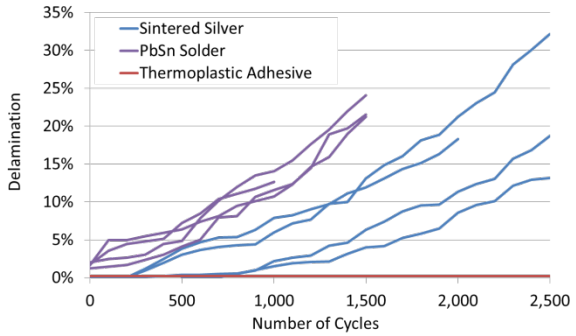

Figure 12: Perimeter delamination of sintered silver, $Sn_{63}Pb_{37}$ solder, and thermoplastic adhesive as a function of number of thermal cycles

Modeling Results

Figure 13 shows the temperature profile and development of shear strain and shear stress within the solder interface's corner region as a function of time. Calculations of strain levels within the solder interface are critical to develop relationships with fatigue failures within the interface material. As the temperature ramps up from room temperature to 150°C, strain within the solder develops and reaches a maximum value at the end of the elevated dwell period. During the subsequent ramp down, the strain decreases and reaches

This report is available at no cost from the National Renewable Energy Laboratory (NREL) at www.nrel.gov/publications.

the lowest level at the end of the low-dwell period. A similar pattern is also seen for shear stress, where the stress level first increases with temperature during the ramping up period. Stress relaxation is then observed during the last portion of ramping up and continues to relax through the elevated dwell period. Negative shear stress levels develop during ramp down and reach a minimum at the low dwell, where some stress relaxation is then observed. This model confirms that for $Sn_{63}Pb_{37}$ solder, creep effects accelerate at elevated temperatures.

Analysis of stress-strain hysteresis loops helps to understand the inelastic behavior exhibited by the interface and combines the effect of stress and strain into a single parameter: the strain energy density. On completion of a simulation, the node with the maximum equivalent strain was selected and its stress and strain values as a function of time were obtained through post-processing. Results indicated that the maximum strain energy distribution occurred at the solder's corner region, at the interfacial joint with the Cu base plate. The inelastic behavior of the solder joint under varying thermomechanical loads during a temperature cycle is illustrated in Figure 14. The temperature cycle is segmented into four different cases, a high dwell at 150°C, a ramp down to –40°C, a low dwell at –40°C, and then a ramp up back to 150°C. Beginning at the 150°C high dwell, shear stress slightly decreases as shear strain increases, with creep strain playing a predominant role. The ramp down segment causes both stress and strain values to decrease until the low dwell at –40°C, at which point stress levels increase slightly while strain values continue to decrease. As the temperature increases during ramp up to 150°C, stress levels increase until approximately room temperature, at which point stress decreases and strain values begin to increase from temperature-dependent creep. At room temperature, the homologous temperature of solder is more than 0.5 and hence stress relaxation begins to occur with the rise in temperature.

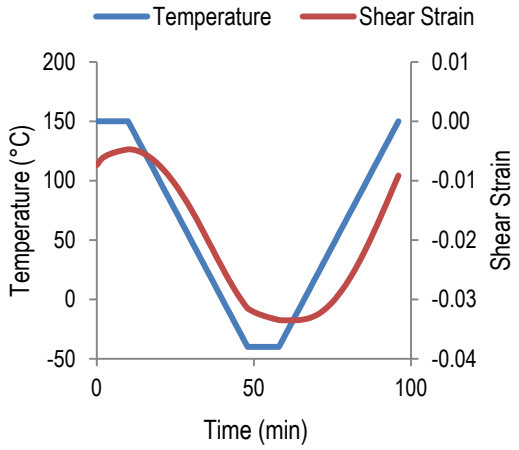

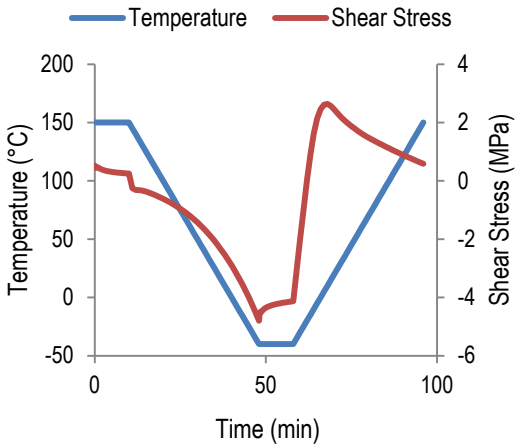

Figure 13: Temperature and shear strain versus time (top) and temperature and shear stress versus time (bottom)

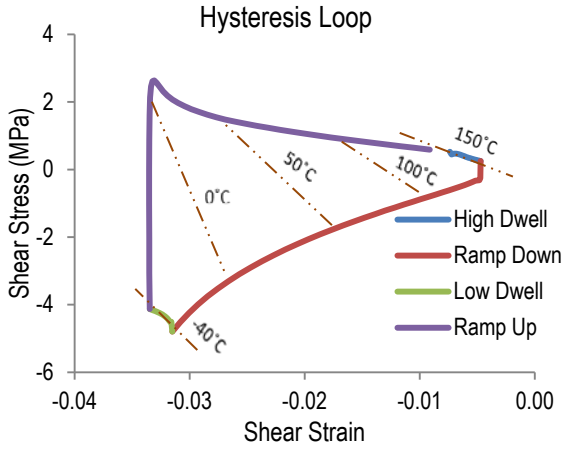

Figure 14: Hysteresis loop from a solder interface's 2-mm fillet maximum equivalent strain node

Figure 15 shows a comparison of stress-strain values between solder interfaces with 1.5-mm and 2-mm fillet corners. Separate simulations were run to obtain the results. The figure shows that under the same temperature loading conditions, an equivalent amount of stress was induced but the maximum shear strain values were reduced in the 2-mm fillet geometry.

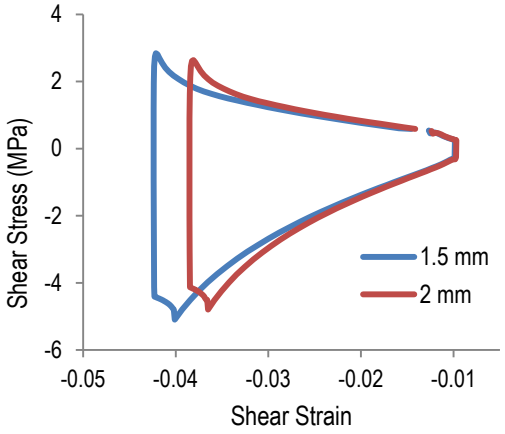

This report is available at no cost from the National Renewable Energy Laboratory (NREL) at www.nrel.gov/publications.

Figure 15: Stress-strain comparison

Energy stored in the solder interface region from deformation during the temperature loading conditions is referred to as the strain energy. The strain energy density is the strain energy per unit volume and is determined by calculating the area within the stress-strain hysteresis loop for a given temperature cycle. The strain energy density values calculated over the entire fillet regions for 1.5-mm and 2-mm fillet corners were 9.04 MPa and 8.91 MPa, respectively.

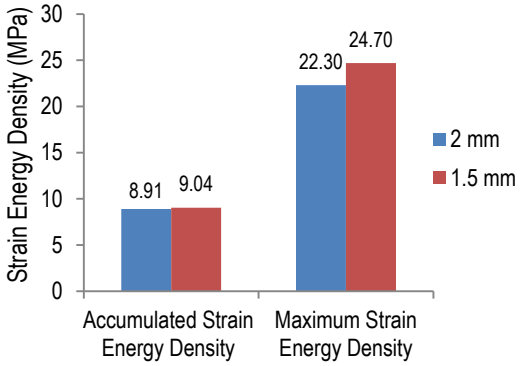

Figure 16: Strain energy density values

These strain energy density values will be correlated with an experimentally determined number of thermal cycles to failure for the $Sn_{63}Pb_{37}$ solder BIM.

Conclusions and Future Directions

A consistent framework has been implemented to establish the thermal performance and reliability of large-area bonded interfaces based on novel/emerging materials such as thermoplastics with embedded carbon fibers and sintered silver materials as compared to $Sn_{63}Pb_{37}$ solder. These large-area attachments are currently being considered in state-of-the-art power electronics packages for electric-drive vehicle applications. Results for bond quality after thermal cycling suggest that thermoplastics with embedded fibers could be a promising alternative to solders. Future work with sintered silver material will focus on minimizing the occurrence of cohesive fracturing by optimizing processing conditions.

Modeling of strain energy density for the $Sn_{63}Pb_{37}$ solder BIM bonded between the metalized substrate and Cu base plate was performed using the Anand model parameters for the solder BIM from the literature. The results will be leveraged in the efforts to generate experimental cycles-to-failure versus strain energy density models for BIMs of interest.

FY 2013 Publications/Presentations

1. DeVoto, D., Paret, P., Narumanchi, S., and Mihalic, M., "Reliability of Bonded Interfaces for Automotive Power Electronics," InterPACK2013-73143, *Proceedings of the 2013 InterPACK Conference,* July 2013, Burlingame, CA (Outstanding Paper Award – Second Place, Mechanics).
2. DeVoto, D., Paret, P., and Mihalic, M., "Reliability of Bonded Interfaces," *2013 DOE Vehicle Technologies Office (VTO) Annual Merit Review,* Crystal City, VA, May 2013.
3. DeVoto, D., Paret, P., and Mihalic, M., "Reliability of Bonded Interfaces," *Presentation to the DOE Vehicle Technologies Office Electrical and Electronics Team,* Southfield, MI, April 2013.
4. DeVoto, D., Paret, P., and Mihalic, M., "Reliability of Bonded Interfaces," *Advanced Power Electronics and Electric Motors FY13 Kickoff Meeting, DOE VTO,* Oak Ridge, TN, November 2012.

Acknowledgments

The author would like to acknowledge the support provided by Susan Rogers and Steven Boyd, Technology Development Managers for Advanced Power Electronics and Electric Motors, Vehicle Technologies Office, U.S. Department of Energy Office of Energy Efficiency and Renewable Energy. The contributions of Mark Mihalic and Paul Paret (NREL) to the project are acknowledged. The author also thanks Jay Browne (Btechcorp) for providing the thermoplastic material and Christian Goebl (Semikron) for provided the bonded samples based on sintered silver material.

References

1. Official Journal of the European Union, 2003, "Directive 2002/95/EC of the European Parliament and of the Council of 27 January 2003 on the Restriction of the Use of Certain Hazardous Substances in Electrical and Electronic Equipment." February 13, 2003.
2. Dudek, R., Faust, W., Ratchev, R., Roellig, M., Albrecht, H., Michel, B., 2008, "Thermal Test- and Field Cycling Induced Degradation and its FE-based Prediction for Different SAC Solders," *Proceedings of the ITHERM Conference*, Orlando, FL, May 28–31, 2008, pp. 668–675.
3. Wang, Q., Johnson, W., Ma, H., Gale, W. F., Lindahl, D., 2005, "Properties of Lead Free Solder Alloys as a Function of Composition Variation," *Electronic Circuits World Convention (ECWC 10),* Anaheim, CA, February 22–24, 2005.
4. Schulze, E., Mertens, C., Lindemann, A., 2009, "Low Temperature Joining Technique – a Solution for Automotive Power Electronics," *Power Conversion, Intelligent Motion (PCIM),* Nuremberg, Germany, May 12–14, 2009.
5. Schulze, E., Mertens, C., Lindemann, A., 2010, "Pure Low Temperature Joining Technique Power Module for Automotive Production Needs," *6th International Conference on Integrated Power Electronics Systems (CIPS),* Nuremberg, Germany, March 16–18, 2010.
6. Narumanchi, S., 2008, 2009, *Thermal Interface Materials for Power Electronics Applications*, NREL Technical

This report is available at no cost from the National Renewable Energy Laboratory (NREL) at www.nrel.gov/publications.

Report MP43970, September 2008; NREL Technical Report, September 2009.

7. Narumanchi, S., Mihalic, M., Kelly, K., Eesley, G., 2008, "Thermal Interface Materials for Power Electronics Applications," *Proceedings of the ITHERM Conference*, Orlando, FL, May 28–31, 2008, pp. 395–404.
8. American Society for Testing and Materials, 2005, ASTM Standard D5470-01.
9. Chuang, R. W., Lee, C. C., 2002, "Silver-Indium Joints Produced at Low Temperature for High Temperature Devices," *IEEE Transactions on Components and Packaging Technologies*, Vol. 25, No. 3, pp. 453–458.
10. McCluskey, P., Quintero, P. O., 2007, "High Temperature Lead-Free Attach Reliability," *Proceedings of InterPACK, IPACK2007-33457*, Vancouver, British Columbia, Canada, July 8–12, 2007.
11. Wu, R., McCluskey, F. P., 2007, "Reliability of Indium Solder for Cold Temperature Packaging," *Proceedings of InterPACK, IPACK2007-31456,* Vancouver, British Columbia, Canada, July 8–12, 2007.
12. Lu, G-Q., Zhao, M., Lei, G., Calata, J. N., Chen, X., Luo, S., 2009, "Emerging Lead-Free, High-Temperature Die-Attach Technology Enabled by Low-Temperature Sintering of Nanoscale Silver Pastes," *International Conference on Electronic Packaging Technology & High Density Packaging (ICEPT-HDP)*, Beijing, China, August 10–13, 2009, pp. 461–466.
13. Lei, T. G., Calata, J. N., Lu, G-Q., Chen, X., Luo, S., 2010, "Low-Temperature Sintering of Nanoscale Silver Paste for Attaching Large-Area (>100 mm^2) Chips," *IEEE Transactions on Components and Packaging Technology*, Vol. 33, No. 1, pp. 98–104.
14. Enerpac, 2011, "Arbor, C-Clamp and Bench Frame Presses," http://www.enerpac.com/en-US/products/presses/arbor-c-clamp-and-bench-frame-presses, Accessed May 2011.
15. Associated Research, Inc., 2011, "Exploring the Necessity of the Hot Hipot Test," http://www.asresearch.com/events-training/pdfs/HotHipot.pdf, Accessed May 2011.
16. Zahn, B. A., 2002, "Finite Element Based Solder Joint Fatigue Life Predictions for a Same Die Stacked Chip Scale Ball Grid Array Package," ChipPAC Inc.
17. Lau, L., Pao, Y., 1997, *Solder Joint Reliability of BGA, CSP, Flip Chip, and Fine Pitch SMT Assemblies*. The McGraw Hill Company, pp. 115–120.
18. Darveaux, R., 2002, "Effect of Simulation Methodology on Solder Joint Crack Growth Correlation," *Electronic Components & Technology Conference (ECTC)*, San Diego, CA, May 28–31, 2002, pp. 1048–1058.
19. Wang, G. Z., 2001, "Applying Anand Model to Represent the Viscoplastic Deformation Behavior of Solder Alloys," *Journal of Electronic Packaging*, Vol. 123, pp. 247–253.
20. Yeo, A, 2006, "Flip Chip Solder Joint Reliability Analysis Using Viscoplastic and Elastic-Plastic-Creep Constitutive Models," *IEEE Transactions on Components and Packaging Technologies*, Vol. 29, No. 2, pp. 355–363.
21. Anand, L., 1985, "Constitutive Equations for Hot Working of Metals," *International Journal of Plasticity*, Vol. 1, No. 2, pp. 213–231.
22. Brown, S. B., Kim, K. H., and Anand, L., 1989, "An Internal Variable Constitutive Model for Hot Working of Metals," *International Journal of Plasticity*, Vol. 5, No. 2, pp. 95–130.
23. JEDEC Solid State Technology Association, 2009, "JESD22-A104D Temperature Cycling."
24. Vandevelde, B., Gonzalez, M., Limaye, P., Ratchev, P., Beyne, E., 2007, "Thermal Cycling Reliability of SnAgCu and SnPb Solder Joints: A Comparison for Several IC-Packages," *Microelectronics Reliability*, Vol. 47, pp. 259–265.
25. Aoki, Y., Tsujie, I., Nagai, T., 2007, "The Effect of Ramp Rate on Temperature Cycle Fatigue in Solder Joints," *Espec Technology Report,* pp. 4–13.
26. Lu, G-Q., Calata, J. N., Lei, G., Chen, X., 2007, "Low-Temperature and Pressureless Sintering Technology for High-Performance and High-Temperature Interconnection of Semiconductor Devices," *International Conference on Thermal, Mechanical and Multi-Physics Simulation Experiments in Microelectronics and Micro-Systems (EuroSime),* London, Great Britain, April 16–18, 2007, pp. 1–5.

This report is available at no cost from the National Renewable Energy Laboratory (NREL) at www.nrel.gov/publications.

Reliability of Electrical Interconnects

Principal Investigator: Douglas DeVoto
National Renewable Energy Laboratory (NREL)
Transportation and Hydrogen Systems Center
15013 Denver West Parkway
Golden, CO 80401
Phone: 303-275-4256
E-mail: Douglas.Devoto@nrel.gov

DOE Technology Development Manager: Susan A. Rogers
Phone: 202-586-8997
E-mail: Susan.Rogers@ee.doe.gov

NREL Task Leader: Sreekant Narumanchi
Phone: 303-275-4062

Start Date: FY11
Projected End Date: FY14

Objectives

- Investigate and improve the reliability of the ribbon bonds using Al and Cu/Al-clad ribbon materials.
- Develop predictive lifetime models for ribbon bonds that can be used to design components and packages.

Technical Barriers

In automotive power electronics modules, standard packaging technologies have limited the advancement of insulated gate bipolar transistor (IGBT)-based power modules toward designs that promise higher performance and reliability. Increased power densities and larger temperature swings reduce lifetimes for traditional wire bond interconnects. Wire bonds can be replaced with a transition to ribbon bonding technology. The ribbon bond process promises a reduction in bonding time, lower loop heights (and corresponding less heel fatigue), and higher current densities than wire bonds. However, as a newer technology, ribbon bond failure mechanisms are not well understood and thus do not have an accurate lifetime estimate.

Technical Targets

Improved package reliability is an enabler to achieve the U.S. Department of Energy (DOE) Advanced Power Electronics and Electric Motors (APEEM) power electronics targets for improved efficiency, performance, and lifetime.

Accomplishments

- Evaluated the initial strength of bonded wire and ribbon interconnects of various configurations.
- Completed temperature cycling and corrosion testing on wire and ribbon interconnects.
- Performed strength evaluation on wire and ribbon interconnects after accelerated testing.

Introduction

The drive toward reduced cost, weight, and volume of components in electric drive vehicles has led to increased performance demands on power electronics modules. The trend toward higher power densities, current levels, and operating temperatures has shown that traditional packaging designs cannot meet the industry's reliability needs. Figure 1 shows an example of a power electronics package with electrical interconnects (wire or ribbon bonds), die (IGBT or diode), metalized substrate, and base plate components.

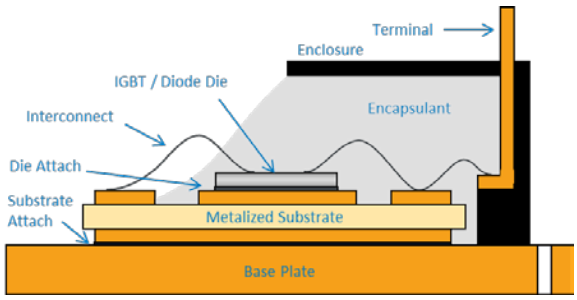

Figure 1: Traditional power electronics package

Wire bonding technology is used to electrically connect dies to each other, to the top metallization layer within the substrate, or to lead frames for connections outside of the power electronics package. Au, Cu, or Al has traditionally been used as the wire material, with each having tradeoffs in cost, current carrying capability, and mechanical strength [1]. For most common applications, Al has replaced Au and Cu because of its lower cost, but Cu is still selected for power module designs with high current requirements. In addition to material selection, the maximum current a wire can carry is dependent on its length and diameter; wire sizes are typically between 300 and 500 µm in diameter. If the maximum current level is exceeded, ohmic self-heating will cause the wire to fuse [2]. Heating from within the wire as well as from the silicon dies creates large temperature fluctuations during operation. These temperature variations and coefficient of thermal expansion (CTE) mismatches between the wire material and silicon dies or metalized substrates cause failures in the heel of the wire through flexure fatigue as well as bond pad lift-off. Analytical models have been developed for both failure modes to estimate the mean number of cycles to failure. Failure modes for wire and ribbon interconnects are shown in Figure 2.

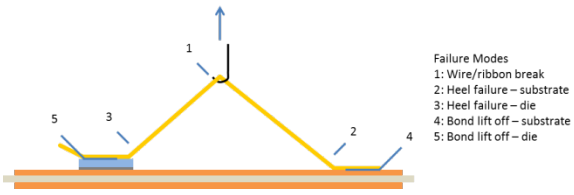

Figure 2: Wire and ribbon interconnect failure modes

This report is available at no cost from the National Renewable Energy Laboratory (NREL) at www.nrel.gov/publications.

For high-current power modules, mechanical limitations to bonding a wire with a diameter larger than 500 µm has required multiple wires to be bonded in parallel. Adding more parallel wires is limited by a substrate's bond pad area and increases the time and cost of bonding. These limitations have generated interest in replacing wire bonds with ribbon bonding technology. Three Al wire bonds with diameters of 400 µm can be replaced on an equivalent electrical current basis by one ribbon bond with a cross section of 2,000 µm × 200 µm [3]. The single ribbon requires a bond width of 2 mm; the three wire bonds require a width of 2.5 mm. Bonding times for both technologies remain the same (300 ms per bond); therefore, the ribbon bonding time for a package can be reduced. For the same span distance, a ribbon bond allows for a lower loop height than a wire bond. This helps to reduce heel stress and ultimately flexure fatigue. Minimizing heel stress is necessary as desired IGBT operating junction temperatures continue to rise to 175°C or higher [4]. However, because of the ribbon's larger geometry, higher bonding energies and forces are required and bond pad contact areas become larger. Damage initiated during the bonding process could be more likely under ribbon bonding, and CTE mismatches between the interconnect material and silicon devices or metalized substrate could cause failure under thermal cycling conditions.

The performance and reliability of conventional wire bonding are well understood; however, lifetime uncertainties of newer interconnect technologies remain barriers for those novel processes to be utilized by industry. The work at NREL focuses on providing a comprehensive reliability assessment of alternative interconnect technologies to wire bonds, beginning with ribbon bonding. Ribbon bonds are attached to a substrate under a variety of materials and geometries, and then subjected to accelerated test conditions that highlight the same failure mechanisms found under normal operating conditions. Ideas unique to ribbon bonding will be evaluated, first with the selection of a Cu/Al-clad ribbon that allows the Al to be easily bonded to silicon die surfaces while providing the improved electrical performance of Cu [5]. The ribbon's rectangular cross-section geometry makes twisting to create forced angles more difficult than with wire bonding; therefore, bonds with several forced angles will be attached to substrate samples [6]. The proposal to attach multiple ribbons over the same bond pad location will be explored as a stacked bonding technique [7]. In conjunction with accelerated testing, physics-of-failure models based on wire bond geometry will be validated for ribbon bonds.

Approach

Materials and Sample Synthesis

NREL has chosen several ribbon materials under various geometries for accelerated testing. The variations are as follows:

- Material – Al ribbon and a 2:1 ratio Cu/Al-clad ribbon.
- Ribbon cross-section – Two cross-sections suitable for current levels within a power module were chosen to be 2,000 µm × 200 µm and 1,000 µm × 100 µm.
- Ribbon span – 10-mm and 20-mm spans were selected. Corresponding loop heights were set at a ratio of 1:2.2 to ribbon span.
- Number of stitches – Single and double stitches were bonded for 20-mm ribbon spans.
- Ribbon stacking – Stacking one ribbon pad above a second pad can minimize the bonding area on the top of a die but may create a weaker bond.
- Forced angle – Forcing a ribbon at various angles from its bond pad orientation would allow for offset pad locations, but may also create a weaker bond.
- Bond pad interfaces – One end of each ribbon will be bonded to a silicon die and the other end to a substrate's top Cu metalized surface.
- Bonding power – Two bonding powers were selected to evaluate the relationship between bond pad strength and long-term reliability.

The ribbon material and geometry variations cover a design space likely used within a power electronics unit if wire bonds were to be replaced with ribbon bonds. The ribbon bond variations are shown in Figure 3.

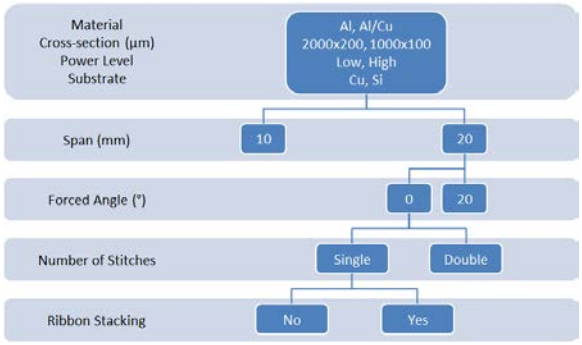

Figure 3: Ribbon bond variations

Three instances of each ribbon configuration were arranged on a 140-mm × 190-mm test substrate. The substrate was obtained from Curamik and is constructed of a 0.635-mm-thick alumina layer sandwiched between two 0.203-mm-thick Cu metallization layers. The design of the etch mask for the top Cu layer configures four ribbon bonds electrically in series with multiple parallel paths. This layout was chosen for power cycling samples, but remains the same for all samples. Before the ribbon material was attached to the test substrate, Vishay 5-mm × 5-mm Schottky diodes were soldered in place. The selected diodes have a breakdown voltage of 100 V and can reach a maximum junction temperature of 175°C. The diode backside has a Cr/Ni/Ag coating for good solderability; the top side includes a 3-µm layer of Al (1% Si) to be compatible with the ultrasonic bonding process. Each test substrate was imaged by acoustic microscopy to ensure that the solder attachment for each diode contained minimal voiding. The first end of each ribbon interconnect was bonded to the top Cu metallization layer of the test substrate; the second was bonded to the top surface of the diode. Both Al- and Cu/Al-clad ribbon materials were obtained from Materion Technical Materials and were attached using an Orthodyne 3600 wedge bonder at Kulicke & Soffa. Dow Corning 3-4150

This report is available at no cost from the National Renewable Energy Laboratory (NREL) at www.nrel.gov/publications.

gel kits were used to protect the interconnects in silicone encapsulant. An example of a test substrate with a completed design layout is shown in Figure 4.

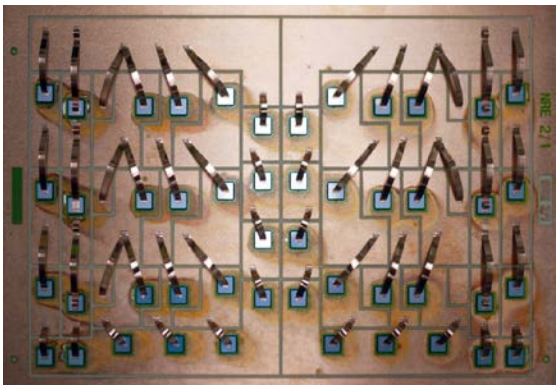

Figure 4: Test substrate showing ribbon layout (Photo credit: Doug DeVoto, NREL)

The four geometry variations (span, forced angle, number of stitches, and ribbon stacking) require eight ribbon interconnects; repeating each variation three times brings the total number of interconnects to 24, or one half of a test substrate. Including the additional ribbon selection variations (material, cross-section, and power level) requires a total of eight test substrate halves, or four test substrates. An additional half test substrate is added to include 500-µm-diameter Al wire bonds as a reference to the ribbon bonds. Thus, four and a half test substrates are required for each accelerated test condition.

Ribbon Bonding Mechanical Characterization

An XYZTEC Condor 100-3 mechanical bond tester was used to measure the pull strength of the ribbon and wire bonds. As this was a destructive evaluation, one set of test sample substrates without any prior accelerated testing was selected to measure initial bond strength through pull tests. Silicone encapsulant was removed prior to pull testing with Digesil NCX de-polymerization compound. For the pull test, a hook was first positioned under the ribbon bond. At the initiation of the test, a constant velocity of 250 µm/s was applied to the hook and maintained for a travel distance of approximately 4 mm. Sufficient force was used to maintain this velocity against the tensile strength of the ribbon material and strength of the bond pads. A test was completed when one of the five failure modes previously listed occurred, and the maximum force required for failure was recorded. This force was compared to minimum acceptable bond strengths as outlined in Method 2011.8 of the Department of Defense Test Method Standard 883H. The minimum acceptable pull force is a function of the interconnect's cross-section, as shown in Figure 5.

In addition to recording the maximum tensile force, the failure mode was documented. Images showing the most common modes are shown in Figure 6.

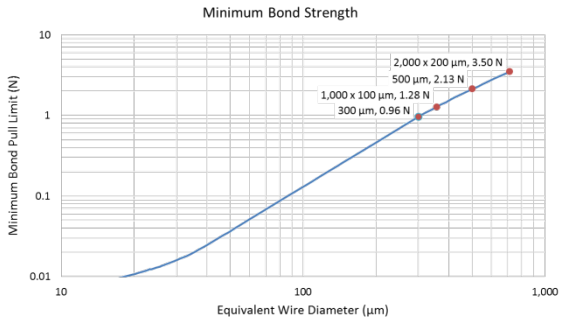

Figure 5: Minimum wire and ribbon bond pull strength limits

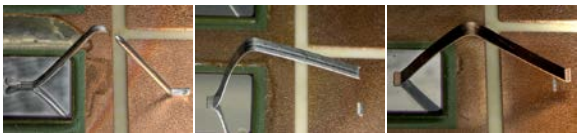

Figure 6: Failure modes from the left: wire break (left), heel failure from substrate (center), and bond lift-off from substrate (right) (Photo credit: Doug DeVoto, NREL)

Accelerated Testing

Subjecting a component to accelerated test conditions identifies its failure mechanisms in a shorter time relative to normal operating stress conditions. Various accelerated tests were selected to evaluate likely failure mechanisms within ribbon interconnects and are shown in Table 1. These test procedures are based on standards for the microelectronics industry [8].

Table 1: Accelerated Testing Procedures

Accelerated Test	Testing Condition	Duration
Temperature Elevation	150°C	1,000 hours
	200°C	96 hours
	250°C	96 hours
Temperature Cycling	–40°C to 150°C, less than 20 s transition time	3,000 cycles
	–40°C to 200°C, less than 20 s transition time	3,000 cycles
Corrosion Testing	85°C, 85% relative humidity, cycled DC bias	1,000 hours
	121°C, 100% relative humidity	96 hour s
Power Cycling	–40°C to 125°C, 10 minute dwell, 10°C/min ramp rates, cycled DC bias	1,500 temperature cycles
Vibration Testing	Highly accelerated life test	Until interconnect fails

Accelerated test methods—humidity, thermal, power, vibration, or a combination of the four—are designed to highlight a particular interconnect's failure mode.

- Samples subjected to high-temperature storage testing will highlight thermally activated failure mechanisms. Ribbon bonds will be stored under three separate test

This report is available at no cost from the National Renewable Energy Laboratory (NREL) at www.nrel.gov/publications.

conditions, at 175°C for 1,000 hours and at 200°C and 250°C for 96 hours.

- Alternating temperature extremes will test the ability of interconnects to withstand thermally induced mechanical stresses. Samples will be cycled either from –40°C to 150°C or –40°C to 200°C for 3,000 cycles. Transition times between temperature extremes will be completed in less than 20 seconds and no dwell/soak times will be held.
- Two humidity-based tests will evaluate the corrosion resistance of the ribbons and their bond pads. Under a humidity bias test, ribbon interconnects will be placed in an 85°C, 85% relative humidity environment for 1,000 hours. A DC bias will be applied during the test. Under a second humidity test, samples will be subjected to a 121°C, 100% relative humidity environment for 96 hours with no electrical bias. This is considered a destructive test.
- Under combined power and thermal cycling, interconnects will be subjected to a periodically applied operating bias while they experience high and low temperature extremes. Samples will be cycled from –40°C to 125°C for 1,500 cycles, with ramp rates of 5°C/minute and dwell/soak times of 10 minutes.
- Random six-degree-of-freedom vibration and rapid thermal cycling will stress the ribbon bonds beyond their design specifications to quickly highlight predominant failure mechanisms.

Two accelerated tests were completed for 500-µm-diameter Al wire and 1,000 µm × 100 µm ribbon. Their testing conditions and durations are outlined in Table 2.

Table 2: Completed Accelerated Tests

Accelerated Test	Testing Condition	Duration
Temperature Elevation	200°C	144 hours
Corrosion	121°C, 100% relative humidity	144 hours

Results

Initial Results

Initial results from pull test data are shown in the following figures for Al wire, Cu/Al ribbon, and Al ribbon. The Al wire used has a cross-section of 500 µm; the ribbon interconnects have 1,000 µm × 100 µm cross-sections. The bonding power for ribbon interconnects is specified as either low or high. Three test bonds were completed for each bonding method, which includes defined interconnect material, geometry, and bonding parameters. The averages of these pull strength tests between Al wire, Cu/Al ribbon, and Al ribbon are shown in Figure 7; error bars indicate the standard deviations between tests.

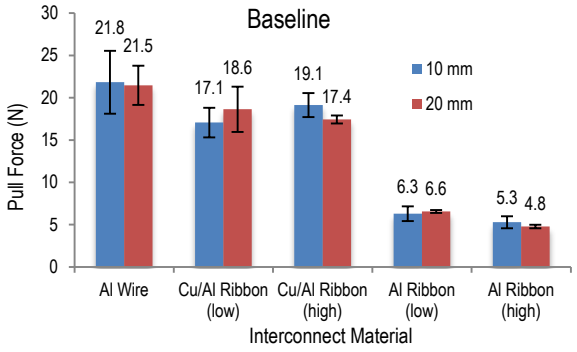

Figure 7: Pull force versus interconnect material

Al wire interconnects exhibited the greatest strength from the pull tests, closely followed by Cu/Al ribbons. The strength of Al ribbon bonds was noticeably lower, but still strong enough to be considered successful. The key aspect to monitor is if the bond strength for each respective interconnect material significantly decreases after accelerated tests. The failure modes associated with the above pull test measurements are shown in Figure 8. The three interconnects tested for each bonding method typically failed by a similar method. Although bond strength remained approximately the same between low and high power bonds for Cu/Al ribbons, the failure method shifted from bond pad lift-offs to heel failures. This indicates that the lower power setting for Cu/Al ribbons may not be sufficient to adequately bond the Al side of the ribbon to the metalized substrate, but accelerated testing will highlight if the lower power setting ultimately ends in a bond with longer lifetime.

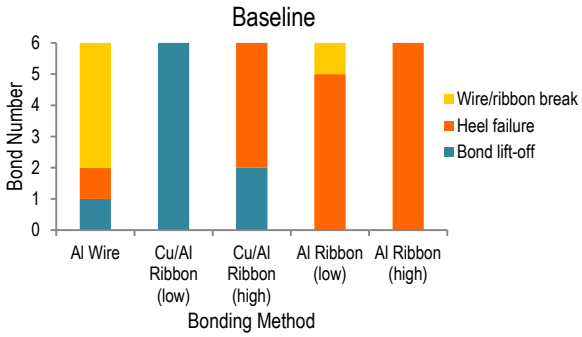

Figure 8: Failure modes for interconnect materials

A similar analysis of bond strength for Cu/Al ribbon interconnects at various forced angles was also completed. Results indicated that bond strength was reduced as a consequence of imparting a forced angle onto the ribbon bonds. The averages of these pull strength tests are shown in Figure 9; error bars indicate the standard deviations between tests.

This report is available at no cost from the National Renewable Energy Laboratory (NREL) at www.nrel.gov/publications.

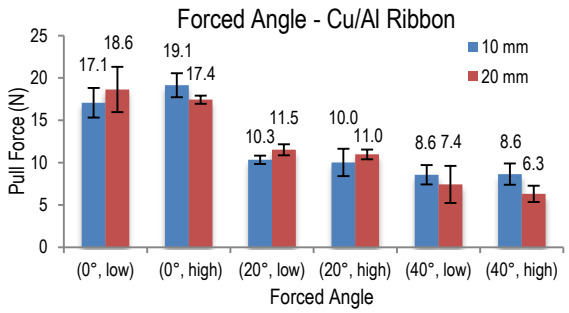

Figure 9: Pull force versus forced angle of Cu/Al ribbon

A forced angle analysis was also completed for Al ribbon bonds, as shown in Figure 10. The bond strength is slightly reduced when incorporating forced angle geometries.

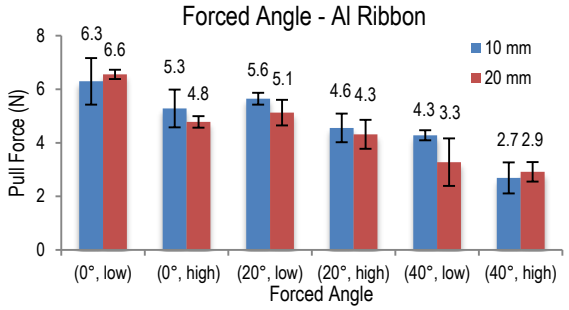

Figure 10: Pull force versus forced angle of Al ribbon

As previously apparent with Cu/Al ribbon bonds with no forced angle, increasing bonding forces shifted the failure methods from bond pad lift-offs to heel failures, as shown in Figure 11.

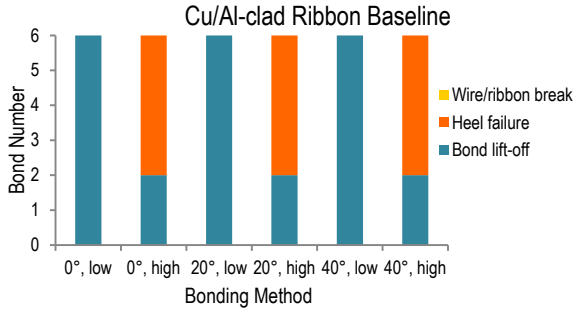

Figure 11: Failure modes for Cu/Al ribbon at forced angles

The failure modes for Al ribbon under forced angles were consistently heel failures on either the die or substrate side of the ribbon, shown in Figure 12.

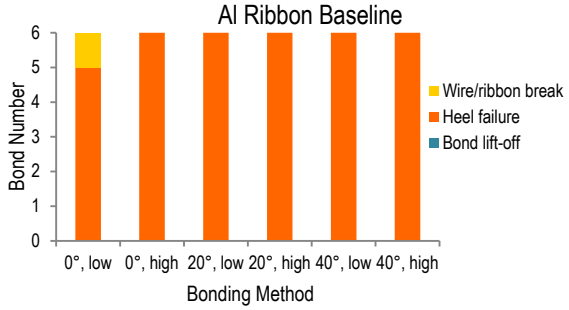

Figure 12: Failure modes for Al ribbon at forced angles

Mechanical tests are conducted on samples after they complete their designated accelerated testing procedure. In addition to mechanical evaluation, cross-sections of ribbon bond pads will provide a qualitative way to determine if the grain structure has changed after accelerated testing. Bonding of dissimilar metals between the ribbon and pad causes intermetallic formation and Kirkendall voiding under high-temperature storage tests. Visual analysis will also monitor signs of corrosion development.

Accelerated Test Results

Pull testing of the wire and ribbon interconnects after accelerated testing indicated various reductions in bond strength. The effects of temperature elevation and humidity testing reduced the bond strength of Al wire and Cu/Al ribbon interconnects, but strength levels were still above minimum acceptable values. Humidity testing of Al ribbon caused pull strength failures below acceptable strength levels outlined by MIL-STD-883H Method 2011.8. Results for 10-mm span and 20-mm span interconnects are shown in Figures 13 and 14.

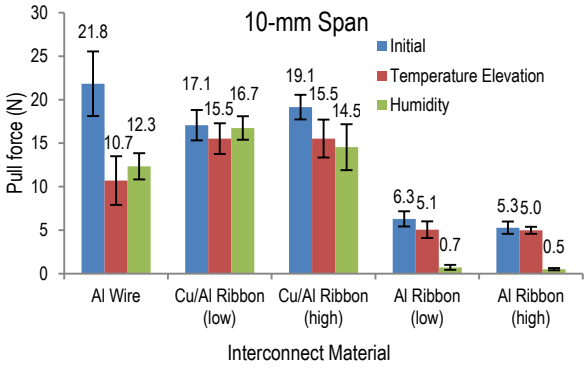

Figure 13: Pull force versus 10-mm span interconnect material after accelerated tests

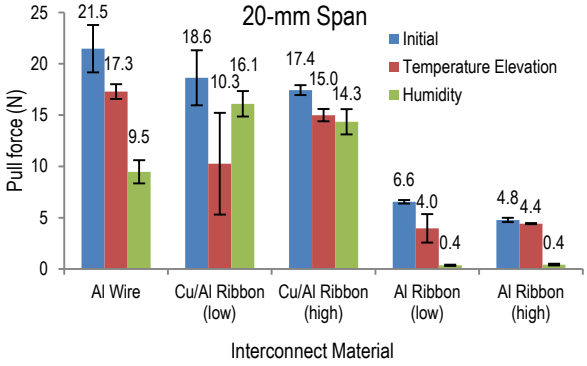

Figure 14: Pull force versus 20-mm span interconnect material after accelerated tests

Failure modes were recorded for each interconnect after accelerated testing. Temperature elevation testing resulted in Al wire breaks from the initial pull testing evaluation to shift to bond pad lift-off failures. Al and Cu/Al-clad ribbon failure modes remained the same. Temperature elevation testing failure mode results are shown in Figure 15.

This report is available at no cost from the National Renewable Energy Laboratory (NREL) at www.nrel.gov/publications.

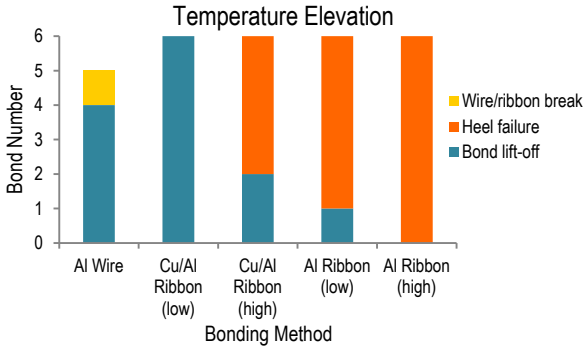

Figure 15: Failure modes for interconnect materials after accelerated tests

Corrosion testing resulted in Al wire breaks from the initial pull testing evaluation to shift to bond pad lift-off failures. Al ribbon heel failures from initial pull testing shifted to ribbon breaks, indicating that the low pull force results were caused by a decrease in the strength of the interconnect material itself. Cu/Al-clad ribbon failure modes remained the same. Corrosion testing failure mode results are shown in Figure 16.

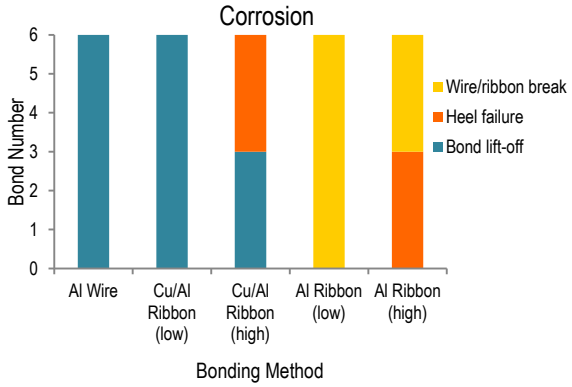

Figure 16: Failure modes for interconnect materials after accelerated tests

Physics of Failure Models

Under temperature cyclic loads, the CTE mismatch between the ribbon material and the silicon die or metalized substrate results in stress/strain reversals in the heel of the ribbon interconnect, gradually leading to its failure. Physics of failure models identify the root cause of this failure and then provide lifetime estimation based on material properties, geometry, and environmental conditions [9]. Using the theory of curved beams, the strain prediction on the upper side of the ribbon bond can be approximated using equation 1:

$$\varepsilon = \frac{r(\rho_f - \rho_i)}{\rho_i \rho_f} = r(k_i - k_f) \quad (1)$$

where

ε is strain induced

r is half the thickness of the ribbon

ρ_f is the radius of curvature of the ribbon heel after heating

ρ_i is the radius of curvature of the ribbon heel before heating

k_f is the curvature at the heel of the ribbon after heating

k_i is the curvature at the heel of the ribbon before heating

This equation shows that the strain induced in the lower side ($[\rho_i/\rho_f]$+2r) will be lower compared to the strain in the upper side of the ribbon. Once the strain is calculated, the number of cycles to failure, N_f, can be determined using the Coffin-Manson equation:

$$N_f = C_r \varepsilon^{-m_r} \quad (2)$$

where C_r and m_r are fatigue properties found through material tensile tests.

As the loop geometry plays a significant role in the prediction of strain values, the ribbon should be in a state of minimum potential energy. An energy-based cubic spline model is used to determine the geometry of the loop that achieves a minimum potential energy [9]. For a given span, the loop height is varied to find the least energy state, by equation 3:

$$d = \frac{Dh}{H}\left[1 - \sqrt{1 - \frac{H}{h}}\right] \quad (3)$$

where

d is half the span

h is loop height

D is the total span of the ribbon

H is the height offset between bond pads

This calculation was used to determine the least energy state for a ribbon interconnect to have a ratio of 1:2.2 loop height-to-span length.

A finite element analysis (FEA) model was developed to find the stress and strain values induced in an Al ribbon bond with a 10-mm span. The model geometry of a sample ribbon interconnect was created in SolidWorks and imported into ANSYS Workbench. A cross-section image of the sample ribbon was experimentally measured using a microscope to create a spline fit profile that could be imported into the FEA model. The plasticity model was specified as a multilinear kinematic hardening model to properly define the plastic behavior of the Al material, with stress-strain values at room temperature obtained from corresponding curves from literature [10]. A test case was run with a temperature cycle profile from 20°C to 160°C at a ramp rate of 5°C/min. A maximum deflection of 33.8 µm was observed at the center of the profile at the highest region. Maximum von Mises stress values of 193.9 MPa and 183.1 MPa were found to be at the heel for the first and second bond pads, respectively. The maximum deflection result from the model will be compared against experimentally obtained deflection results to validate the FEA model. The SolidWorks geometry and maximum von Mises stress are shown in Figure 17.

This report is available at no cost from the National Renewable Energy Laboratory (NREL) at www.nrel.gov/publications.

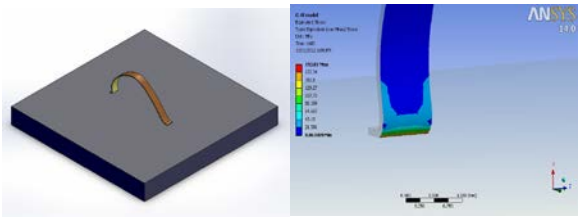

Figure 17: FEA model of 1,000 µm × 100 µm Al ribbon with 10-mm span (left) and maximum stress shown at heel location near second bond pad (right)

Future modeling results will be improved by including temperature-dependent material properties for Cu and Al, and will be expanded to include Cu/Al-clad ribbon geometries. Deflection, von Mises stress, and strain results will be compared to the failure modes observed in the experimental accelerated tests. Analytical and FEA results will be incorporated into the Coffin-Manson relation to predict the number of cycles to failure, and validated with experimental test results for cycles to failure.

Conclusions and Future Directions

The work establishes the foundation for a comprehensive evaluation of the reliability of ribbon bond interconnects. To date, the impact of temperature elevation and humidity on the interconnects have been investigated. Some key findings were that temperature elevation and humidity testing reduced the bond strength of Al wire, Al ribbon, and Cu/Al ribbon, but the strength levels were still above minimum acceptable levels. Humidity testing of the Al ribbon caused pull strength failures below acceptable strength levels. When the interconnects were pull tested after accelerated testing, some interesting changes in the pattern of the failure modes were observed with respect to the modes of failure observed in pull testing prior to accelerated testing. A variety of materials and geometries will continue to be tested under various accelerated testing conditions to highlight failure mechanisms. Combining experimental results with time-to-failure models will enable reliability predictions for ribbon interconnects.

FY 2013 Publications/Presentations

1. DeVoto, D., Paret, P., and Mihalic, M., "Reliability of Electrical Interconnects – June 2013 Milestone Report," *FY2013 DOE milestone report,* June 2013.
2. DeVoto, D., Paret, P., and Mihalic, M., "Reliability of Electrical Interconnects," *Presentation to the DOE Vehicle Technologies Office (VTO) Electrical and Electronics Technical Team,* Southfield, MI, May 2013.
3. DeVoto, D., Paret, P., and Mihalic, M., "Reliability of Electrical Interconnects," *2013 DOE VTO Annual Merit Review,* Crystal City, VA, May 2013.
4. DeVoto, D., Paret, P., and Mihalic, M., "Reliability of Interconnects," *Advanced Power Electronics and Electric Motors FY13 Kickoff Meeting, DOE VTO,* Oak Ridge, TN, November 2012.

Acknowledgments

The author would like to acknowledge the support provided by Susan Rogers and Steven Boyd, Technology Development Managers for Advanced Power Electronics and Electric Motors, Vehicle Technologies Office, U.S. Department of Energy Office of Energy Efficiency and Renewable Energy. The contributions of Mark Mihalic and Paul Paret (NREL) to the project are acknowledged. The author would also like to acknowledge Christoph Luechinger (Kulicke & Soffa) for providing substrates with the ribbon bonds.

References

1. Ménager, L., Martin, C., Allard, B., and Bley, V., 2006, "Industrial and lab-scale power module technologies: A review," *IEEE 32nd Annual Conference on Industrial Electronics (IECON)*, Paris, France, November 7–10, pp. 2426–2431.
2. Ciappa, M., 2002, "Selected failure mechanisms of modern power modules," *Microelectronics Reliability*, Vol. 42, pp. 653–667.
3. Farassat, F., and Sedlmair, J., 2007, "More performance at lower cost – heavy aluminum ribbon bonding," F & K Delvotec Bondtechnik GmbH.
4. Guth, K., Siepe, D., Görlich, J., Torwesten, H., Roth, R., Hille, F., and Umbach, F., 2010, "New assembly and interconnects beyond sintering methods," *Power Conversion, Intelligent Motion (PCIM),* Nuremberg, Germany, May 4–6, 2010.
5. Luechinger, C., Loh, T., Oftebro, K., and Wong, G., 2007, "Composite aluminum-copper ribbon bonding – heel reliability," *Proceedings of IMAPS*, San Jose, CA, November 11–15, 2007.
6. Luechinger, C., 2007, "Ribbon bonding – A Scalable interconnect for power QFN packages," *IEEE 9th Electronics Packaging Technology Conference (EPTC),* Singapore, December 10–12, 2007, pp. 47–54.
7. Almagro, E., and Granada Jr., H., 2008, "Stack bonding technique using heavy aluminum ribbon wires," *IEEE 10th Electronics Packaging Technology Conference (EPTC),* Singapore, December 9–12, 2008, pp. 976–981.
8. "Standards & documents search," JEDEC, <http://www.jedec.org/standards-documents>.
9. Meyyappan, K., 2004, *Failure prediction of wire bonds due to flexure*, Ph.D. Thesis, College Park, MD: University of Maryland.
10. Tamarin, Y., 2002, *Atlas of stress-strain curves,* 2nd Edition, Materials Park, OH: ASM International.

This report is available at no cost from the National Renewable Energy Laboratory (NREL) at www.nrel.gov/publications.